

Università di Pisa
Facoltà di Scienze Matematiche Fisiche e Naturali
Corso di Laurea Magistrale in Fisica

Anno Accademico 2010/2011

Master Thesis

**Impact of PAMAM dendrimers on the
photophysics of linked fluorophores: a
spectroscopy and microscopy approach**

Candidate
Diana Di Paolo

Advisor
Dott.
Stefano Luin

Contents

Introduction	1
1 Dendrimers: promising tools for biomedical purposes	7
1.1 The Dendritic Architecture	7
1.2 Dendrimers: chemistry and structure.	8
1.2.1 Synthesis: Divergent and Convergent Methods	9
1.3 Unique Features of Dendrimers.	11
1.3.1 Comparison with Traditional Polymers	12
1.4 Dendrimers for Biological Applications	13
1.4.1 Drug Delivery	14
1.4.2 Gene Delivery	15
1.4.3 Biocompatibility and Toxicity	15
2 Light-Matter Interactions	17
2.1 Primary and Secondary photophysical processes	17
2.2 Radiation Absorption and B Einstein coefficients	19
2.2.1 The Extinction Coefficient	21
2.3 Spontaneous Emission and A Einstein coefficient	21
2.4 Emission spectra and their properties	23
2.4.1 Jablonski Diagrams	23
2.4.2 Internal Conversion and Kasha's Rule	24
2.4.3 InterSystem Crossing and Phosphorescence	25
2.4.4 Quenching of Fluorescence	25
2.4.5 Resonance Energy Transfer (RET)	26
2.4.6 Effects of Chemical Environment on Emission Spectra	28
2.5 Lifetimes and Quantum Yields	28
2.5.1 Brightness	29
2.6 Fluorescence Microscopy	30
2.6.1 Confocal Microscopy	31
2.6.2 The Point Spread Function (PSF)	32
2.6.3 Fluorescent Markers	33
2.6.4 Fluorescence Lifetime Imaging Microscopy	36
2.6.5 Fluorescence Correlation Spectroscopy	40

2.6.6	Single Molecule Detection	44
3	Materials, Methods and Experimental Results	47
3.1	Fluorescein and derivative dyes	47
3.2	Materials	48
3.2.1	Procedure for Fluorophore Labeling of PAMAM Dendrimers	48
3.2.2	General Procedure for PAMAM Dendrimer Acetylation	50
3.3	UV-Vis Spectrofluorimetry: Methods	51
3.3.1	Fluorescein Absorption and Emission Spectra	52
3.3.2	Titration and Volume Corrections	54
3.4	UV-Vis Spectrofluorimetry: Results	54
3.4.1	NHScarboxyfluorescein-Glycine Absorption and Emission Spectra.	54
3.4.2	Samples pH Titrations	56
3.4.3	Absorption and Emission Peak Wavelength Shift	61
3.4.4	Molar Extinction Coefficients	64
3.4.5	Quantum Yields	66
3.5	Fluorescence Lifetime Measurements	67
3.5.1	Instrument Calibration	67
3.5.2	IRF and Results on NHScarboxyfluorescein	68
3.5.3	Results on the Samples	69
3.6	Single Molecule Detection (SMD)	73
3.6.1	Sample Preparation	73
3.6.2	Data Acquisition and Analysis	75
3.6.3	Single-Molecule Statistics	76
3.7	Fluorescence Correlation Spectroscopy (FCS)	78
3.7.1	Correction-Ring: adjusting cover glass correction	79
3.7.2	Calibration with Fluorescein Standard	80
3.7.3	Fit of Autocorrelation Curves	81
3.7.4	MCS Traces	83
4	Impact of PAMAM dendrimers on the photophysics of 5(6)-FAM SE	87
4.1	Spectral Features	87
4.2	Distribution of Quantum Yields	88
4.3	Single-Molecule Experiments	92
	Conclusions and Perspectives	101
	Bibliography	102
	Acknowledgements	107

Introduction

In the scientific world of today it is sometimes argued that the key to future progresses in Science lies in a more and more increasing specialization of individual areas of research, such as Mathematics, Physics, Biology and Chemistry. Although all these subjects may rightly undertake different roads in order to evolve our knowledge of Nature from different point of views, these paths should not be thought of as parallel. In fact, the most exciting and revolutionary discoveries may be waiting for us when they cross. Some of the most productive contributions to the advancing of science come from people who have developed a solid specialized background in either of the traditional disciplines, but have then pursued a horizontal research work, marked by interdisciplinary exchanges and cross-linking of knowledges.

Biophysics is a relatively new approach to the Life Sciences, founded on a strongly multidisciplinary background of Biology, Chemistry and Physics. It focuses on the biochemical processes that characterize the carbon-based life, and aims to explain them as fully as possible trying to frame them in a theoretical model. In order to reach this goal, fluorescence microscopy and spectroscopy, particularly in time-resolved variants, are establishing as primary research tools. Some of the most recent and promising applications of Biophysics are in the biomedical field. One of the scientists' ultimate purpose would be realizing nano-devices capable of diagnosing and healing the single diseased cells, without involving the healthy ones. It is evident how nano-medicine would be much less invasive and much more accurate than its macroscopic counterpart. To achieve this goal, it is desirable to develop and create a multivalent dispositive composed by a scaffold that should be biocompatible and metabolizable by the body once its job is finished, and able to carry cell-penetrating targeting agents (peptides, antibodies, small ligands), sensing and/or imaging moieties (fluorophores or probes of other kind) and actuators (drugs or similar). In this view, many macromolecules have been proposed as building blocks for this nanotool, for example nanoparticles, nanotubes and dendrimers.

Dendrimers are highly branched synthetic polymeric molecules, with all bonds emanating radially from a central core with highly reproducible structure. They have revealed a considerable potential in several biological and biomedical applications; one of the interesting features of these macromolecules is that they have surface groups that can be successfully functionalized in a controlled way, *e.g.* with drugs, fluorophores, or other contrasting or sensing agents, in order to serve as biosensors in the cellular environment or as drug

carriers once they are internalized in living cells or organisms [1, 2].

This emerging scenario motivates the present thesis work. Indeed, while there exist many papers and works regarding (or even exploiting) fluorophore-functionalized dendrimers [3, 4], a careful analysis of the impact of dendrimers on the photophysics of those fluorophores is still missing. In the work described in this thesis, several of the fluorescence techniques most widely used in Biophysics have been employed to study the physical-chemical properties of Polyamidoamine (PAMAM) dendrimers functionalized with fluorescent dyes Carboxyfluorescein N-hydroxy succinimide ester (5(6)-FAM SE or NHS-carboxyfluorescein). In particular, the dendrimers used are of Generation 4 (G4) and have an ethylenediamine core. Beyond the classical spectroscopic techniques aimed at investigating absorption and fluorescence properties of the samples, three specific fluorescence microscopy techniques have been exploited: Fluorescence Lifetime Imaging Microscopy (FLIM), Fluorescence Correlation Spectroscopy (FCS) and Single Molecule Detection (SMD) [5].

The ultimate goal of this project is to study how the optical and mechanical properties of the samples may vary with respect to the dye alone also by tuning relevant parameters, such as the charge on the surface of the dendrimer (*i.e.* by acetylating the usually positively charged amino end groups), the number of fluorophores on the surface, the pH, and other significant quantities that may affect the internalization, diffusion and the general behavior of dendrimers in cells.

In order to reach this goal, molar extinction coefficients of the charged samples and quantum yields of either charged and acetylated samples were determined; these values were compared with the known ones of the dye alone (also confirmed by measurements I performed firsthand). We found that the direct linkage to the dendrimer surface affects the optical properties of the dye by a similar extent for charged and neutral samples: in particular, we observed a strong decrease in its average quantum yield. Absorption and emission spectra at various pH were recorded; differences in the shape and peak wavelength of the spectra with respect to those of the non-conjugated fluorophore were interpreted as caused by interactions between the dye(s) and the dendrimer local environment. Finally, measurements performed by means of fluorescence microscopy (FLIM, FCS) and Single-Molecule techniques allowed us to better elucidate the results obtained with spectroscopy methods, reaching the following conclusions: there are interactions between NHS-carboxyfluorescein fluorophores bound directly to the surface of PAMAM dendrimers with the dendrimers themselves, which affect significantly the photophysical properties of the dyes; there are different configurations which cause different brightnesses for the dyes; these configurations seem to evolve dynamically in the single dendrimer-dye(s) systems, probably according to the ever-changing local conformation of these complexes.

This thesis is organized as follows:

- **Chapter 1** focuses on dendrimers, with particular attention to their chemical structure, the unique features of the dendritic architecture and their biological applications.
- **Chapter 2** starts with a brief overview of the general theory that underlies the interactions between light and matter. In particular, I describe the processes of absorption and emission of radiation, the mechanism of fluorescence and its typical characteristics, such as lifetime, quantum yield and quenching. Then, the main spectroscopic and fluorescence microscopy techniques exploited during the experimental part of this project are illustrated, with particular emphasis on the three mentioned above.
- In **Chapter 3**, after a brief outline of the chemical and optical properties of fluorescein and its derivative dyes, the materials and methods are listed, and the obtained results reported, for each technique employed.
- **Chapter 4** summarizes the main experimental results of this thesis work. In this chapter, a qualitative model of interpretation for the peculiar behavior of the system dendrimer-fluorophores is proposed and the evidences observed in the experiments are enclosed in a global descriptive frame.
The thesis ends with the conclusions and an overlook on future perspectives.

Chapter 1

Dendrimers: promising tools for biomedical purposes

1.1 The Dendritic Architecture

In organic chemistry, a dendritic macromolecule is a molecule whose structure is characterized by a high degree of branching that originating from a single focal point (core). The dendritic architecture is perhaps one of the most pervasive topologies observed on our planet. In biological systems, these dendritic patterns may be found at dimensional length scales measured in meters (trees), millimeters/centimeters (fungi) or microns (neurons). One of the reasons for such extensive mimicry of these dendritic topologies is that they manifest maximum interfaces for energy and nutrient extraction/distribution and for information storage/retrieval. At the nanoscale level, there are relatively few natural examples of this architecture. Examples are the glycogen's and the proteoglycans' hyperbranched structure for energy storage.

In chemistry, at least three major strategies are presently available for covalent synthesis of organic and related complexes beyond the atomic level, namely: *traditional organic chemistry*, *traditional polymer chemistry* and *dendritic macromolecular chemistry*. On the one hand, traditional organic chemistry leads to higher complexity by involving the formation of relatively few covalent bonds between small heterogeneous aggregates of atoms (reagents) to give well-defined small molecules. On the other hand, polymerization strategies involve the formation of relatively few covalent bonds between homogeneous monomers to produce large molecules with a broad range of structure control. All dendritic polymers are open covalent assemblies of branch cells. There are three dendritic subclasses (Fig. 1.1): random hyperbranched polymers, dendrigraft polymers and dendrimers [6]. The order of this subset reflects the relative degree of structural control present in each of these dendritic architectures. In fact, hyperbranched polymers are polymers having imperfectly branched or irregular structures; dendrigrafts are the most recently discovered and currently the least well understood subset of dendritic polymers: they may be viewed as semi-controlled branched polymer architectures intermediate in terms of structure control between dendrimers and hyperbranched polymers. They most

often incorporate randomly distributed branching points, but are still characterized by narrow molecular weight distributions. Lastly, dendrimers have completely branched star-like topologies and display ordered structures with a high degree of reproducibility. Both dendrimer and hyperbranched polymer molecules are composed of repeating units emanating from a central core. In the following, I will restrict attention only on the third subclass, the one of dendrimers, which are the main subject of this thesis work.

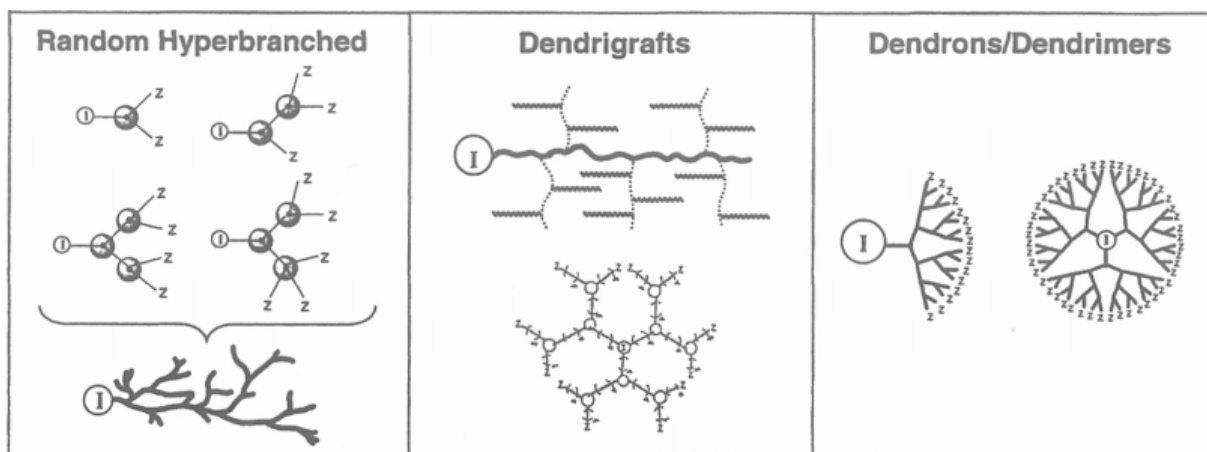


Figure 1.1: Dendritic polymers: from left to right, random hyperbranched polymers, dendrigrafts and dendrimers.

1.2 Dendrimers: chemistry and structure.

Dendrimers are globular, nano-scaled macromolecules with a particular architecture constituted of three distinct domains, as illustrated in Fig. 1.3:

1. A central core which is either a single atom or an atomic group having at least two identical end groups;
2. An interior of shells consisting of repeating branch-cell units having at least one branch junction: their repetition is organized in a geometrical progression that results in a series of radially concentric layers called *generations* (Fig. 1.4);
3. Many terminal functional groups, generally located in the exterior of the macromolecule, which play a key role in the dendrimer's properties.

The name *dendrimer* is derived from the Greek words *dendri* (branch tree-like) and *meros* (part of). In the past decade, over 2000 literature references have appeared on this unique class of structure controlled polymers. Poly(amidoamine) (PAMAM) dendrimers constitute the first commercialized dendrimer family and undoubtedly represent the most extensively characterized and best understood series at this time. The core of PAMAM is a diamine (commonly ethylenediamine), which is reacted with methyl acrylate and another ethylenediamine to make the generation-0 (*G-0*) PAMAM (see Fig 1.2). Successive reactions create higher generations, which tend to have different properties.

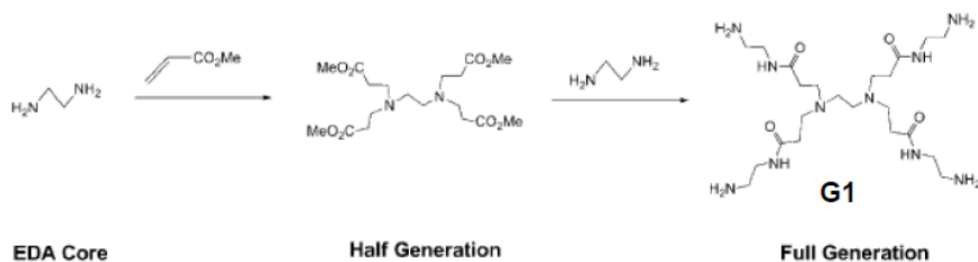


Figure 1.2: PAMAM dendrimer production reaction: the ethylenediamine core reacts with methyl acrylate and another ethylenediamine yielding the G-0 PAMAM. In the figure, Me indicates a Methyl $-\text{CH}_3$ group.

Intermediates during the dendrimer synthesis are denoted *half-generations*. The early generations ($G = 1 - 3$) possess a highly asymmetric, open, hemispherical shape, while the later generations ($G \geq 4$) possess a nearly spherical shape with dense-packed surface. Lower generations can be thought of as flexible molecules with no appreciable inner regions, while medium sized ($G-3$ or $G-4$) do have internal space that is essentially separated from the outer shell of the dendrimer. Very large ($G-7$ and greater) dendrimers can be considered more like solid particles with very dense surfaces due to the structure of their outer shell. The amine functional group on the surface of PAMAM dendrimers (Fig. 1.5) gives rise to many potential applications since they can be easily functionalized with any moiety presenting a reactive carboxyl group. In this thesis work we decided to employ this type of dendrimers; further description of the materials will be reported in Chapter 3, Section 3.2. The concept of repetitive growth with branching at molecular level was first reported in 1978 by Vögtle [7] (University of Bonn, Germany) and was followed closely by the parallel and independent development of the divergent, macromolecular synthesis (explained in Subsection 1.2.1) of true dendrimers in the Tomalia Group [8] (Dow Chemical Company). The first paper describing in detail the preparation of Poly(amidoamine) (PAMAM) dendrimers with molecular weights ranging from several hundred to over 1 million Daltons appeared in 1985 [9]. The appearance of this paper produced a rise of interest in dendritic polymeric architectures, although many of the major scientific journals tepidly welcomed the illustrated results. Indeed, at first they did not consider dendrimers such a promising discovery, neither believed them to exhibit new and perhaps unexpected physical-chemical properties different from other kinds of polymers. Fortunately, these initial suspicions were refuted in the subsequent years as dendrimers have become the subject of more and more studies and publications, and today many hundreds of research groups from diverse scientific disciplines have joined the field, leading to numerous advances in the synthesis, analysis and applications of these polymers [6].

1.2.1 Synthesis: Divergent and Convergent Methods

The methods for assembling the dendrimers can be categorized as either **divergent** or **convergent**; both synthetic processes can control precisely the size and number of

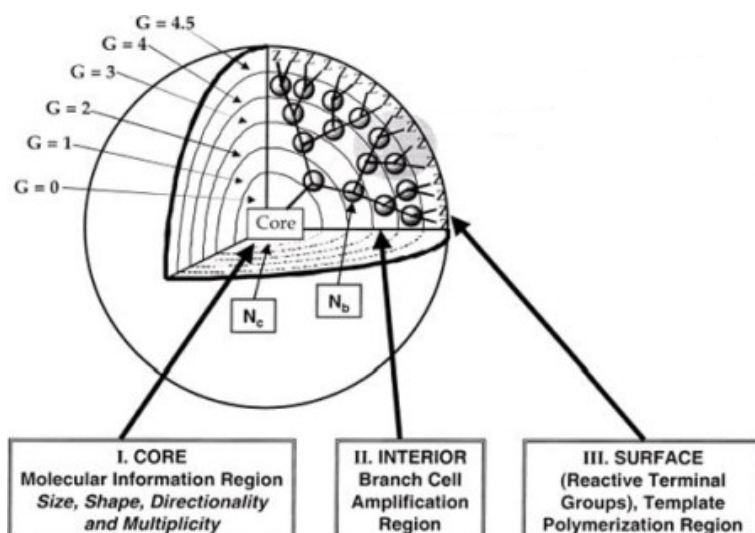


Figure 1.3: Schematic three-dimensional projection of dendrimer-core shell architecture for $G=4.5$ poly(amidoamine) PAMAM dendrimer with principal architectural components (I) core, (II) interior and (III) surface. The quantities N_c and N_b will be defined in Section 1.3 of this Chapter.

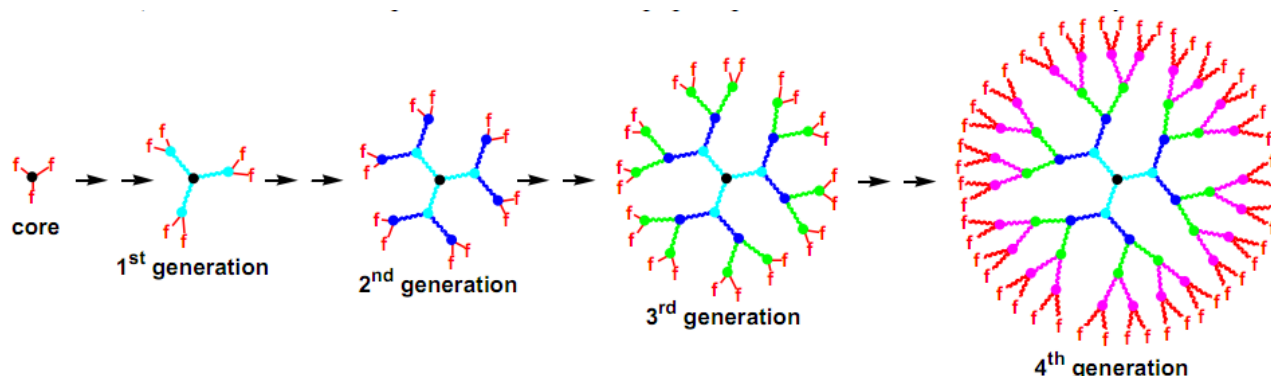


Figure 1.4: Schematization of the concept of *generation* of a dendrimer.

branches on the dendrimer. The first dendrimers were made by divergent synthesis approaches; in 1990 a convergent synthetic approach was introduced by Jean Fréchet. Fig. 1.6 illustrates both the *divergent* and the *convergent* method: in the former, the dendrimer is assembled from a multifunctional core, which is extended outward by a series of reactions; each step of the reaction must be driven to full completion to prevent mistakes in the dendrimer, which can cause architectural defects (for example, some branches could be shorter than others); in the second, dendrimers are built from small molecules that end up at the surface of the sphere, and the reactions proceed inward up to the final attachment to a core. This method makes it much easier to remove impurities and shorter branches along the way, so that the final dendrimer is more monodisperse. However dendrimers made this way are not as large as those made by divergent methods because are more subject to crowding due to steric effects. Ideally, a dendrimer can be synthesized to have different functionality in each of its three portions (core, interior and surface) to control properties such as solubility, thermal stability, and attachment of compounds for particular applications. PAMAM dendrimers are synthesized by the divergent approach.

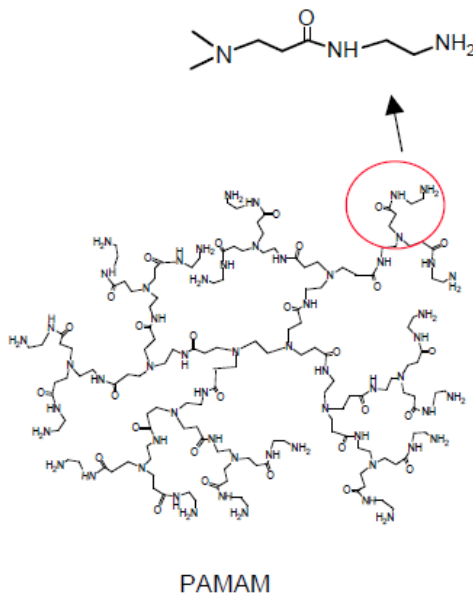


Figure 1.5: G-2 poly(amidoamine) (PAMAM) dendrimer and detail of the amine terminal group.

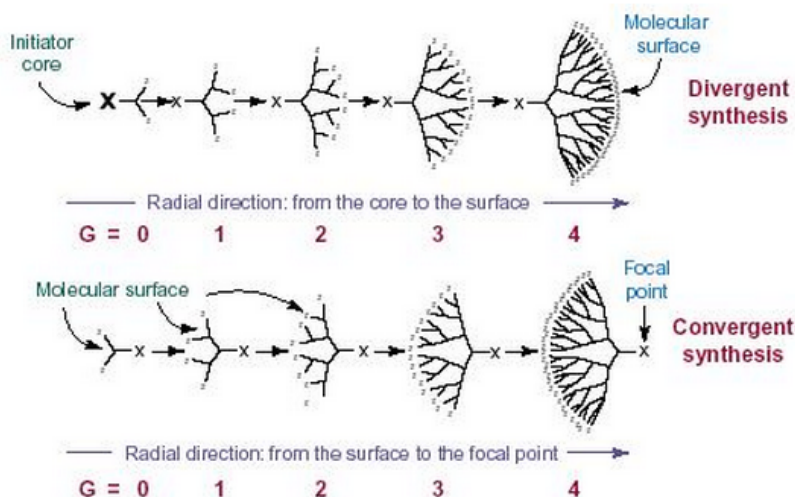


Figure 1.6: Schematic of *divergent* and *convergent* synthesis of dendrimers.

1.3 Unique Features of Dendrimers.

Dendrimers are unique nanoscale devices. Their three components (core, interior and terminal groups) determine their physical-chemical properties, as well as the overall size, shape and flexibility. It is important to note that dendrimer diameters increase linearly as a function of generation, while the number of surface functional groups increases exponentially. We define now two quantities of interest to describe the dendrimer structural properties: the core multiplicity N_c and the branch cell multiplicity N_b , the number of arms (dendrons) anchored to the core and to branch cells (generations), respectively .

These quantities contribute to determine the precise number of terminal groups Z and of covalent bonds formed as a function of generation G , according to

$$Z = N_c N_b^G \quad (1.1)$$

$$N_{bonds} = N_c \frac{N_b^G - 1}{N_b - 1} \quad (1.2)$$

The surface groups (Z) and number of bonds amplify mathematically according to a power function of the generation, producing structures with precise molecular weights, as shown in Table 1.1.

Gen	No. of NH Surface Groups	Molecular Formula	MW
0	4	$C_{24}H_{52}N_{10}O_4S_2$	609
1	8	$C_{64}H_{132}N_{26}O_{12}S_2$	1,522
2	16	$C_{144}H_{292}N_{58}O_{28}S_2$	3,348
3	32	$C_{304}H_{612}N_{122}O_{60}S_2$	7,001
4	64	$C_{624}H_{1252}N_{250}O_{124}S_2$	14,307
5	128	$C_{1264}H_{2532}N_{506}O_{252}S_2$	28,918
6	256	$C_{2544}H_{5092}N_{1018}O_{508}S_2$	58,140
7	512	$C_{5104}H_{10212}N_{2042}O_{1020}S_2$	116,585

Table 1.1: Theoretical number of surface groups (Z), molecular formulas and weights calculated by means of Eqs. 1.1, 1.2 for a PAMAM dendrimer, cystamine core. The molecular weights approximately double as one progresses from one generation to the next.

1.3.1 Comparison with Traditional Polymers

Unique features offered by dendrimers that have no equivalency in the linear topologies include:

1. Nearly complete monodispersity (the property of an ensemble with constituents all with the same mass): although, in general, convergent methods yield the most nearly isomolecular dendrimers, mass spectroscopy has shown that PAMAM dendrimers produced by the divergent method are very monodisperse;
2. The display of unimolecular container/scaffolding properties;
3. Exponential amplification of terminal functional groups;
4. Persistent nanoscale dimensions as a function of molecular weight (generation).

Apart from those reported above, which are exclusive characteristics of dendrimers, the dendritic architecture presents other properties which differ from those of linear polymers; let's list the most peculiar of these: first, the solubility of the latter decreases with molecular weight, whereas for dendrimers it increases; second, in contrast to what normally observed for linear polymers, viscosities of dendrimers do not increase continuously with

molecular weight, but reach a maximum at a certain generation; lastly, dendrimers present isotropic electronic conductivity, whereas linear polymers usually show an anisotropic electronic conductivity. To conclude, I shall say that the properties of dendrimers result in

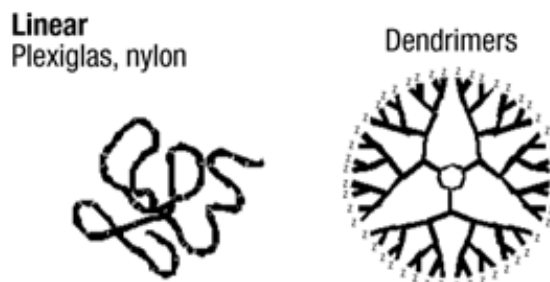


Figure 1.7: Schematic comparison of a common linear polymer (like plexiglas or nylon) and a dendrimer.

large part dominated by the functional groups on the molecular surface; however, there are examples of dendrimers with internal functionality [10]. It is possible to make dendrimers water soluble, unlike most polymers, by functionalizing their outer shell with charged species or other hydrophilic groups. Other controllable properties of dendrimers include toxicity, crystallinity, and chirality [11].

1.4 Dendrimers for Biological Applications

The last decades have seen research at the interface between polymer chemistry and the biomedical sciences giving birth to the first nano-sized (5-100 nm) polymer-based pharmaceuticals. This family of constructs has been called "polymer therapeutics". Polymer therapeutics are complex technologies, often combining several components, *e.g.*, polymers, drugs, peptides, proteins and others. [12] The advent of dendrimer chemistry has brought many potential advantages to this new approach to therapeutics. In fact, unlike traditional polymers, dendrimers can be obtained in precise molecular weights even at high generations, which can provide a reproducible pharmacokinetic behavior. Plus, it is possible to conjugate other chemical species to the dendrimer surface in order to serve as detecting agents (such as a dye molecule), targeting components, imaging agents, or pharmaceutically active compounds. Recently, progress has been made also in the application of biocompatible dendrimers to cancer treatment, including their use as delivery systems for potent anticancer drugs. The field of biomedical dendrimers is still in its infancy, but the interest in dendrimers as active therapeutic agents, as vectors for targeted delivery of drugs, peptides and oligonucleotides, and as permeability enhancers able to promote oral and transdermal drug delivery is increasing at a fast rate. Scientists have also studied dendrimers for use in sensor technologies. Studied systems include pH or ionic sensors using dendrimer-dye composites to detect fluorescence signal quenching. We exploit this sensor feature of dendrimer-dye(s) systems later in this thesis, in Chapter 3, Section ??.

Research in this field is vast and ongoing due to the potential for multiple detection and

binding sites in dendritic structures.

1.4.1 Drug Delivery

The physical characteristics of dendrimers, including their monodispersity, water solubility, encapsulation ability, and large number of functionalizable peripheral groups, make these macromolecules appropriate candidates for evaluation as drug delivery vehicles. Dendrimers have very strong potential for this application because, as already mentioned, their structure can lead to multivalent systems. In other words, one dendrimer molecule has hundreds of possible sites for coupling to active species. There are presently three methods for using dendrimers in drug delivery, as shown by Fig. 1.8: the drug can be covalently attached to the periphery of the dendrimer, coordinated to the outer functional groups via ionic interactions, or the dendrimer itself can act as a unimolecular micelle by encapsulating a pharmaceutical through the formation of a dendrimer-drug supramolecular assembly [13]. Indeed, dendrimers with hydrophobic core and hydrophilic periphery have shown to exhibit micelle-like behavior and container properties in solution [14]. This analogy highlighted the utility of dendrimers as solubilizing agents: in fact, the majority of drugs available in pharmaceutical industry are hydrophobic. This drawback of drugs can be obviated by dendrimeric scaffolding, which can be used to encapsulate as well as to solubilize the drugs because of the capability of such scaffolds to participate in extensive hydrogen bonding with water [15, 16]. The encapsulation increases with dendrimer generation and this method may be useful to entrap drugs with a relatively high therapeutic dose. Studies based on dendrimers also open up new avenues of research into the further development of drug-dendrimer complexes specific for a cancer and/or targeted organ system.

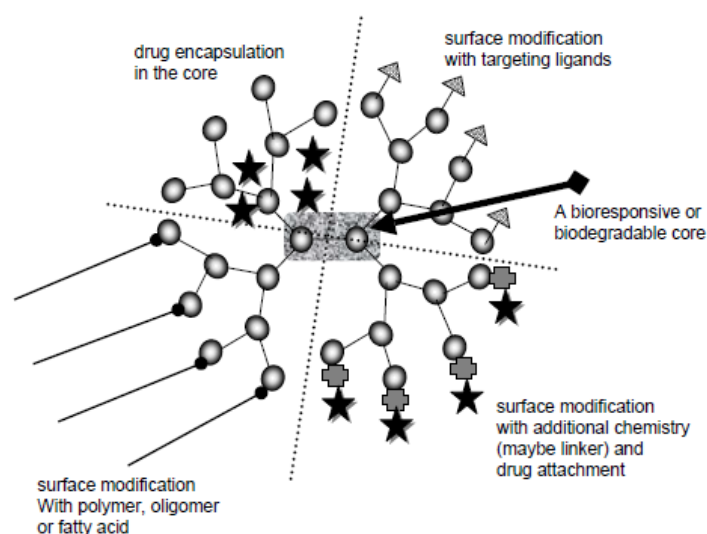


Figure 1.8: Diagram showing schematically approaches for design of therapeutics and drug delivery systems [12].

1.4.2 Gene Delivery

Gene delivery is the process of introducing foreign DNA into host cells. It is one of the main steps of genetic therapies. There are many different methods for gene delivery developed for various types of cells (from bacterial to mammalian) and tissues. Generally, the methods can be divided into two categories, viral and non-viral. Virus mediated gene delivery utilizes the ability of a virus to inject its DNA inside a host cell. A gene that is intended for delivery is packaged into a viral particle. Non-viral methods include physical methods such as microinjection and electroporation. It can also include the use of polymeric gene carriers. The ability to deliver pieces of DNA to the required parts of a cell presents many challenges. Current research is being performed to find ways to use dendrimers to traffic genes into cells without damaging or deactivating the DNA. PAMAM dendrimers have revealed to be highly efficient non-viral vectors for gene delivery into numerous cell lines, *in vitro* and *in vivo*, both as functionalized and micelle-like carriers [17]: some of their generations can be internalized in cells without inducing biocompatibility issues or toxicity and this confers to PAMAM dendrimers a significant advantage over other gene delivery vectors for use *in vivo*.

1.4.3 Biocompatibility and Toxicity

Surveys regarding the toxicology of dendrimers for biological and cellular environments are currently under development. The cytotoxicity (quality of being toxic to cells) of unmodified PAMAM dendrimers was found to be appreciably higher for cationic compared with partially or totally uncharged dendrimers and for both types increased with increasing size (generation) and concentration [18]. It has been observed that surface modified dendrimers with carbohydrates should make it possible to avoid the cytotoxic effects of cationic and high-generation dendrimers and to reduce the toxicity in cells by reduction/shielding of the positive charge on the dendrimer surface [2]. In future it will only ever be possible to designate a dendrimer as "safe" when related to a specific application. The so far limited clinical experience using dendrimers makes it impossible to designate any particular intrinsically "safe" dendrimer. Although there is widespread concern as to the safety of nano-sized particles, preclinical and clinical experience gained during the development of polymeric excipients, biomedical polymers and polymer therapeutics shows that judicious development of dendrimer chemistry for each specific application will ensure development of safe and important materials for biomedical and pharmaceutical use.

Chapter 2

Light-Matter Interactions

Photoluminescence is the property of any substance of emitting photons from electronically excited states upon absorption of radiation of appropriate wavelength. In most cases, emitted light has a longer wavelength, and therefore lower energy, than the absorbed radiation. Photoluminescence includes the phenomena of **fluorescence** and **phosphorescence**, depending on the nature of the excited state.

Let's examine fluorescence first, the real protagonist of this thesis. Absorption occurs from the ground state of a molecule, which is usually a singlet state. In excited singlet states, the electron in the excited orbital remains "paired" (by opposite spin) to the second electron in the ground-state orbital. Decay to the ground state occurs by emission of a photon with rates typically around 10^8s^{-1} , so that a typical fluorescence lifetime is near 10 ns ($10 \times 10^{-9}\text{s}$). The lifetime (τ) of a fluorophore refers to the average time the molecule stays in its excited state.

Phosphorescence is emission of light from triplet excited states, in which the electron in the excited orbital has the same spin orientation as the ground-state electron. Transitions to the ground state are forbidden (at least in the electric dipole approximation) and the emission rates are slow ($10^3 - 1\text{ s}^{-1}$), so that phosphorescence lifetimes are typically milliseconds to seconds.

In short, fluorescence has immediate effect and stops immediately after the light source is turned off, while phosphorescence's effect continues even after cessation of the irradiation. Besides, phosphorescence is usually not seen in fluid solutions at room temperature. This is because there are many deactivation processes that compete with emission, such as non-radiative decay and quenching. We will consider them in more detail later in this chapter.

2.1 Primary and Secondary photophysical processes

At the beginning of the studies about the interactions between light and matter, Stark and Einstein stated that each molecule is excited by only one photon. Exceptions are the so-called *multiphoton processes*, in which the molecule absorbs two or more photons at the same time. The latter occur exclusively when the energy difference between the involved

states of the molecule is equal to the sum of the energies of the two photons. Two-photon absorption is a second-order, nonlinear process and differs from linear absorption also because the probability of absorption depends on the square of the light intensity. Moreover, it is usually several orders of magnitude weaker than linear absorption.

Following excitation, a molecule may undergo chemical reactions, and in this case the process is called "photochemical", or it may not, and it is then called a "photophysical" process. In general, we write: $A + h\nu \longrightarrow A^*$ where the star indicates a species which is in an electronic excited state. All the processes that directly involve the A^* species are classified as "primary" [19]. A list is reported below.

- Luminescence (radiation emission): $A^* \longrightarrow A + h\nu'$
Usually the emitted photon has a longer λ than the exciting one ($\nu' < \nu$) because part of the energy is lost in other ways.
- Ionization: $A^* \longrightarrow A^+ + e^-$
It generally requires high energies (8-10 eV in organic molecules) and the eventual energy in excess may convert to kinetic energy of the emitted electron.
- Non-radiative decay: $A^* \longrightarrow A$
No photon has been emitted returning to the electronic ground state, nor any chemical reaction has occurred. Evidently, the molecule still possesses a certain amount of energy in the form of vibrations, which may be dispersed by collisions with the surrounding environment. This energy dissipation occurs with production of heat.
- De-activation or Quenching: $A^* + B \longrightarrow A + B$
Deactivation or non-radiative decay depend on the presence of another species B (See also Section 2.4.3).
- Energy Transfer: $A^* + B \longrightarrow A + B^*$
This can occur without exchange of a photon (see Fluorescence Resonance Energy Transfer in section 2.4.4 of this chapter).
- Photoisomerization: $A^* \longrightarrow B$
The A species turns into the B isomer, eventually in its ground state. The energy in excess can be dissipated through interactions with other molecules.
- Photodissociation: $A^* \longrightarrow B + C$
Part of the incident photon's energy is used to break the bond between B and C fragments, and the remainder goes in kinetic and translational energy of B and C.
- Bimolecular reaction: $A^* + B \longrightarrow C + D$
As the reagents typically contain energy in excess with respect to the reaction products, the latter would probably disperse this excess by collisions.

Many of the products listed above possess enough energy left to undergo further physical-chemical processes, called "secondary" since they do not directly involve the A species.

2.2 Radiation Absorption and B Einstein coefficients

Light is a propagating oscillating electromagnetic field. Molecules contain distributions of charges and spins that are altered when they are exposed to light. We are usually interested in the rate at which the molecule responds to this perturbation. In the following, I shall restrict attention only to the electric field of light, although more rigorous treatments include magnetic effects as well. A typical chromophore (a molecular moiety that interacts with light) is small ($\sim 10\text{\AA}$) compared to the wavelength of light (say 5000\AA); thus one can ignore the spatial variation of the electric field within the molecule. The oscillating electric field can then be written as

$$\mathbf{E}_0 = \mathbf{E}_0 e^{i\omega t} \quad (2.1)$$

where \mathbf{E}_0 is the maximum amplitude and ω is equal to $2\pi\nu$ with ν frequency of the electric field in Hz. Suppose our system is originally in state Ψ_a , an eigenstate of the time-independent Hamiltonian $\hat{\mathbf{H}}$ with energy E_a ; light perturbs the system causing transitions between Ψ_a and other states at a certain *rate*. In general, in quantum physics, **Fermi's golden rule** is used to calculate the transition rate (probability of transition per unit time) from one eigenstate n with energy E_n of a quantum system to another eigenstate m with energy E_m , due to a perturbation W :

$$P_{n \rightarrow m} \sim \frac{2\pi}{\hbar} |\langle \Psi_n | W | \Psi_m \rangle|^2 \delta(E_m - E_n \pm \hbar\omega) \quad (2.2)$$

where δ is the Dirac Delta functional. In order to derive the result, let's consider a hypothetical molecule with only two states, Ψ_a and Ψ_b . Because light is a time-dependent interaction, the time-dependent Schrödinger's equation must be solved. The Hamiltonian can be written as

$$\hat{\mathbf{H}}' = \hat{\mathbf{H}} + \hat{\mathbf{V}}(t) \quad (2.3)$$

where the effect of the light appears entirely in $\hat{\mathbf{V}}(t)$. The wavefunction of the system in the presence of light must be a linear combination of the two states, with time-dependent coefficients:

$$\Psi(t) = C_a(t)\Psi_a e^{-iE_a t/\hbar} + C_b(t)\Psi_b e^{-iE_b t/\hbar} \quad (2.4)$$

Inserting this expression into the time dependent Schrödinger equation with Hamiltonian 2.3, we obtain (after some algebra):

$$i\hbar(\Psi_a e^{-iE_a t/\hbar} dC_a/dt + \Psi_b e^{-iE_b t/\hbar} dC_b/dt) = \hat{\mathbf{V}}(t)[\Psi_a e^{-iE_a t/\hbar} C_a(t) + \Psi_b e^{-iE_b t/\hbar} C_b(t)] \quad (2.5)$$

Multiplying by $\Psi_a^* e^{iE_a t/\hbar}$ or $\Psi_b^* e^{iE_b t/\hbar}$ and integrating over spatial coordinates, we obtain two equations to evaluate $C_a(t)$ and $C_b(t)$:

$$i\hbar dC_a/dt = \langle \Psi_a | \hat{\mathbf{V}} | \Psi_a \rangle C_a + \langle \Psi_a | \hat{\mathbf{V}} | \Psi_b \rangle C_b e^{-i(E_b - E_a)t/\hbar} \quad (2.6)$$

$$i\hbar dC_b/dt = \langle \Psi_b | \hat{\mathbf{V}} | \Psi_a \rangle C_a e^{-i(E_a - E_b)t/\hbar} + \langle \Psi_b | \hat{\mathbf{V}} | \Psi_b \rangle C_b \quad (2.7)$$

The integrals symbolized by the angle brackets are taken over spatial coordinates only. To proceed further, let's insert an explicit form for the perturbing potential $\hat{\mathbf{V}}(t)$. As already said, a molecule is perturbed by light because its distribution of electric charge is altered by the presence of the oscillating electric field \mathbf{E} ; for electrically neutral molecules, this charge distribution is in good approximation represented by the electric dipole, which in quantum mechanics is described by the operator $\hat{\mu} = \sum_i e_i \mathbf{r}_i$ where the sum runs over each electronic charge e_i at position \mathbf{r}_i . I will consider only the electronic part of the wavefunction, since the positions of nuclei are assumed to be fixed and thus can be ignored. Let's calculate now the transition rate from the state a to the state b: Imposing $|C_b(0)|^2 = 0$ and $|C_a(0)|^2 = 1$, the Eq. 2.6 becomes:

$$i\hbar dC_b/dt = C_a \langle \Psi_b | \hat{\mu} | \Psi_a \rangle \cdot \mathbf{E}_0 e^{-i(E_a/\hbar - E_b/\hbar - \omega)t} \quad (2.8)$$

where \mathbf{E}_0 has been removed from the integrals because it is constant over the dimensions of the molecules.

Let's now calculate the probability P_b that the system is in state b at time t. The result, for small \mathbf{E}_0 and, again, imposing $|C_b(0)|^2 = 0$ is:

$$P_b = |C_b(t)|^2 = \frac{|\langle \Psi_b | \hat{\mu} | \Psi_a \rangle \cdot \mathbf{E}_0|^2 t^2 \sin^2[(E_b/\hbar - E_a/\hbar - \omega)t/2]}{\hbar^2 2[(E_b/\hbar - E_a/\hbar - \omega)t/2]^2} \quad (2.9)$$

For $t \rightarrow \infty$, we have that

$$\frac{t^2 \sin^2[(E_b/\hbar - E_a/\hbar - \omega)t/2]}{2[(E_b/\hbar - E_a/\hbar - \omega)t/2]^2} \longrightarrow 2\pi t \delta(E_b/\hbar - E_a/\hbar - \omega) \quad (2.10)$$

where $\delta(E_b/\hbar - E_a/\hbar - \omega)$ is a Dirac Delta functional. Because $\hbar\omega$ is the energy of the light, transitions from a to b will be induced only when $\hbar\omega = h\nu = E_b - E_a$ with $E_b - E_a$ energy separation between the two states. The rate at which these transitions occur is just the rate of change of $|C_b(t)|^2$ in response to illumination with radiation centered about frequency ν , and it is constant for large values of t, since the probability for the molecule being in state b increases linearly with time. We can write the transition rate dP_b/dt as a product of two terms

$$dP_b/dt = B_{ab}U(\nu) \quad (2.11)$$

where B_{ab} is the transition rate per unit energy density of the radiation and $U(\nu)$ is the energy density incident on the sample at frequency ν . Recalling that $U(\nu) = |\mathbf{E}_0|^2/4\pi$ and that the average of $|\langle \Psi_b | \hat{\mu} | \Psi_a \rangle \cdot \mathbf{E}_0|^2$ over all possible orientations of the molecules dipole moments is just $(1/3)|\langle \Psi_b | \hat{\mu} | \Psi_a \rangle|^2 |\mathbf{E}_0|^2$, we can evaluate B_{ab} :

$$B_{ab} = (2/3)(\pi/\hbar^2) |\langle \Psi_b | \hat{\mu} | \Psi_a \rangle|^2 \quad (2.12)$$

Noting that, following the same procedure, it is possible to determine also B_{ba} , the rate

at which energy is removed from the light will be

$$-dU(\nu)/dt = h\nu(N_a B_{ab} - N_b B_{ba})U(\nu) \quad (2.13)$$

where N_a and N_b are the number of molecules per cm^3 in states a and b, respectively. The quantities B_{ab} and B_{ba} are called **Einstein coefficients** for absorption and stimulated emission, respectively; it is $B_{ab} = B_{ba}$ [20].

2.2.1 The Extinction Coefficient

In a typical light-absorption measurement, a monochromatic beam of intensity I_0 and wavelength λ impinges on a sample (usually a solution of sample molecules with known concentration in mol l^{-1}) for a path length of l cm; the not-absorbed light has intensity $I < I_0$, and is collected by an appropriate detector.

Consider a beam of light propagating perpendicularly to a layer of sample molecules thin enough (dl) to suppose the light intensity within it constant; then the fraction of light that is absorbed is

$$-dI/I = C\varepsilon' dl \quad (2.14)$$

where ε' is called the **molar extinction coefficient**: it is independent of concentration for non-interacting molecules but is function of the frequency (or the wavelength) of the absorption spectrum. Integrating the left member of Eq. 2.12 between I_0 and I and the right one between 0 and l , we obtain

$$\ln(I_0/I) = C\varepsilon' l \quad (2.15)$$

Converting this expression to \log_{10} , we derive the well-known **Lambert-Beer Law**

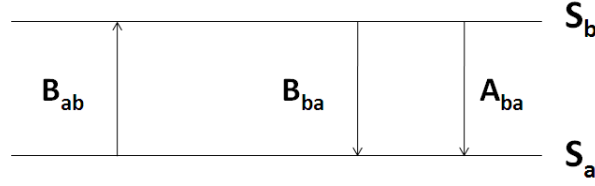
$$A(\lambda) \equiv \log_{10}(I_0/I) = c\varepsilon(\lambda)l \quad (2.16)$$

with $\varepsilon = \varepsilon'/2.303$ and A absorbance or optical density of the sample. ε is usually measured in $\text{l mol}^{-1}\text{cm}^{-1}$ and usually spaces between 1 and more than $10^5 \text{ l mol}^{-1}\text{cm}^{-1}$. Looking at Eq. 2.16, we conclude that concentrations $\sim \mu\text{M}$ should be used for absorption measurements in cuvettes with a 1 cm path length (lateral dimension) in order to have $A \sim 0.1$.

2.3 Spontaneous Emission and A Einstein coefficient

Consider again a molecule with only two energy levels S_b and S_a : As already said in the previous section, $B_{ab} = B_{ba}$.

If originally there are n_a molecules in state S_a and n_b in S_b , then the net rates of conversion from a to b and b to a are $n_a B_{ab} U(\nu)$ and $n_b B_{ba} U(\nu)$, respectively. At equilibrium, these rates must be equal, which implies $n_a = n_b$, independent of radiation density. This is an absurd result: in fact, in absence of incident radiation, all molecules should be in



the ground state S_a . It was Einstein who first proposed that, in order to resolve this discrepancy, one could postulate a rate of spontaneous emission of photons from S_b . The rate of this process A_{ab} is called the Einstein spontaneous emission coefficient and should be independent of $U(\nu)$. When spontaneous emission is included and at equilibrium, we have

$$n_a/n_b = [B_{ba}U(\nu) + A_{ba}]/(B_{ab}U(\nu)) = 1 + A_{ba}/(B_{ab}U(\nu)) \quad (2.17)$$

Recalling that, according to the Boltzmann statistics, at thermal equilibrium it must be $n_a/n_b = e^{-(E_a-E_b)/KT} = e^{h\nu/KT}$, with $K = 1.38 \times 10^{-23} \text{ JK}^{-1}$ Boltzmann constant, and that at thermal equilibrium the energy density distribution of the electromagnetic radiation is that of a black body $U(\nu) = 8\pi h\nu^3/[c^3(e^{h\nu/KT} - 1)]$, we obtain:

$$n_a/n_b = (1 + A_{ba}(e^{h\nu/KT} - 1)c^3)/(8\pi h\nu^3 B_{ab}) \quad (2.18)$$

and setting this value equal to $e^{(h\nu/KT)}$

$$A_{ba} = 8\pi h\nu^3 c^{-3} B_{ab} \quad (2.19)$$

Note that the dependence of A_{ba} by the cube of the frequency causes most of the emission to be due to spontaneous decay at the highest photon energies.

In the absence of radiation or any other type of de-excitation, it will be $dn_b/dt = -A_{ba}n_b$, with solution $n_b(t) = n_b(0)e^{-A_{ba}t}$ with $n_b(0)$ population of state b at zero time. Thus, it is possible to define the **radiative lifetime** or *natural lifetime* of S_b as

$$\tau_R = 1/A_{ba} \quad (2.20)$$

From Eqs. 2.19-2.20 derives that the stronger the absorption, the faster the emission of fluorescent radiation. In general, the lifetime of the excited state is defined by the average time the molecule spends in the excited state before returning to the ground state (typically times of ns). Note that Eq. 2.17 is valid only if the electronic state couple involved in absorption and emission is the same. In fact, this is not always the case, and more complex expressions have been developed to account for this.

The radiative (fluorescence) rate constant (k_F) is equal to $1/\tau_R$ and so we have

$$k_F = A_{ba} \quad (2.21)$$

as long as stimulated emission is negligible.

2.4 Emission spectra and their properties

Absorption is an event which occurs so fast - $\sim 10^{-15}\text{s}$ - that there is no time for molecular motion or for significant displacement of nuclei during it (**Franck Condon principle**). As a result, absorption spectroscopy can only yield information on the average structure of the molecules that absorb light and absorption spectra are not sensitive to molecular dynamics but can only provide information on the average local environment surrounding the chromophore. Only solvent molecules that are immediately adjacent to the absorbing species will affect its absorption spectrum. Light emission can reveal properties of biological molecules quite different from the ones revealed by light absorption. The process takes place on a much slower time scale, allowing a much wider range of interactions and perturbations to influence the spectrum. A fluorescence emission spectrum is a plot of the fluorescence intensity versus the wavelength λ (nm) or the wavenumber $k = 1/\lambda$ (cm^{-1}) of emitted light. The following sections will examine in more details the characteristics of fluorescence and the main factors that affect the emission intensity.

2.4.1 Jablonski Diagrams

The transitions between electronic states are usually displayed by the **Jablonski diagrams**, named after Professor Alexander Jablonski, who is regarded as the father of fluorescence spectroscopy. In this schemes, each molecular level is indicated by a horizontal line, and the electronic levels are actually split in several horizontal parallel lines, to represent the partition in rotational and vibrational sublevels. In Figure 2.2, radiative transitions (absorption, fluorescence, phosphorescence) are drawn as coloured arrows, non-radiative ones as black arrows. Horizontal arrows indicate processes that conserve energy, like conversions, e.g. from electronic to vibrational excited states in **Internal Conversion (IC)** and **InterSystem Crossing (ISC)**, whilst vertical and oblique ones indicate exchange of energy with the electromagnetic field (absorption, stimulated emission, photoluminescence) or with other molecules (collisions, solvent interactions). The non-radiative processes of Internal Conversion and InterSystem Crossing are outlined in more detail in the following subsections.

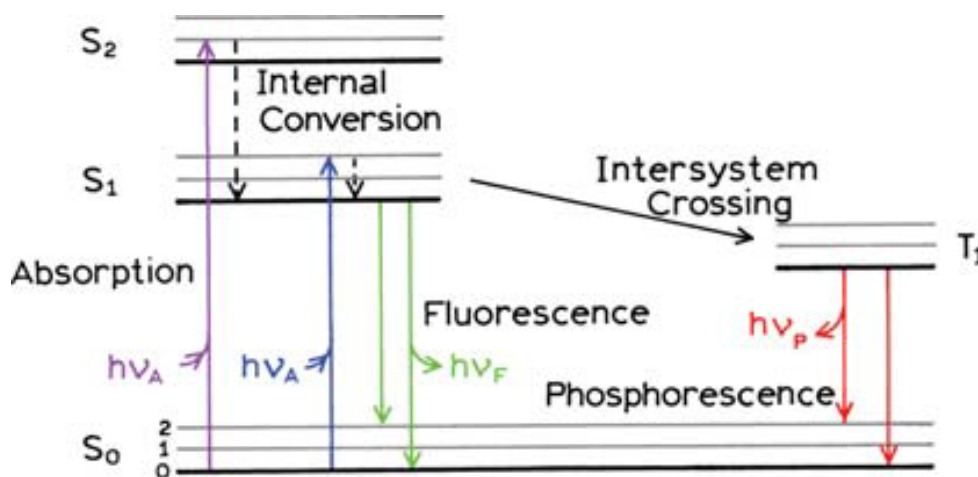


Figure 2.1: General form of a Jablonski diagram: it does not include non-radiative interactions such as quenching, energy transfer, and solvent interactions.

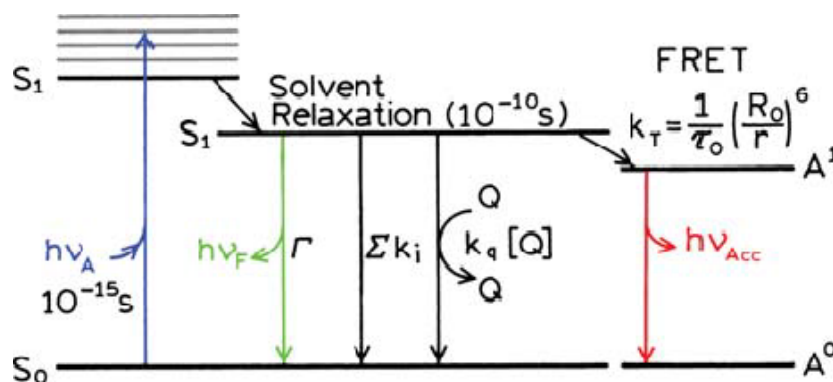


Figure 2.2: Jablonski diagram with collisional quenching and fluorescence resonance energy transfer (FRET). The term $\sum k_i$ represents non-radiative decay channels aside from quenching and FRET.

2.4.2 Internal Conversion and Kasha's Rule

Following radiation absorption, a fluorophore is excited to some vibrationally excited state of a higher electronic level S_N . The decay from a molecular state to a lower one with the same spin multiplicity is called **Internal Conversion (IC)**. It is due to loss of energy by collisions with solvent or by dissipation through internal vibrational modes and thus increases as the temperature is raised. This process has typical times of 10^{-12} s or less, and thus occurs prior to emission, since fluorescence lifetimes, as already said, are around $10^{-9} - 10^{-8}$ s. Hence, fluorescence emission generally results from a thermally equilibrated excited state, that is, the lowest energy vibrational state of S_1 . This causes the **Kasha's Rule**, which states that *the fluorescence spectrum is independent from the excitation wavelength*; similarly, the quantum yields of most of the primary processes are also independent from the excitation wavelength. After excitation, the fluorophore returns to the electronic ground state, but usually on a vibrational level of higher energy, which then thermally relaxes to the fundamental one in about 10^{-12} s. A consequence of the

processes explained above is that the energy of the emitted photon is usually lower than for the absorbed one. Another interesting consequence of emission to higher vibrational ground states is that the emission spectrum is typically a mirror image of the absorption spectrum of the $S_0 \rightarrow S_1$ transition. This similarity occurs because electronic excitation does not greatly alter the nuclear geometry. Hence the spacing of the vibrational energy levels of the excited states is similar to that of the ground state. As a result, the vibrational structures seen in the absorption and the emission spectra are similar.

2.4.3 InterSystem Crossing and Phosphorescence

Molecules in the S_1 state can also undergo a spin conversion to the first triplet state T_1 . Emission from T_1 can occur either by **phosphorescence**, or by internal conversion, and, since the triplet state generally is lower in energy than the excited singlet, phosphorescence is usually shifted to longer wavelengths relative to fluorescence. Conversion of S_1 to T_1 is an example of **Intersystem Crossing (ISC)**. Transition from T_1 to the singlet ground state is forbidden in electric dipole approximation, and as a result the rate constants for triplet emission are several orders of magnitude smaller than those for fluorescence, and therefore the triplet state will display an extremely long radiative lifetime (seconds or longer instead of nanoseconds typical of excited singlets). This means that collisions with other molecules or internal conversion can effectively compete with phosphorescence. This is why it is rarely observed in solution, but rather in solid and de-oxygenated samples, conditions very far from the biological ones in which we are interested.

2.4.4 Quenching of Fluorescence

Fluorescence quenching refers to any process that decreases the fluorescence intensity of a sample. The extent of quenching can be affected by the environment surrounding the fluorophore; in fact, a variety of molecular interactions can result in quenching. These include excited-state reactions, molecular rearrangements, energy transfer, ground-state complex formation, and collisional quenching. The latter occurs when the excited-state fluorophore is deactivated upon contact with some other molecule in solution, which is called the quencher. The molecules are not chemically altered in the process. When many fluorophore molecules are really close, they may also undergo *self-quenching*, which in general is quenching of an excited atom or molecular entity by interaction with another atom or molecular entity of the same species. This concept will be resumed in Chapter 4. For collisional quenching the decrease in intensity is described by the **Stern-Volmer equation**:

$$\frac{F_0}{F} = 1 + K[Q] = 1 + k_Q\tau_0[Q] \quad (2.22)$$

where F_0 and F are the fluorescence intensities in the absence and presence of quencher, respectively, K is the Stern-Volmer quenching constant, which indicates the sensitivity of the fluorophore to a quencher, k_Q is the bimolecular quenching constant, τ_0 is the

lifetime of the fluorophore in the absence of quencher, and $[Q]$ is the quencher concentration. A fluorophore inserted in a macromolecule is usually inaccessible to water soluble quenchers, so that the value of K is low. Larger values of K are found if the fluorophore is free in solution or on the surface of a biomolecule, as in this thesis work. A wide variety of molecules can act as collisional quenchers. Examples include oxygen, halogens, amines. The mechanism of quenching varies with the fluorophore-quencher pair, but, in any case, it requires molecular contact between fluorophore and quencher. This contact can cause a (meta)stable nonfluorescent complex formation which produces the so-called *static quenching*, or can be due to diffusion or molecular collisions for the molecule in the excited state, fluorophore-solvent interactions and/or rotational diffusion (which will be described in Section 2.5), which result in *dynamic quenching* instead.

The measurement of fluorescence lifetimes is the most definitive method to distinguish static and dynamic quenching. Static quenching removes a fraction of the fluorophores from observation. The complexed fluorophores are nonfluorescent, and the only observed fluorescence is from the uncomplexed fluorophores. The uncomplexed fraction is unperturbed, and hence the lifetime is τ_0 . Therefore, defining τ as the time constant in presence of quencher, we have that for static quenching $\tau_0/\tau = 1$. In contrast, for dynamic quenching we have $F_0/F = \tau_0/\tau$.

One additional method to distinguish static and dynamic quenching can be based on careful examination of the absorption spectra of the fluorophore. Collisional quenching only affects the excited states of the fluorophores, and thus no changes in the absorption spectra are expected. In contrast, ground-state complex formation will frequently result in perturbation of the absorption spectrum of the fluorophore. In fact, a more complete treatment should include the possibility of different extinction coefficients for the free and complexed forms of the fluorophore. However, in many instances the fluorophore may be quenched both by collisions and by complex formation with the same quencher.

2.4.5 Resonance Energy Transfer (RET)

Another important process that occurs in the excited state and causes loss of energy is resonance energy transfer (RET), sometimes also called **Fluorescence Resonance Energy Transfer (FRET)**. This process can occur if the emission spectrum of a fluorophore, called the *donor*, overlaps with the absorption spectrum of another molecule, called the *acceptor*, in its close proximity and with proper orientation of the dipoles.

The acceptor does not need to be fluorescent. RET does not involve emission of light by the donor, is not the result of emission from the donor being absorbed by the acceptor; the donor and acceptor are coupled by a dipole-dipole interaction. For these reasons the term RET is preferred over the term fluorescence resonance energy transfer (FRET), which is also in common use. The extent of energy transfer is determined by the distance between the donor and acceptor, and the extent of spectral overlap. The latter is described in terms of the Förster distance R_0 , according to the following expression which we report

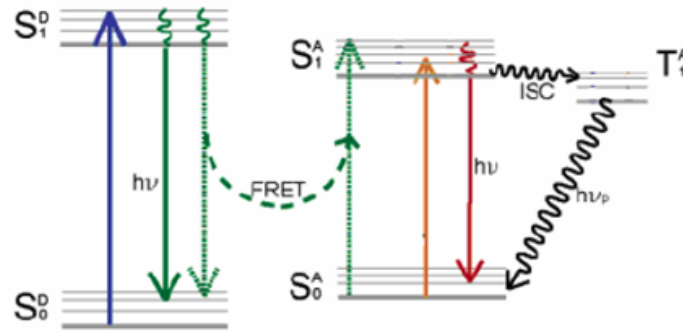


Figure 2.3: FRET Jablonski diagram showing energy transfer from the donor D to the acceptor A. Eventual InterSystem Crossing for the acceptor is also reported.

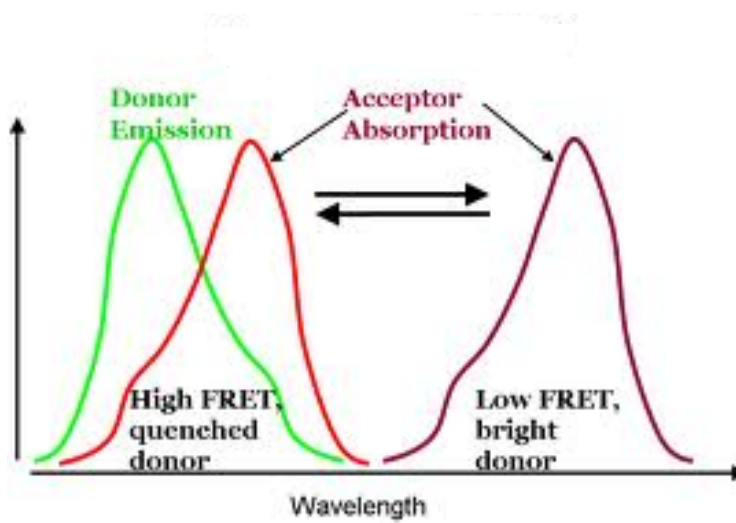


Figure 2.4: Example of two possible situations considering a FRET couple: if there is a spectral overlap between donor emission spectrum and acceptor absorption spectrum (left part of the figure) we have high fluorescence resonance energy transfer (RET) and donor quenching; if, instead, the two spectra do not overlap much (right part of the figure), there is low FRET and the donor's brightness remains unaltered.

here for completeness without derivation

$$R_0^6 \propto \frac{\kappa^2 Q_D}{nN} \int_0^\infty F_D(\lambda) \varepsilon_A(\lambda) \lambda^4 d\lambda \quad (2.23)$$

where Q_D is the quantum yield of the donor, n is the refractive index of the medium, N is the Avogadro's number and $F_D(\lambda)$ is the fluorescence intensity of the donor with the total intensity (area under the curve) normalized to unity. $\varepsilon_A(\lambda)$ is the extinction coefficient of the acceptor at λ , which is typically in units of $\text{l mol}^{-1}\text{cm}^{-1}$. The term κ^2 is a factor describing the relative orientation in space of the transition dipoles of the donor and acceptor, and is usually assumed to be equal to its average value $2/3$, which is appropriate for dynamic random averaging of the donor and acceptor. This expression allows the Förster distance to be calculated from the spectral properties of the donor and

the acceptor and the donor quantum yield. The integral term in Eq. 2.23 expresses the degree of spectral overlap between the donor emission and the acceptor absorption. The rate of energy transfer $k_T(r)$ is given by ([5])

$$k_T(r) = \frac{1}{\tau_D} \left(\frac{R_0}{r} \right)^6 \quad (2.24)$$

where r is the distance between the donor (D) and acceptor (A) and τ_D is the lifetime of the donor in the absence of energy transfer. The efficiency of energy transfer for a single donor-acceptor pair at a fixed distance is

$$E = \frac{R_0^6}{R_0^6 + r^6} \quad (2.25)$$

Hence the extent of transfer depends on distance r . Fortunately, the Förster distances are comparable in size to biological macromolecules: 30 to 60 Å. For this reason, energy transfer provides an opportunity to measure the distances between sites on macromolecules. According to Eq. 2.25, the distance between a donor and acceptor can be calculated from the transfer efficiency.

2.4.6 Effects of Chemical Environment on Emission Spectra

Emission spectra are dependent upon the chemical structure of the fluorophore and the solvent in which it is dissolved (**solvatochromism**). This is caused by the different interactions between the fluorophore and the solvent itself, which change the energy of the ground and of the excited states of the molecules. In particular, in case of a polar solvent, its molecules orient themselves in order to reduce the ground state energy of the system. Since the charge distribution in the excited state is usually different than in the ground state, this orientation won't be the one with minimal energy for the excited state. However, rotational motions of small molecules in fluid solution are rapid, typically occurring on a timescale of 40 ps or less. The relatively long timescale of fluorescence allows ample time for the solvent molecules to reorient around the excited-state dipole, which lowers its energy and shifts the emission to longer wavelengths. This process is called **solvent relaxation** and occurs within 10^{-10} s in fluid solution. These increased differences between absorption and emission can also produce more substantial Stokes shifts.

2.5 Lifetimes and Quantum Yields

All of the nonradiative processes just described (internal conversion, intersystem crossing and quenching of various types) compete with fluorescence in depopulating the excited singlet state. This is the reason why the latter decays faster than expected by its radiative lifetime. If $S_b(t)$ is the population of the excited singlet state b , k_F the intrinsic fluorescence rate constant and k_{IC} , k_{ISC} and k_Q those that characterize the above mentioned

processes, then we can write

$$-d(S_b)/dt = [k_F + k_{IC} + k_{ISC} + k_Q]S_b \quad (2.26)$$

with solution

$$S_b(t) = S_b(0)e^{-t/\tau_F} \quad (2.27)$$

where $S_b(0)$ is the concentration at time zero and τ_F is the observed fluorescence decay time:

$$\tau_F = [k_F + k_{IC} + k_{ISC} + k_Q]^{-1} \quad (2.28)$$

Defining the fluorescence **Quantum Yield** ϕ_F as the number of emitted photons divided by the number of absorbed photons, this is equal to the ratio between the rate of radiative emission and of excited state depopulation, therefore:

$$\phi_F = \frac{k_F}{k_F + k_{IC} + k_{ISC} + k_Q} \quad (2.29)$$

Combining this expression with the definitions of τ_F and τ_R , we find

$$\phi_F = \tau_F/\tau_R \quad (2.30)$$

If τ_R is known, from a measurement of the fluorescence decay rate τ_F it is possible to determine the quantum yield ϕ_F . More details on the techniques used to measure fluorescence decays, and on more complicated types of measured decay curves, will be given in Subsection 2.6.4, together with the description of the set-up for fluorescence lifetime imaging (FLIM), used during this thesis work to measure fluorescence decay curves.

2.5.1 Brightness

The extinction coefficient tells us how much of the incident light will be absorbed by a given dye, and reflects the wavelength-dependent absorption characteristics indicated by the excitation spectrum of the fluorophore. Emission is increased with higher incident light absorption, meaning that fluorochromes with greater extinction coefficients tend to emit more intensely, and require less energy to adequately excite them. The quantum yield, which is a measure of fluorescence emitted per light energy absorbed, determines how much of this absorbed light energy will be converted to fluorescence. The product of these factors is defined as the **brightness** B of a molecule:

$$B = \phi_F \times \varepsilon \quad (2.31)$$

Suppose that we have a sample which emits a certain fluorescence intensity and we measure an average number of emitted photons N_{counts} for a given configuration of light excitation and detection; the brightness will be proportional to the ratio of the counts

recorded and the sample's concentration c according to:

$$B = \alpha N_{\text{counts}}/c \quad (2.32)$$

with α multiplicative factor that accounts for instrumental geometry and efficiency. I will make use of Eqs. 2.31 and 2.32 further in this thesis, in Chapter 3, Section 3.7.4.

2.6 Fluorescence Microscopy

There has been a rapid growth in the use of microscopy due to advances in several technologies, including probe chemistry (new types of molecular probes have been developed), confocal setups, detectors and computers. Most of the progresses reached during the last years in the field of microscopy stemmed from the purpose of increasing the contrast between the signal and the background in a measurement. In order to reach this goal, fluorescence microscopy is undoubtedly the most powerful technique, and this is one of the reasons why it has become a so widely used tool in the biological sciences. In a typical application of fluorescence microscopy, the chosen target is marked with a fluorescent probe (i.e. a fluorescent proteins or an organic dye); then, the marked target is internalized in the sample, for example cells, and the fluorescence emission is excited by means of a properly filtered source, observed with an optical microscope and collected by a detector (e.g. a CCD for wide-field microscopy), as illustrated in Fig. 2.5. The resolution of this

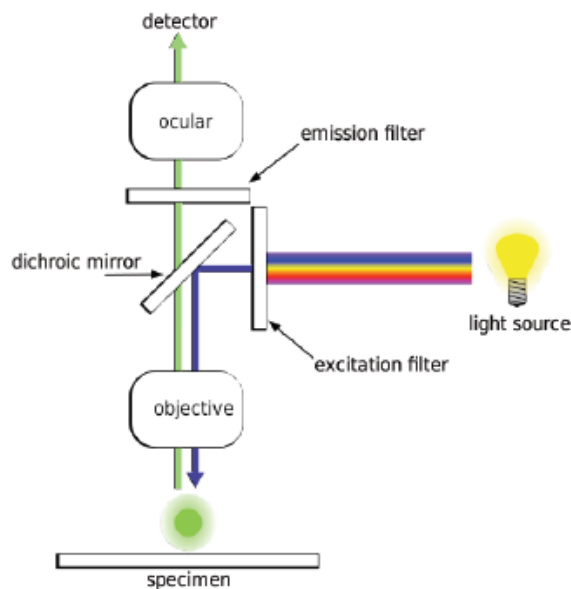


Figure 2.5: Typical experimental setup for an epifluorescence microscopy measurement. In epifluorescence, the sample is observed on the same side of illumination, therefore a dichroic is needed; this is a beam splitter that reflects excitation light and transmits emitted light.

type of microscopy is the same as that of common optical microscopy, but there is a gain with respect to the latter thanks to two factors:

1. the targeted markers localize only in specific cellular compartments, which are distinguishable from the others because they are colored (enhanced contrast);
2. it is possible to mark different targets with different colors and then overlap the images in order to infer information from their colocalization (multichannel microscopy).

Some applications of fluorescence microscopy suffer from the lack of knowledge of local probe concentrations within the sample. This led to the development of fluorescence microscopy techniques whose effectiveness is independent of concentration, such as Fluorescence Lifetime Imaging Microscopy (see Subsection 2.6.4 later in this chapter).

2.6.1 Confocal Microscopy

The resolution of a microscope determines the smallest feature that can be resolved, or the smallest distance that can be determined between two features. It depends on the used optics and microscopy configuration, but also on the *signal-to-noise ratio* (*SNR*), which is defined as

$$SNR = \frac{|mean\ signal - background|}{signal\ standard\ deviation} \quad (2.33)$$

where the background and the signal standard deviation values are increased by the effects of all kinds of noise, e.g. shot, thermal, photon scattering etc. A low SNR makes difficult to discriminate two spots very close to each other. The confocal variant of fluorescence microscopy was introduced to enhance three-dimensional optical resolution; in confocal microscopy, this is achieved by suppressing any signal coming from out-of-focus planes using a pinhole in front of the detector as schematically shown in Fig. 2.6. In a typical confocal setup, a collimated laser beam is reflected by a dichroic mirror and focused by a microscope objective to a small spot in the specimen; the emitted fluorescence is collected by the same microscope objective, transmitted by the dichroic, focused on the mentioned pinhole, eventually filtered and measured by a detector, which can be a photomultiplier tube (PMT), a photodiode or other light sensitive detectors. The effect of blocking out-of-focus fluorescence is called also "*optical sectioning*" because it allows the imaging of separate slices within the sample. Only a single point is imaged at a time, so that to obtain a whole bidimensional section some kind of scanning is required. There are two ways for this: specimen scanning and laser scanning. In the former, the excitation beam is kept stationary while the object is moved, in the latter the sample remains steady and the excitation spot is moved. Laser scanning is usually the most employed method in confocal fluorescence microscopy. The utility of recording many optical sections of the sample is that these can be stacked by the computer to form tomographic images. A comparison between the result of widefield and confocal microscopy is shown in Fig. 2.7.

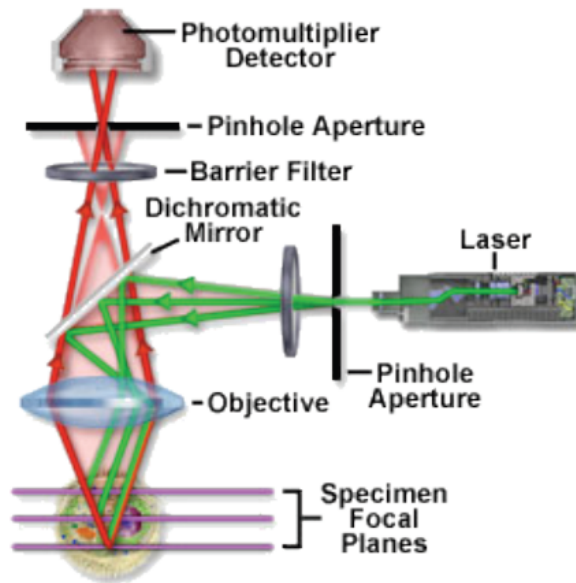


Figure 2.6: Schematic setup of a confocal microscope.

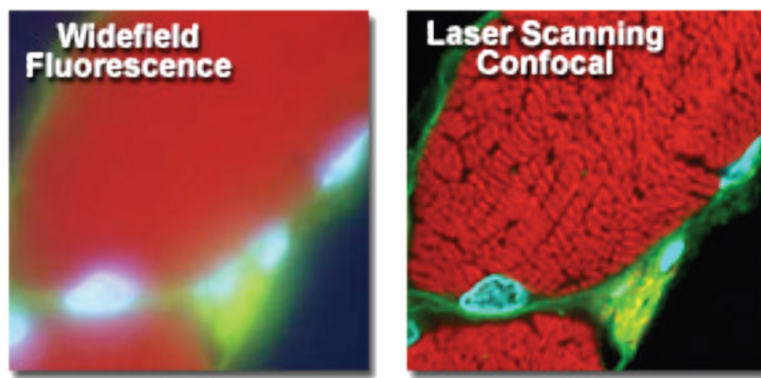


Figure 2.7: Comparison between a snapshot imaged with wide-field microscopy (left panel) and with fluorescence microscopy (right panel): in the latter, the noticeable high contrast enhancement is given by the absence of out-of-focus light.

2.6.2 The Point Spread Function (PSF)

The function of the objective and of the other lens in a microscope is to transform the diverging spherical wavefront radiated by the object to a converging spherical wavefront forming the image. Whereas the former extend over the full 4π radians of a sphere, the second is limited by the size of the lens, given by its aperture. The 3D distribution of light in the image of a point like source is called the **Point Spread Function (PSF)** of the optical system. For an ideal, aberration-free lens, the size of the PSF is determined only by the wavelength of the light and the numerical aperture of the lens ($NA = n \sin \alpha$, with n refractive index of the medium and α semi-aperture angle of focusing); in this case, the imaging is said to be *diffraction-limited*. The PSF can be calculated from diffraction theory; the Full Width Half Maximum of the PSF is said to determine the resolution limit, according to the Rayleigh criterion: two objects are spatially resolvable only if they

are more distant than it. This criterion is also expressed by Eq. 2.34:

$$RES = \frac{1.22\lambda}{2 \cdot N.A.} \quad (2.34)$$

However, in principle it is possible to resolve two points that are closer than the FWHM by deconvolving the output signal with the PSF itself. Since it is nontrivial to calculate the PSF, it is widespread practice to evaluate it by fitting experimental data sets.

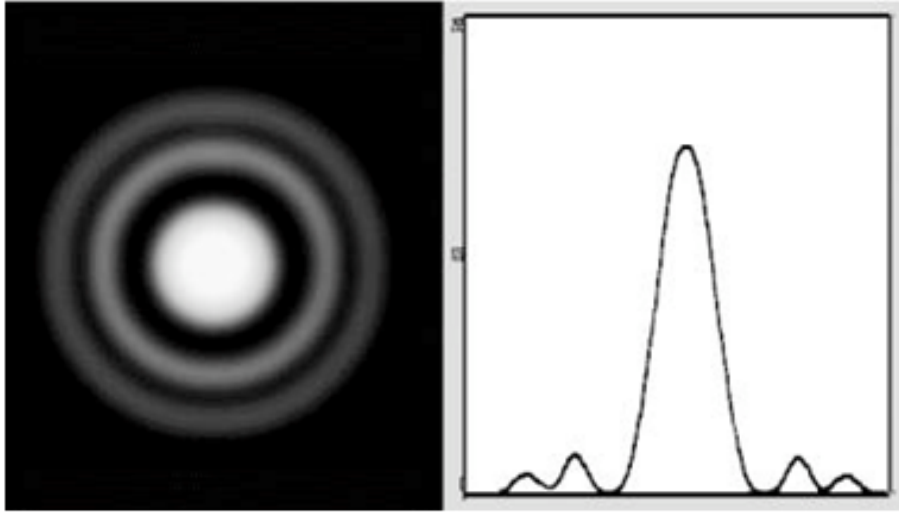


Figure 2.8: Schematic example of Point Spread Function.

2.6.3 Fluorescent Markers

Fluorophores are divided into two general classes, *intrinsic* and *extrinsic*. Intrinsic fluorophores are those that occur naturally. Extrinsic fluorophores are those added to a sample that does not display the desired spectral properties. A class of fluorophores consists of the fluorescent indicators, whose spectral properties are sensitive to a particular substance of interest. Whereas many organic substances present intrinsic fluorescence (autofluorescence), the typical microscopy approach is to employ extrinsic fluorophores. In the following, is reported a short list of the most common fluorescent markers used in fluorescence microscopy.

- **Quantum Dots** (2-10 nm in diameter, $10^2 - 10^5$ atoms): spherical structures made of nanocrystalline layers of semiconductor material (ZnSe, CdS, ecc) whose optical properties are linked to the formation of electron-hole pairs (*excitons*); their emission wavelength are closely related to their linear dimensions. The new generations of quantum dots have far-reaching potential for the study of intracellular processes at the single-molecule level, high-resolution cellular imaging, long-term in vivo observation of cell trafficking, tumor targeting, and diagnostics. The downside of using these objects as fluorescence probes in cellular environment is that, being artificial and made of inorganic elements, they are less biocompatible than other types of

markers listed below.

- **Fluorescent Proteins (FPs, ~ 26 kDa):** intrinsically fluorescent, their name traditionally refers to the Green Fluorescent Protein (GFP) first isolated from the jellyfish *Aequorea victoria*, which has a major excitation peak at a wavelength of 395 nm and a minor one at 475 nm. Its emission peak is at 509 nm and it has a fluorescence quantum yield of 0.79. As fluorescence probes, they have advantages and also disadvantages: on the one hand, they can be genetically "fused" to any other protein to be marked, and, once this is done, it is possible to create cell-lines or transgenic organisms that directly express the GFP labelled protein instead of the normal one, without significantly altering their physiology (Fig. 2.9). Thus, GFPs are very useful for in-vivo observations and, moreover, they are completely biocompatible and bond tightly to the targets. On the other hand, their fluorescence is less photostable and less extended than Quantum Dots one; plus, GFPs fluorescence shows a quite fast *photo-bleaching* (exponential decay of intensity upon protracted illumination).

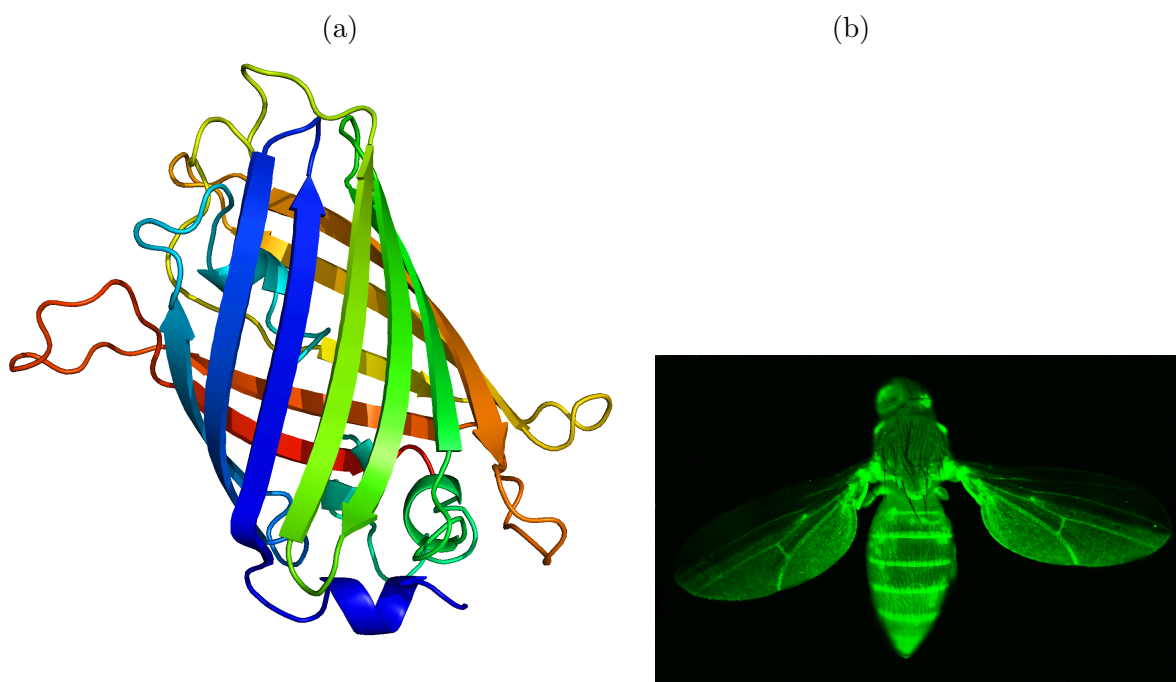


Figure 2.9: Green Fluorescent Protein barrel structure (a) and a bee genetically modified to express the GFP (b).

- **Small organic molecules with delocalized electronic system:** they often have ring structures (aromatic) or single-double bonds sequences, with π bonds which easily distribute outer orbital electrons over a wide area; this kind of molecules are ideal for fluorescence microscopy because the energy differences between the ground and excited states is small enough to allow relatively low-energy photons in the visible part of the electromagnetic spectrum to induce transitions from the first to the other. In general, the more interacting π bonds in the molecule, the smaller the energy gap

and higher the fluorescence quantum yield. An example is the Fluorescein and its derivatives, which are the fluorophores of interest in this thesis work. These molecules are chemically linked to the labelled objects and then are internalized in cells or employed in specific techniques that do not require internalization. I will discuss this type of fluorescent markers more in detail in Chapter 3, Section 3.1.

2.6.4 Fluorescence Lifetime Imaging Microscopy

As already anticipated in 2.5, **time-resolved spectroscopy** is a method of studying biophysical dynamic events investigating transient phenomena in the interaction of light with matter down to subnanosecond times. Time-resolved measurements contain more information than is available from the steady-state data. For instance, consider a sample containing two species, each with a distinct lifetime, but with spectral overlap of absorption and emission; in this case, it is not possible to resolve the emission of the two from steady state data. However, the time-resolved data may reveal two decay times, which can be used to resolve the relative intensities and localization of the two species. Moreover, lifetime measurements allow to distinguish static and dynamic quenching, as anticipated in Subsection 2.4.4. Time-resolved measurements are widely used in fluorescence spectroscopy, particularly for studies of biological macromolecules and increasingly for cellular imaging.

The **Fluorescence-lifetime imaging microscopy (FLIM)** technique was developed in the late 1980s and early 1990s (Bugiel et al. 1989, König 1989), before establishing as a fundamental in the late 1990s. It produces an image based on the difference between fluorescence exponential decays in various regions of the sample. It is a particularly useful technique because it provides measurements that are independent of probe concentration. In fact, the lifetime of a fluorophore is mostly independent of its concentration. Anyway, the fluorescence lifetime depends on environmental factors, such as ionic strength, oxygen concentration, hydrophobicity and interactions between the dyes and other molecules, especially if they result in FRET. In fact, FLIM can be used to measure FRET because the resonant passage of energy from the donor to the acceptor obviously decreases the donor's lifetime. Since it is nontrivial to measure a single lifetime, the concept of lifetime imaging seemed impractical with the technology available in the 1980s and early 1990s. Even if such measurements could be performed, the data acquisition times would be excessively long, precluding studies of living cells. At present, thanks to significant advances in technology, FLIM is establishing in the biosciences as a leading technique.

Measurement Methods for Decay Curves

The two classes of methods for measuring time-resolved fluorescence are time-domain and frequency-domain ones. In the first, the sample is excited with a short pulse of light, preferably much shorter than the decay time τ of the sample. A fluorophore which is excited by a photon will drop to the ground state with a certain probability based on the decay rates through a number of different (radiative and/or nonradiative) decay pathways, as already discussed in the previous sections. To observe fluorescence, one of these pathways must be by spontaneous emission of a photon. In the ensemble description, the fluorescence $F(t)$ emitted will decay with time according to

$$F(t) = F_0 e^{-t/\tau} \quad (2.35)$$

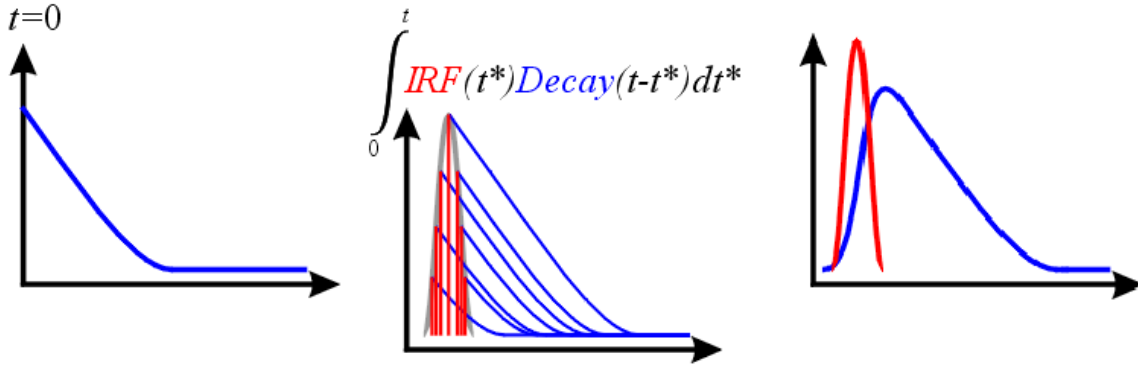


Figure 2.10: Schematic representation of the steps that define an instrument response function.

where $F(0)$ is the initial fluorescence at zero time. The decay time τ is calculated from the slope of a plot of $\log I(t)$ versus t , or from the time at which the intensity decreases to $1/e$ of the intensity at $t = 0$. Unfortunately, the intensity decay law $I(t)$ is what would be observed with δ -function excitation and a δ -function for the instrument response: if the excitation pulse is broad or the detection response is slow, the measured fluorescence $I(t)$ will not be purely exponential. The instrumental response function, $IRF(t)$, will be convolved with the decay function $F(t)$: $I(t) = IRF(t) \otimes F(t)$. The instrument response function (IRF) is the response of the instrument to a zero lifetime sample (i.e. scattering). Its width relates to the shortest time profile that can be measured by the instrument. It should be noticed that the finite width of the excitation pulse is not the only contribute to the IRF: detector response and limited resolution of the instrumental setup must be taken into account too. The instrumental response of the source, detector, and electronics can be measured from scattered excitation light. The IRF can then be convolved with a trial decay function to produce a calculated fluorescence, which can be compared to the measured fluorescence. The parameters for the trial decay function can be varied until the calculated and measured fluorescence curves fit well. This process is known as reconvolution or reiterative convolution, and can be performed quickly by several software packages. In this thesis work, in particular, the Symphotime software by Picoquant has been employed. For a single exponential decay the lifetime is the value of τ that provides the best match between the measured data and the calculated time-dependent intensities. For a multi-exponential decay the analysis yields the values of lifetimes τ_i that are most consistent with the data. The alternative method of measuring the decay time is the frequency-domain or phase-modulation method. In this case the sample is excited with intensity-modulated light, typically with a sine-wave modulation. When a fluorescent sample is excited in this manner the emission is forced to respond at the same modulation frequency. The fluorophore emission results thus delayed in time by a phase shift (φ), and with a reduced modulation with respect to scattered light; both measurements can be used to calculate the decay time.

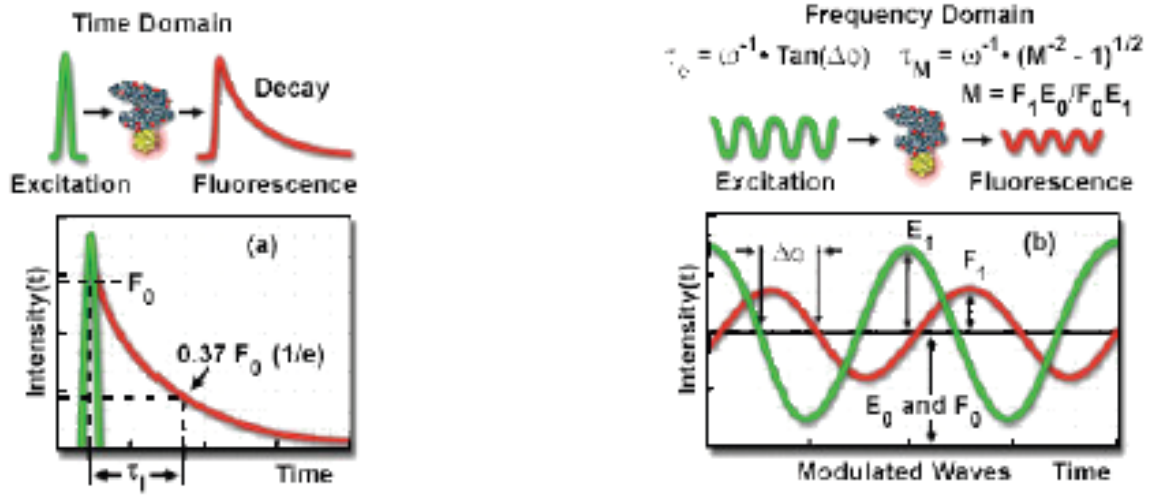


Figure 2.11: Time-domain and frequency-domain lifetime measurements: in the first one (left panel), a pulsed signal impinges on the sample and the decay time is determined straightforward; in the second one (right panel), the exciting source is a modulated signal and the quantities measured are the phase shift and the amplitude variation of the response wave.

Quantum Yields and Decay Curves for a Mixture of Fluorescent Species

In this section, I will show how it is possible to determine the apparent total quantum yield of a mixture of different fluorescent species from the analysis of their fluorescence decay curves, starting from Eq. 2.30, and from rewriting Eq. 2.29 as:

$$\phi_F = \frac{k_F}{k_F + k_{nr}} \quad (2.36)$$

where the term k_{nr} includes all of the non-radiative deactivation possible processes. Eq. 2.36 applies for a sample containing only one species; for a sample displaying two or more species, we can generalize as follows:

$$\phi_{F,i} = \frac{k_{F,i}}{k_{m,i}} = k_{F,i}\tau_i \quad (2.37)$$

with $\phi_{F,i}$ quantum yield, $k_{F,i}$ radiative decay rate, $k_{m,i}$ experimentally measured decay rate and τ_i measured lifetime of the i -th species. Similarly, we can generalize the Lambert-Beer Law (Eq. 2.16) for the case of more than just one absorbing species:

$$A_i = c_i \varepsilon_i(\lambda) l \longrightarrow A = \sum_i c_i \varepsilon_i(\lambda) l \quad (2.38)$$

where l is the optical path length, A_i , c_i and ε_i are the absorbance, the concentration and the molar extinction coefficient of the i -th species, respectively. If N is the number of incident photons and $A \ll 1$, the number of absorbed photons is approximately

$N_{abs} \sim \ln 10 \cdot N l \sum_i c_i \varepsilon_i(\lambda)$. The number of emitted photons is approximately

$$I = \ln 10 N \sum_i c_i \varepsilon_i(\lambda) l \phi_i \quad (2.39)$$

and so we can write

$$\phi_{tot} = \frac{\sum_i c_i \varepsilon_i(\lambda) \phi_i}{\sum_i c_i \varepsilon_i(\lambda)} = \frac{\sum_i c_i \varepsilon_i(\lambda) k_{F,i} \tau_i}{\sum_i c_i \varepsilon_i(\lambda)} \quad (2.40)$$

The number of photons detected per unit of time as an output in a FLIM experiment on a sample with more than one species is

$$N_\gamma = \eta_F \sum_i k_{F,i} c_i \varepsilon_i(\lambda) e^{-t/\tau_i} \quad (2.41)$$

where the term e^{-t/τ_i} represents the exponential decay of the number of molecules in the excited state, and η_F is a factor which accounts also for the instrumental geometry and efficiency in collecting the signal, the way the system is excited.

In a multi-exponential model, the time-dependent intensity is fitted with the following equation:

$$I(t) = \sum_i \alpha_i e^{-t/\tau_i} \quad (2.42)$$

where τ_i are the decay times, α_i represent the amplitudes of the components at $t = 0$. Comparing 2.39 and 2.42, one deduces $\alpha_i \propto k_{F,i} c_i \varepsilon_i$ and

$$\phi_{tot} = \frac{\sum_i \alpha_i \tau_i}{\sum_i \alpha_i / k_{F,i}} \quad (2.43)$$

The most obvious application is to a mixture of fluorophores, each displaying decay time τ_i and fluorescence decay rate $k_{F,i}$. However, sometimes samples that contain only a single fluorophore display decays more complex than a single exponential, *e.g.* because there are different subpopulation of the same chromophore in different local environments (for example, because they are linked to different molecules, or with the same macromolecule in different conformations). For a sample with only one fluorescent species displaying a complex decay, we can assume the same radiative decay rate $k_{F,i} \equiv k_F$, in each environment. In this case, Eq. 2.40 can be rewritten as

$$\phi_{tot} = k_F \frac{\sum_i \alpha_i \tau_i}{\sum_i \alpha_i} \quad (2.44)$$

with k_F is the intrinsic fluorescence rate constant for the type of fluorophore in analysis.

2.6.5 Fluorescence Correlation Spectroscopy

Fluorescence correlation spectroscopy (FCS) measures correlations in the fluctuations of fluorescence intensity in a sub-femtoliter volume; these can be used to detect parameters as diffusion time, number of molecules or dynamics and impact of Inter-System crossing for fluorescently labeled molecules. The technique was independently developed by Watt Webb and Rudolf Rigler during the early 1970s. The breakthrough of the technique was the introduction of confocal optics during the early 1990s by Rigler and co-workers. Indeed, imaging of femtoliter volumes can be obtained with localized multi-photon excitation or using confocal optics. Due to their random motion, molecules will enter and leave the detection volume over time; in response, the measured fluorescence signal (which can be considered proportional to the number of fluorescent molecules in the spot) will fluctuate strongly.

The Effective Volume

The lateral extension (beam waist) w_0 and the axial extension z_0 of the observation volume are schematized in Fig. 2.6.5. The ratio z_0/w_0 is the eccentricity or structure parameter κ . V_{eff} is defined in terms of these dimensions in the following way [21]:

$$V_{eff} = \pi^{3/2} w_0^2 z_0 \quad (2.45)$$

Both diffusion time and number of molecules depend on the size of the observation volume V_{eff} ; this size is determined with the calibration of the system with a known dye with known D and concentration. We should note that V_{eff} is larger than the confocal volume typically referred to in the literature by a factor of $2^{(3/2)} \sim 2.8$. The geometry of excitation and detection light in the confocal spot roughly follows a three-dimensional normal distribution. By approximating it with a Gaussian function, one can find an analytical model for the FCS autocorrelation function. Since effective volume is obtained by curve fitting of the autocorrelation function, the quality of the results depends very strongly on how well the model describes the reality. Misalignment of the system or aberration

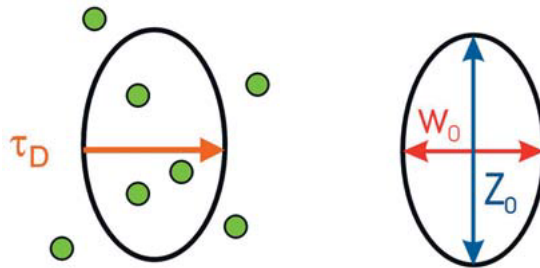


Figure 2.12: Scheme of observation volume and extensions of it: to be more precise, z_0 is effective focal radius along the optical axis at $1/e^2$ intensity and w_0 is the effective lateral focus radius at $1/e^2$ intensity. The diffusion time τ_D indicates the time molecules (green points) spend within the observation volume, i.e. how long it takes to diffuse laterally.

reduce the predictivity of the model.

FCS Theory

In FCS, the detected time-varying fluorescence signal is correlated with a time-shifted replica of itself for different values of time shift τ (lag time). The result is the so-called **autocorrelation function** which is calculated as

$$g(\tau) = \langle I(t)I(t + \tau) \rangle \quad (2.46)$$

where $I(t)$ is the fluorescence signal at time t , $I(t + \tau)$ is the time-shifted one and the triangular brackets indicate averaging over all times t . For $\tau = 0$ we have $g(0) = \langle I^2(t) \rangle$ and for infinite lag time $g(\infty) = \langle I(t) \rangle^2$, the square of the mean fluorescence signal, if there are no long-time correlations. Therefore, the amplitude of the autocorrelation function equals the variance of the signal distribution:

$$g(0) - g(\infty) = \langle I^2(t) \rangle - \langle I(t) \rangle^2 = \sigma^2 \quad (2.47)$$

Generally, the probability to have N particles entering and leaving the volume randomly is distributed according to a Poissonian, for which mean and variance coincide. The function one traditionally deals with in FCS is:

$$G(\tau) = \frac{g(\tau)}{g(\infty)} - 1 \quad (2.48)$$

This function has zero offset and amplitude at $\tau = 0$ proportional to N^{-1} . FCS is highly sensitive only if few fluorophores are observed at any time. In fact, less fluorophores result in more fluctuations, and more fluorophores result in smaller fluctuations and a more constant average signal. The intensity increases and decreases more rapidly if the fluorophores diffuse rapidly. In the case that fluctuation is given only by diffusion of n fluorescent species i , its rate depends on the rate of fluorophore diffusion according to the following equations:

$$G(\tau) = \sum_{i=1}^n \rho_i \left(1 + \frac{\tau}{\tau_i}\right)^{-1} \left(1 + \frac{\tau}{\tau_i \kappa^2}\right)^{-1/2}$$

$$\kappa = \frac{z_0}{w_0} ; V_{Eff} = \pi^{3/2} w_0^2 z_0 ; \langle C \rangle = \frac{\langle N \rangle}{V_{Eff} N_A} ; D_i = \frac{w_0^2}{4 \tau_i} ; \sum_{i=1}^n \rho_i = \frac{1}{\langle N \rangle}$$

where the very last expression is strictly valid only if all the diffusing fluorescent species have the same brightness. Parameters and their physical meaning are summarized in Table 2.1. $\langle C \rangle$ (nM) is the average concentration of molecules in the focal volume and $\langle N \rangle$ denotes the average number of molecules within the detection volume; ideal values of $\langle N \rangle$ for FCS measurements would be 0.3 – 1.5: lower or higher numbers would still do, but the first ones would require longer measurement durations and present a bigger impact of background, while the second ones would cause a decrease in the autocorrelation function's amplitude.

For autocorrelation experiments, where a single dye is measured in each emission channel, the magnitude of the change in molecular weight of free-probe and bound-probe macromolecule will result in a right ward shift in the correlation decay curve due to an increase in correlation time, as shown in Fig. 2.13 below.

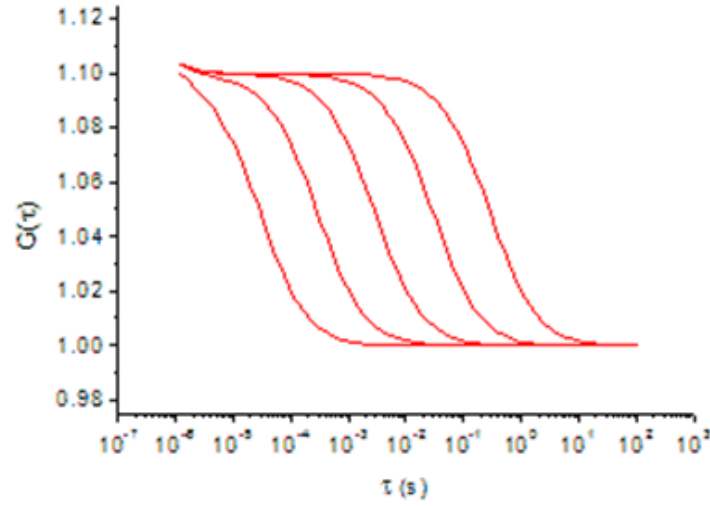


Figure 2.13: FCS curves for free dye (first curve on the left) and some general conjugated systems dye-macromolecule: the change in molecular weight results in a right-ward shift of the correlation decay curves due to an increase in correlation time.

However, in addition to their system of singlet states, fluorophores typically have a set of parallel states (excluding the ground state) referred to as triplet states. To go from a singlet to a triplet state is a so-called forbidden transition and therefore occurs with a small rate constant. These transitions represent a crossing between the system of singlet and the system of triplet states. The fluorescence effectively blinks off as molecules move into the triplet states and back on when they move into the singlet states; this process has

Parameter	Name	Meaning
ρ_i	Current amplitude	$G(0)$
τ_i	Diffusion Time	Time molecules spend inside V_{eff}
D_i	Diffusion Coefficient	Diffusion constant of the i-th diffusing species
κ	Structure Parameter	Excentricity of V_{eff}

Table 2.1: Parameters of the Pure Diffusion Model for fitting FCS autocorrelation curves.

Parameter	Name	Meaning
τ_T	Triplet Time	Typical time for fluctuations between bright and dark states
T	Triplet Fraction	Fraction of molecules in dark state

Table 2.2: Distinctive parameters of the Triplet State Model for fitting autocorrelation curves.

a characteristic relaxation time. Typically, the typical time τ_T of the fluctuations between the bright and the dark states is of the order of microseconds, which is usually smaller than the dynamics of interest (e.g. τ_i in the following expression) but large enough to be measured. A multiplicative term is added to the autocorrelation function for diffusion to account for the triplet state. We have then the **Triplet State Model**.

$$G(\tau) = \left[1 - T + T e^{\left(-\frac{\tau}{\tau_T} \right)} \right] \sum_{i=1}^n \rho_i \left(1 + \frac{\tau}{\tau_i} \right)^{-1} \left(1 + \frac{\tau}{\tau_i \kappa^2} \right)^{-1/2}$$

$$\kappa = \frac{z_0}{w_0} ; V_{Eff} = \pi \frac{3}{2} w_0^2 z_0 ; \langle C \rangle = \frac{\langle N \rangle}{V_{Eff} N_A} ; D_i = \frac{w_0^2}{4 \tau_i} ; \sum_{i=1}^n \rho_i = \frac{1}{\langle N \rangle (1 - T)}$$

The name and physical meaning of some parameters were already included in Table 2.1; parameters distinctive of this model and their physical meaning are summarized in Table 2.2. Note that τ_T depends on the type of fluorophore observed. The just described model will be employed in the following to perform the fits of the samples autocorrelation functions.

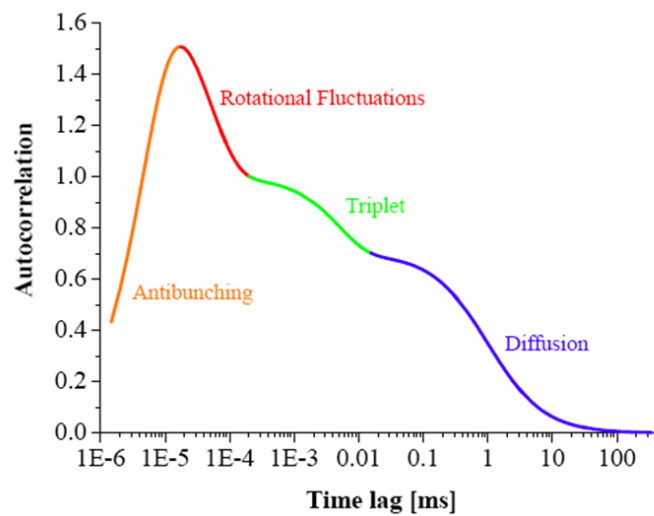


Figure 2.14: Schematization of various contributions to the fluorescence correlation curves: diffusion, triplet-state, rotational fluctuations and photon antibunching.

Optics of FCS

FCS is a spectroscopic method which usually makes advantage of a confocal epifluorescence microscope with high numerical aperture lens, which focuses the beam into a femtoliter sized spot in the sample solution (Fig. 2.15). The collimated laser beam is coupled to the objective via a dichroic mirror, which is reflective at the excitation wavelength and transmissive at the fluorescence emission ones. The confocal aperture rejects emitted light coming from outside the focal plane. The signal is then collected by a sensitive and fast light detector, usually a single-photon avalanche diode (SPAD); the ideal configuration conditions would yield an effective volume V_{eff} of approximately $0.5\mu\text{m}$ in diameter in the focal plane and a few μm along the optical axis.

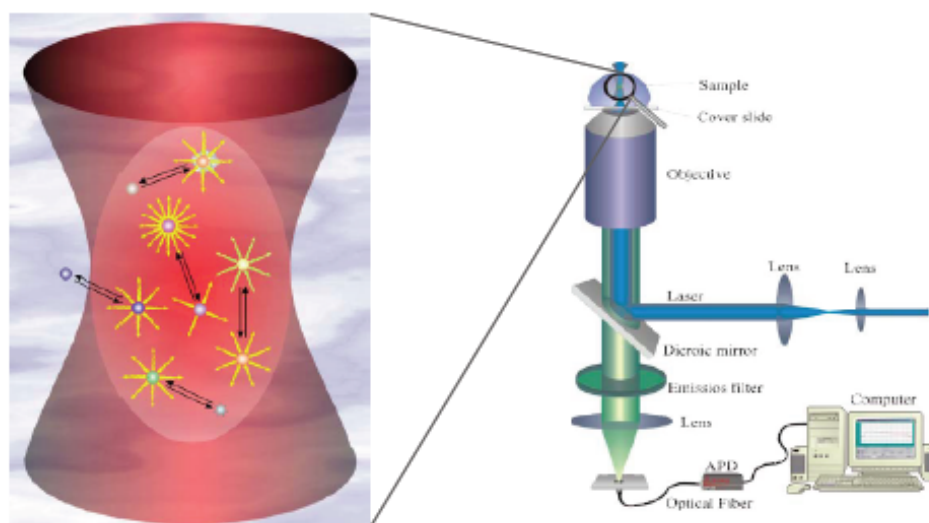


Figure 2.15: Observation volume and molecules entering and leaving it (left side). The temporal correlation function of the fluorescence signal is recorded by means of a confocal microscope, and is possible to obtain maps of fluorescence correlation for the sample.

2.6.6 Single Molecule Detection

Single-molecule detection (SMD) is every day more widespread in the field of Biophysics. Observations on single molecules represent the highest obtainable sensitivity. At the beginning, most single-molecule experiments were performed on immobilized fluorophores, with fluorophores chosen for their high quantum yields and photostability. However, SMD can be extended to intracellular molecules if they are not diffusing too rapidly. In Fig. 2.16 are reported two typical kinds of single-molecule fluorescence intensity traces.

Common bioscience experiments observe a large number of molecules, revealing the ensemble average of the measured properties. When observing a single molecule there is no ensemble averaging, allowing e.g. to distinguish between homogeneous and inhomogeneous broadening in a distribution of parameters. The single-molecule experiments can also reveal the rate of the conformational changes, and this is why it is one of the

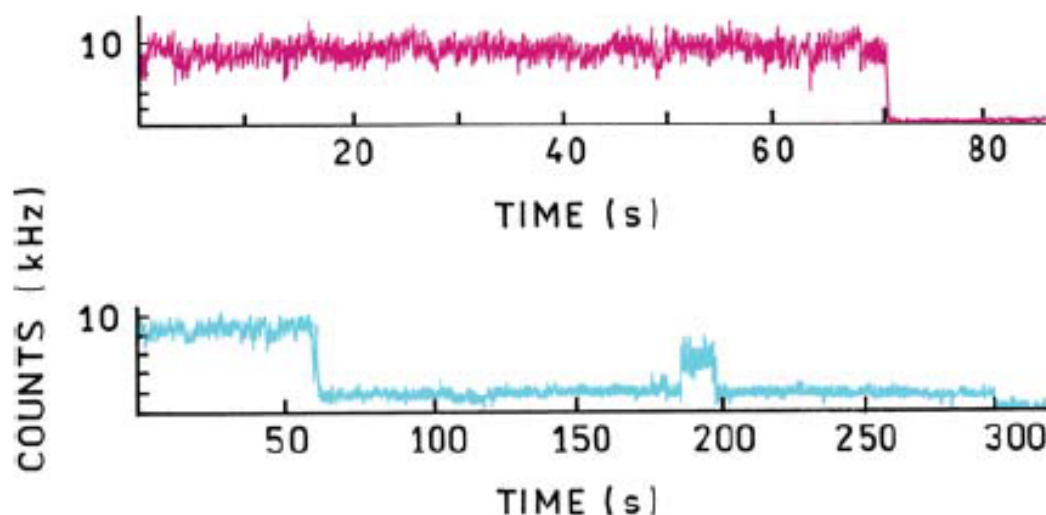


Figure 2.16: Example of fluorescence intensity traces as a function of acquisition time (s) for a typical single-molecule behaviour: top panel shows a single step, which is typical of a molecule which photobleaches after a certain acquisition time; the middle panel is the most typical *blinking* profile: a relatively constant intensity, followed by a rapid drop in intensity, followed by a return of the intensity.

exploited techniques in my thesis work. Such detailed information is not easily extracted from ensemble measurements. Single-molecule experiments are much more prone to the effects of background, therefore they require special care in cleaning the sample and the "sample holder" (see Chapter 3, Section 3.6 for more details inherent to this thesis work), and in collecting the light only from small volumes. A technique useful to reduce the observed volume and so minimize the impact of background is illustrated in the following section.

Total Internal Reflection (TIRF)

A variant of the common fluorescence microscope has been developed in order to reduce the region of signal's provenience, to decrease the background and improve resolution: a **total internal reflection** fluorescence microscope (Fig. 2.17). A particular geometry and opportune refractive indexes mediums ensure that the incident and emitted light beams follow a total reflection path: TIRF Microscopy uses the evanescent wave so created in the sample in order to selectively illuminate and excite fluorophores in a restricted region of the specimen immediately adjacent to the glass-water interface. The evanescent wave is generated only when the incident light is totally internally reflected at the glass-water interface. The evanescent electromagnetic field decays exponentially from the interface, and thus penetrates to a depth of only approximately 100 nm into the sample medium. Recently, TIRF has established as an important tool for biophysics and quantitative biology single-molecule experiments, becoming increasingly used to observe the fluorescence emitted by a single molecule (see also Chapter 3, Section 3.6).

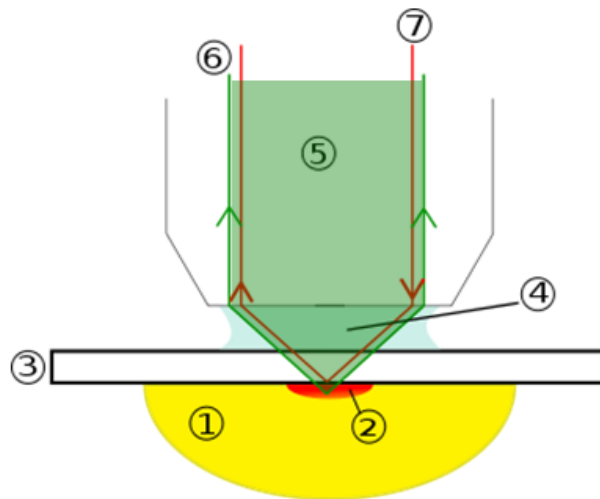


Figure 2.17: Scheme showing the concept of total internal reflection and an example of implementation: (1) sample; (2) limited spot from which the signal is collected; (3) cover glass; (4) Immersion liquid; (5) objective; (6) emitted fluorescence; (7) incident laser radiation.

Chapter 3

Materials, Methods and Experimental Results

3.1 Fluorescein and derivative dyes

The amine-reactive fluorescein derivatives have been among the most common fluorescent derivatization reagents for covalently labeling. In addition to its relatively high absorptivity, excellent fluorescence quantum yield and good water solubility, fluorescein has an excitation maximum (494 nm) that closely matches the 488 nm spectral line of the argon-ion laser, making it an important fluorophore for confocal laser-scanning microscopy. Even though fluorescein has been used to derivatize biomolecules for decades, fluorescein-based dyes and their conjugates have several significant drawbacks, including:

- a relatively high rate of photobleaching, that is the illumination-driven permanent loss for a fluorophore of the ability to fluoresce;
- pH-sensitive fluorescence ($pK_a \sim 6.4$) that is significantly reduced below pH 7 (see Section 3.3);
- a tendency toward quenching of their fluorescence on conjugation to biopolymers, particularly at high degrees of labeling.

An important class of photobleaching events involve the interaction of the fluorophore with a combination of light and oxygen. Reactions between fluorophores and molecular oxygen permanently destroy fluorescence and yield free radical species that can chemically modify other molecules in living cells. Photobleaching can be reduced by limiting the exposure time of fluorophores to illumination or by lowering the excitation energy. However, these techniques also reduce the measurable fluorescence signal. In many cases, solutions of fluorophores or fixed cells can be deoxygenated, but this is not feasible for living cells and tissues.

The photobleaching and pH sensitivity of fluorescein make quantitative measurements with this fluorophore problematic. Furthermore, fluorescein's relatively high photobleaching rate limits the sensitivity that can be obtained, a significant disadvantage for applica-

tions requiring ultrasensitive detection, such as single-molecule detection. These limitations have encouraged the development of alternative fluorophores much more photostable than fluorescein and with less or no pH sensitivity in the physiological pH range (e.g. Alexa Fluor 488, BODIPY FL, Oregon Green 488 etc). When compared with fluorescein, all of these dyes exhibit the same or slightly longer-wavelength spectra (absorption maxima $\sim 490 - 515$ nm) and comparably high fluorescence quantum yields. However, in this work, our goal is to study how the physical-chemical properties of dendrimer-dye(s) systems may vary with respect to the dye(s) alone by tuning relevant parameters that may affect the photophysics, diffusion and the general behavior of dendrimers: in particular, we decided to employ a Fluorescein derivative dye because one of possible outcome of the work would be an optimized pH biosensor, and therefore pH sensibility is requested. We preferred using amine-reactive succinimidyl esters of carboxyfluorescein (commonly called FAM, Fig. 3.1 right scheme) rather than another fluorescein derivative dye available in the laboratory, like Fluoresceine Isothiocyanate (FITC), because the first yields carboxamides more resistant to hydrolysis.

3.2 Materials

G4 Polyamidoamine (PAMAM) dendrimers with Ethylenediamine core, Glycine, Carbonate Buffer pH 9, Triethylamine, 5(6)-Carboxyfluorescein N-hydroxysuccinimide ester BioReagent (NHS-carboxyfluorescein, also known as 5(6)-FAM SE, mixture of isomers, $\geq 90\%$ (HPLC)), Amicon ultra 10 kDa dialysis membranes were purchased from SigmaAldrich. Acetic anhydride was purchased by Carlo Erba Reagents.

N-Hydroxysuccinimide (NHS)-ester labeling reagents, such as NHS-carboxyfluorescein, are among the simplest and most commonly used reagents for labeling. NHS esters react efficiently with primary amino groups ($-\text{NH}_2$) in pH 7-9 buffers to form stable carboxamide bonds. The reaction results in the release of N-hydroxysuccinimide. G4 PAMAM dendrimers have 64 surface primary amines that are available as targets for NHS-ester reagents.

3.2.1 Procedure for Fluorophore Labeling of PAMAM Dendrimers

The G4 PAMAM dendrimer was separately conjugated with different quantities of 5(6)-Carboxyfluorescein N-hydroxysuccinimide ester fluorophores to produce four types of green-labeled, charged PAMAM dendrimers. Conjugation has been carried out via amide bond between the primary amine of the dendrimer and the N-hydroxysuccinimide activated carboxyl of the fluorophores. Dendrimers ($200 \text{ nmol} \leftrightarrow 35 \mu\text{l}$ of PAMAM G4 in solution 10 wt. % in methanol) were dissolved in carbonate buffer at pH 9 and mixed with a DMSO solution of reactive dye until the desired stoichiometric ratio between dendrimer and fluorophore was reached (0.1, 1, 4 and 10 equiv for samples 0.1V+, 1V+, 4V+ and

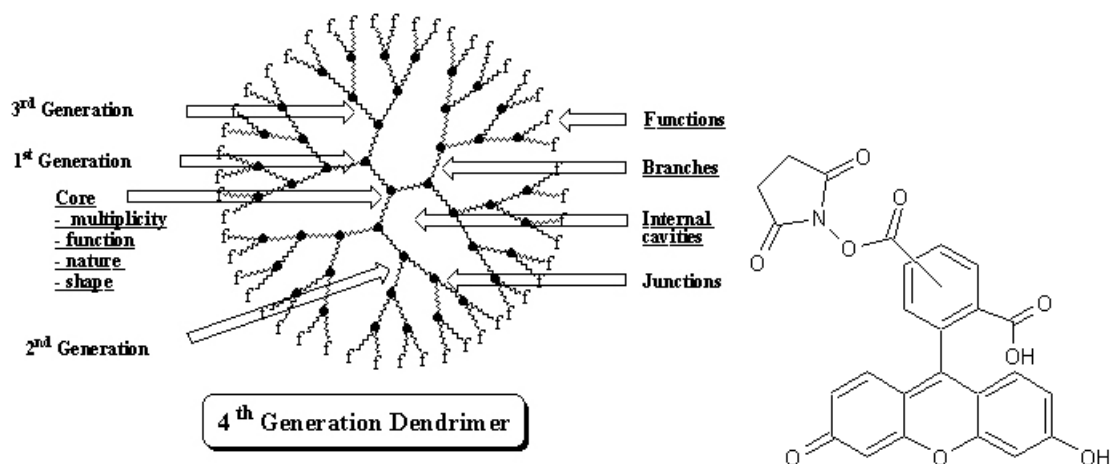


Figure 3.1: G4 PAMAM dendrimer (64 surface primary amines) and 5(6)-Carboxyfluorescein N-hydroxysuccinimide ester fluorophore.

10V+, respectively). The dye was added to the reaction solution in small aliquots (5 or 6 additions overall) to avoid fluorophore aggregation. The solution was stirred overnight at room temperature and then extensively dialyzed against water (Molecular Weight Cutoff MWCO 10 kDa, centrifuge used with speed 3400 rpm and temperature 20°C) to purify the dendrimer-dye conjugates. The solution obtained was then lyophilized in cryovials by means of a Christ Lyophilizer, with the following parameters set: shelf temperature 15°C, vacuum pressure 0.128 mbar and security pressure 5.62 mbar. Typically, after lyophilization, about 1mg of solid product for each sample was obtained and weighted.

A sample of NHS-carboxyfluorescein-Glycine was prepared too, in order to serve as a more reliable comparison to the samples: indeed, NHS-carboxyfluorescein binds to Glycine via amide-bond between the primary amine of the latter and the carboxyl of the fluorophores, which mimics exactly the real linkage between the dendrimer and dyes in the synthesized samples.

When considering the number of fluorophores linked to the dendrimer's surface, we

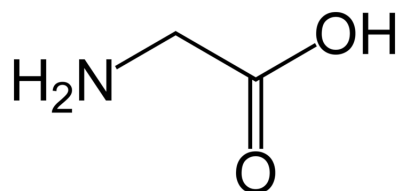


Figure 3.2: Chemical structure of Glycine.

should always keep in mind that they are most probably distributed according to a *Poisson distribution*. In probability theory and statistics, the Poisson distribution is a discrete probability distribution that expresses the probability of a given number of events occurring in a fixed interval of time and/or space if these events occur with a known average rate and independently of the time since the last event. If the expected number of occur-

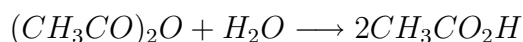
rences in this interval is λ , then the probability that there are exactly k occurrences (k being a non-negative integer, $k = 0, 1, 2, \dots$) is equal to

$$f(k; \lambda) = \frac{\lambda^k}{k!} e^{-\lambda} \quad (3.1)$$

where e is the base of the natural logarithm ($e = 2.71828\dots$). So, for example, the sample supposed to have 4 surface-linked fluorophores may in reality have more or less of them, according to the Poissonian distribution, and this may obviously affect to some extent the photophysical properties of the samples.

3.2.2 General Procedure for PAMAM Dendrimer Acetylation

In order to neutralize the positively charged amines on the surface of G4 PAMAM dendrimers, and so obtain also “neutral” samples to be included in our study, an **acetylation reaction** was carried out. By “neutral” samples we mean samples with neutralized surface amines. Specifically, acetylation refers to the process of introducing an acetyl group into a compound, substituting an active hydrogen atom. In organic chemistry, acetyl is a functional group with chemical formula $-COCH_3$; it is sometimes represented by the symbol *Ac*. Amine acetylation of cationic polymers is attractive since it has been shown to reduce cytotoxicity in a variety of different cell lines. The acetylation reaction occurs by the substitution of an active hydrogen atom due to the attack of acetic anhydride (See Fig. 3.3). However, the acetylation reaction cannot be performed in aqueous solution because, like most acid anhydrides, acetic anhydride hydrolyses to give acetic acid:



This is the reason why acetylation is usually carried out in presence of an excess of triethylamine, which is used as a base to quench eventual acetic acid formed as a side product during the reaction, and to favor the abundance of reactive amines NH_2 over NH_3^+ groups. Triethylamine is a chemical compound with the formula $N(CH_2CH_3)_3$, commonly abbreviated *NEt₃*.

To obtain the acetylated samples, part of the charged samples previously prepared and lyophilized was dissolved in anhydrous methanol (few ml) with triethylamine and acetic anhydride; the solution was stirred overnight at room temperature. An excess of 20 equiv of acetic anhydride and triethylamine were used in the acetylation reaction (quantities of these reagents varied from sample to sample according to the weighed solid, but approximately for all the samples $\sim 10\mu\text{l}$ for both triethylamine and acetic anhydride). The product thus obtained was diluted in deionized water and extensively dialyzed against water (MWCO 10 kDa) to afford the acetylated dendrimer and eliminate all residues of the reagents. Thus, acetylated samples passed through two reactions (the synthesis and the acetylation ones), a two-step dialysis and a two-step lyophilization, in total three more passages than the charged ones. Fig. 3.3 illustrates the acetylation reaction of PAMAM

dendrimer [22].

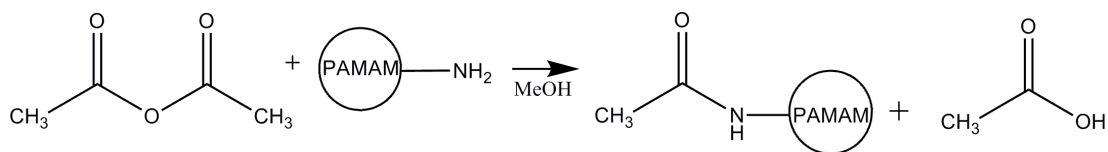


Figure 3.3: Acetylation of PAMAM dendrimers. Acetic anhydride reacts with primary amines of G4 PAMAM dendrimers to produce acetylated PAMAM.

In the following, the samples analyzed will be referred to as 0.1V+, 1V+, 4V+, 10V+, 0.1Vn, 1Vn, 4Vn and 10Vn, where the number stands for the nominal average number of fluorophores linked to the dendrimer's surface, "V" for "verde", which in Italian means "green", and the plus or the 'n' to distinguish if they are charged or neutral.

3.3 UV-Vis Spectrofluorimetry: Methods

Fig. 3.4 and 3.5 illustrate the measurement setup for the two kinds of measurements. Absorption spectra were collected by means of a double beam spectrophotometer Jasco V-550 UV/VIS, equipped with a Peltier temperature controller Jasco ETC-505T; the following experimental parameters were adopted: slits= 5 nm, scanning speed=400 nm/min, data pitch=1 nm. Emission spectra were recorded by means of a Cary Eclipse fluorometer (Varian, Palo Alto, CA) with a built-in Peltier cooler (Varian). Excitation and emission band-pass of 5 nm was employed, scan rate of 60 nm/min and a manually set Photomultiplier voltage of 610 V. In both spectrophotometry and fluorimetry experiments the temperature was set to 25°C. All absorption measurements were carried out according to the following steps: two nominally identical cuvettes were filled with the same amount of solvent and placed the sample and reference chambers of the double-beam spectrophotometer (see Fig. 3.4); after the differential measurement was over, the absorption spectrum of the solvent was saved and set as baseline for subsequent measurements. At this point, a proper quantity of sample was added to the solvent solution contained in the measurement cuvette, in order to obtain the absorption spectrum of the material alone. Two kinds of experiments have been performed with these instruments on the samples: pH titrations and quantum yield measurements. For the first, 1350 μl of Milli-Q water (water purified and deionized to a high degree, registered trademark of Millipore Corporation), 150 μl of Phosphate Buffer Saline (PBS) and an amount of sample solution in the range of 10-100 μl were put in quartz cuvettes (Hellma, Milan, Italy), while for the second, typically 400 μl of PBS/Carbonate Buffer pH 9.1 and sample were put in the cuvettes.

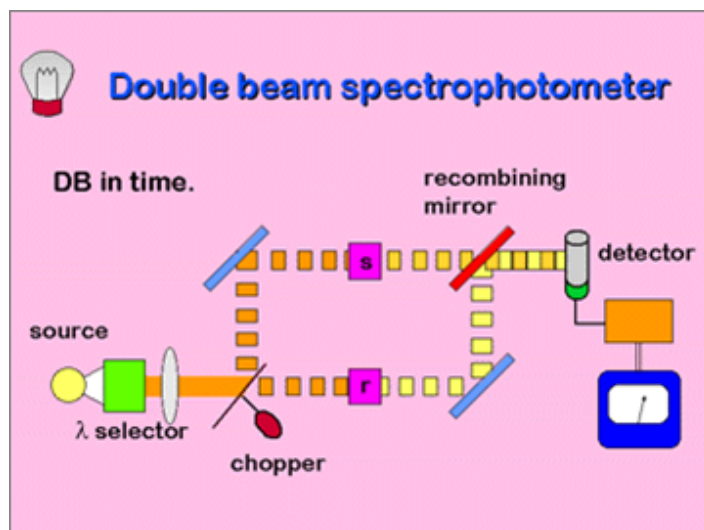


Figure 3.4: Scheme of a double beam spectrophotometer: the radiation emitted by the source is filtered by a variable lambda-selector, *e.g.* a monochromator, and then directed alternatively across sample *s* and reference *r*; the beams are both directed towards a detector, and the resulting signal is then demodulated in order to measure directly the usually small difference between the two light intensities, with a smaller uncertainty than the one given by the difference of the two signals measured directly.

Fluorescence Measurement

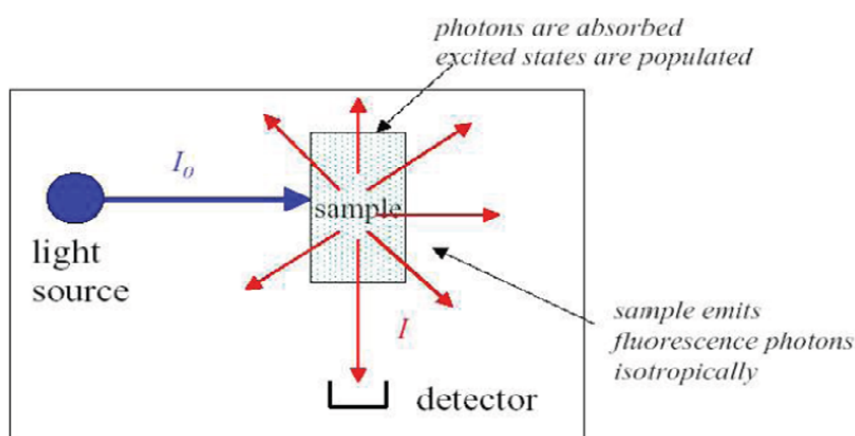


Figure 3.5: A typical fluorescence measurement setup: the light from an excitation source passes through a filter or monochromator, and strikes the sample. A proportion of the incident light is absorbed by the sample, and some of the molecules in the sample fluoresce. The fluorescent light is emitted in all directions. Some of this fluorescent light passes through a second filter or monochromator and reaches a detector, which is usually placed at 90° to the incident light beam to minimize the risk of transmitted or reflected incident light reaching the detector.

3.3.1 Fluorescein Absorption and Emission Spectra

Fluorescein and many of its derivatives exhibit multiple, pH-dependent ionic equilibria. Both the phenol and carboxylic acid functional groups of fluorescein are almost totally ionized in aqueous solutions above pH 9 (Fig. 3.6). Acidification of the fluorescein dian-

ion first protonates the phenol ($pK_a \sim 6.4$) to yield the fluorescein monoanion, then the carboxylic acid ($pK_a < 5$) to produce the neutral species of fluorescein. Further acidification generates a fluorescein cation ($pK_a \sim 2.1$). Only the monoanion and dianion of fluorescein are fluorescent, with quantum yields of 0.37 and 0.93, respectively, although excitation of either the neutral or cationic species is reported to produce emission from an anionic excited state with quantum yields of 0.31 and 0.18, respectively. A further equilibrium involves formation of a colorless, nonfluorescent lactone. The lactone is not formed in aqueous solution above pH 5 but may be the dominant form of neutral fluorescein in solvents such as acetone.

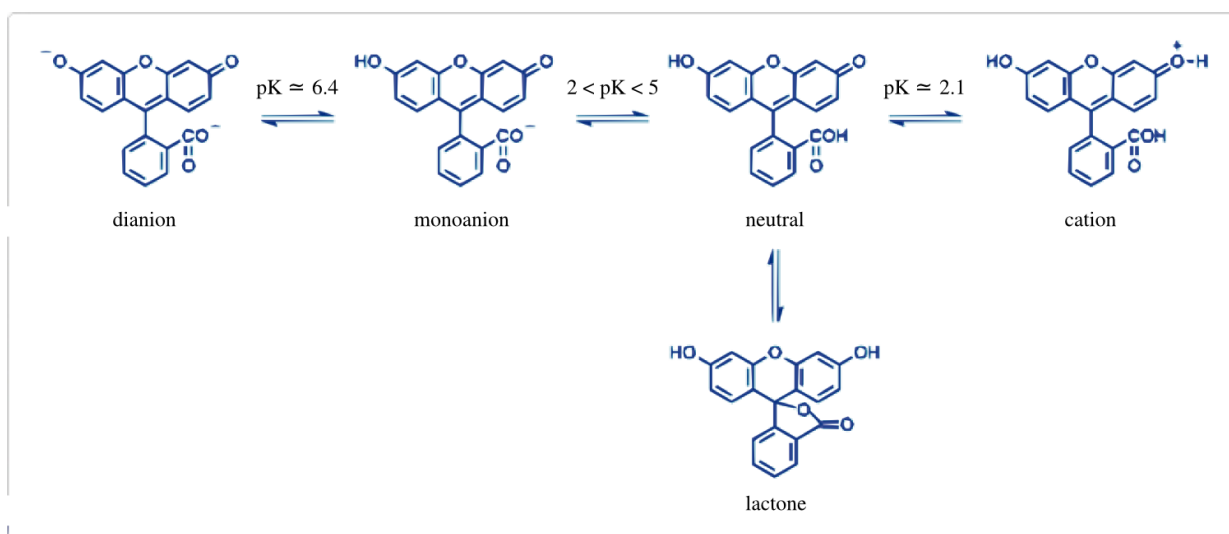


Figure 3.6: Ionization equilibria of Fluoresceine.

The pH-dependent absorption and emission spectra of fluorescein are reported in Fig. 3.7. It is evident the decreased absorptivity at low pH indicative of the formation of protonated species. However, the fluorescence emission spectrum of most fluorescein derivatives, even in acidic solution, is dominated by the dianion, with only small contributions from the monoanion. Consequently, the wavelength and shape of the emission spectra resulting from excitation close to the dianion absorption peak at 490 nm are relatively independent of pH, but the fluorescence intensity is dramatically reduced at acidic pH. As we can see from Fig. 3.7, Fluorescein also presents an **isosbestic point** (equal absorption for all $pH > 5$ values) at 460 nm. Absorption and fluorescence of fluoresceine derivatives, such as 5(6)-FAM SE considered in this work, have the same pH dependency than fluorescein: their molar extinction coefficients and fluorescence quantum yields decrease markedly at $pH < 7$. Indeed, fluorescence is very sensitive and can provide important information on macromolecular structure modifications and particularly on the environment surrounding the probe.

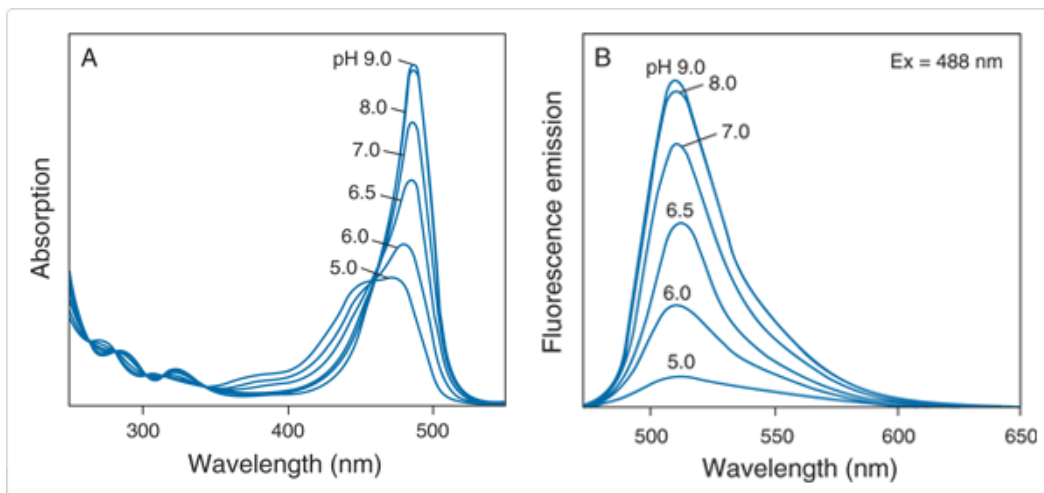


Figure 3.7: Absorption and emission spectra for Fluorescein pH titration from [23].

3.3.2 Titrations and Volume Corrections

A *titration* is the process in which one solution is added to another such that it reacts under conditions in which the added volume may be accurately measured. Titrations are most commonly associated with acid-base reaction, but they may involve other types of reactions as well. I performed pH titrations and also an experiment where aqueous solution of NaOH 0.01M was added to a solution of NHScarboxyfluorescein in Dimethylformamide (DMF).

When performing a titration or similar experiments, the total volume of the solution, and therefore the sample concentration, change. In order to have comparable results, for all the samples, both absorbance A and fluorescence emission I were corrected to account for the change in volume (and, therefore, concentration) in the measurement cuvette as acid or base was added, according to the expressions:

$$A_{corr} = \frac{V_f}{V_i} A_{exp} \quad I_{corr} = \frac{V_f}{V_i} I_{exp} \quad (3.2)$$

where A_{corr} and I_{corr} are the corrected values of absorbance and fluorescence emission, A_{exp} and I_{exp} are the measured absorbance and fluorescence intensity, V_i is the initial volume and V_f is the final volume in cuvette after each acid-base addition.

3.4 UV-Vis Spectrofluorimetry: Results

3.4.1 NHScarboxyfluorescein-Glycine Absorption and Emission Spectra.

pH titrations of the NHScarboxyfluorescein-Glycine compound were performed firsthand and compared to those of Fluorescein reported in Fig. 3.7 above to investigate the absorption and fluorescence emission trends with varying pH. Operatively, to perform pH titrations (see also Subsection 3.4.2), I added separately to the solvent-sample solution in cuvette aliquotes of about 1-5 μ l of acid HCl 0.01M or base NaOH 0.01M, in order to

lower or increase the solution's pH, respectively; I measured the real pH in cuvette after each acid-base addition by means of a calibrated pHmeter and recorded, for each pH, an absorption and an emission spectrum.

From Fig. 3.8 we can see that NHScarboxyfluorescein-Glycine displays a pH-dependent behavior for both absorption and fluorescence emission spectra, with both of them decreasing as the pH becomes more acidic. This is in line with the evidences observed for Fluorescein alone, and expected from what reported in Subsection 3.3.1. Furthermore, NHScarboxyfluorescein-Glycine presents an isosbestic point for pH values > 5 at excitation wavelength of about 460 nm, as the Fluorescein dye (see Fig. 3.7): this evidence indicates that the conjugated system NHScarboxyfluorescein-Glycine behaves exactly like fluorescein in solution. The loss of the isosbestic point at $\text{pH} < 5$ demonstrates the impact of other equilibria, which involve the neutral and/or the cationic species.

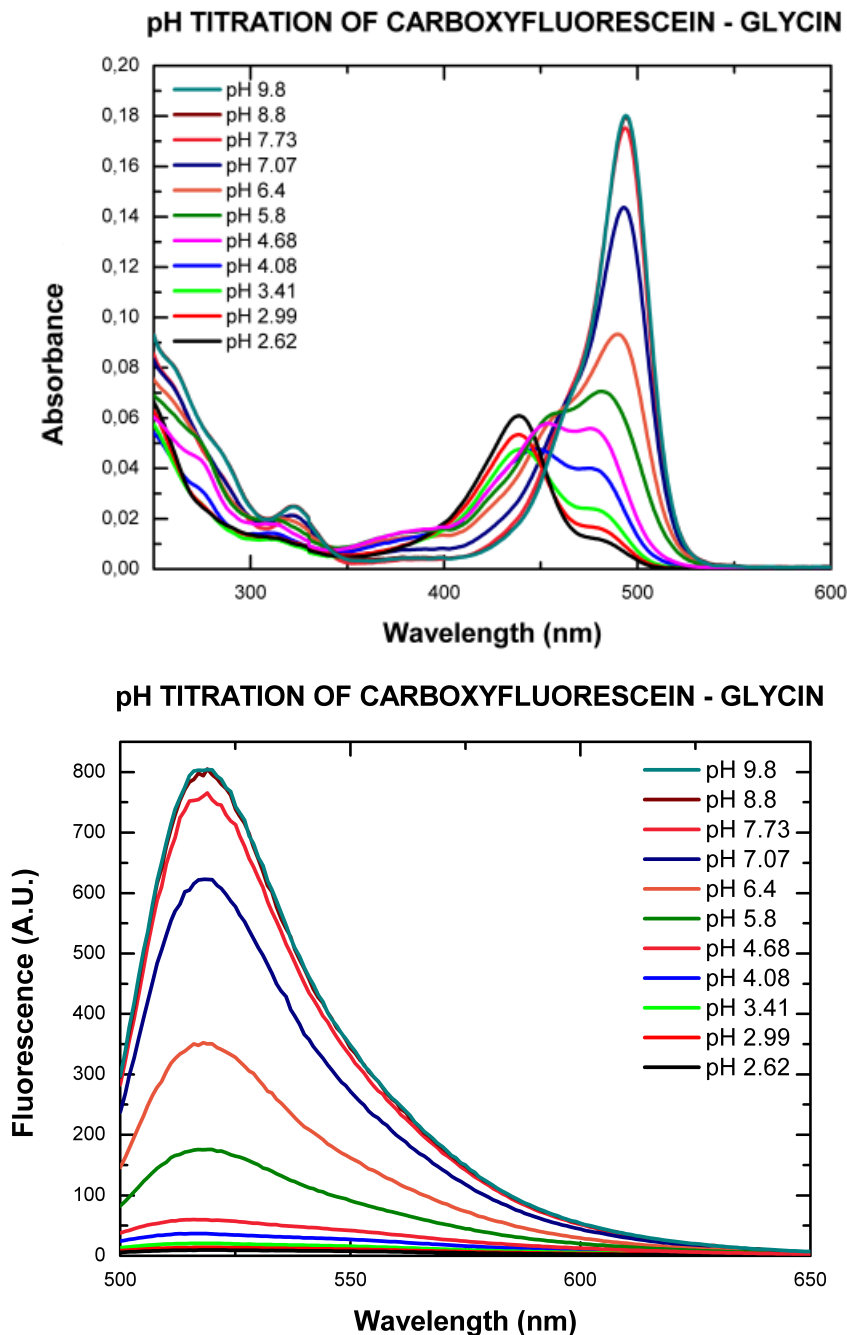


Figure 3.8: pH titration of NHScarboxyfluorescein-Glycine: absorption and emission spectra are reported in different colors at the indicated pH. The sample concentration in cuvette was about $2\mu\text{M}$; the measurements were performed at 25°C , optical path length $l = 1\text{cm}$ and with $\lambda_{exc} = 488\text{nm}$ for the fluorescence experiment.

3.4.2 Samples pH Titrations

In this thesis work, I performed firsthand pH titrations of all the charged samples and two of the neutral ones as well; Fig. 3.9 and 3.10 report the overlay of some of the absorption and emission spectra recorded during the pH titration for the samples 4V+ and 4Vn, respectively, in the pH range from 2.5 to 10.5. Comparing the absorption

spectra of these samples with those of Fluorescein and NHScarboxyfluorescein-Glycine reported in Figs. 3.7 and 3.8, respectively, we note that the samples titrations, both charged and neutral, do not exhibit an isosbestic point, but rather an “isosbestic region” in the range of pH 5-9: this is consistent with the assumption, which we support, that there is not a unique species in solution, but rather many different ones with partially ionized fluorophores contributing to the absorption process. We will discuss this evidence in more detail in Chapter 4. Moreover, there are striking differences between dendrimer-linked NHScarboxyfluorescein and NHScarboxyfluorescein-Glycine in the intensity of the spectra and in the shape of the absorbance ones, especially at $\text{pH} \lesssim 5$, which will be discussed later in this chapter, and in the peak wavelength, which will be discussed in section 3.4.3.

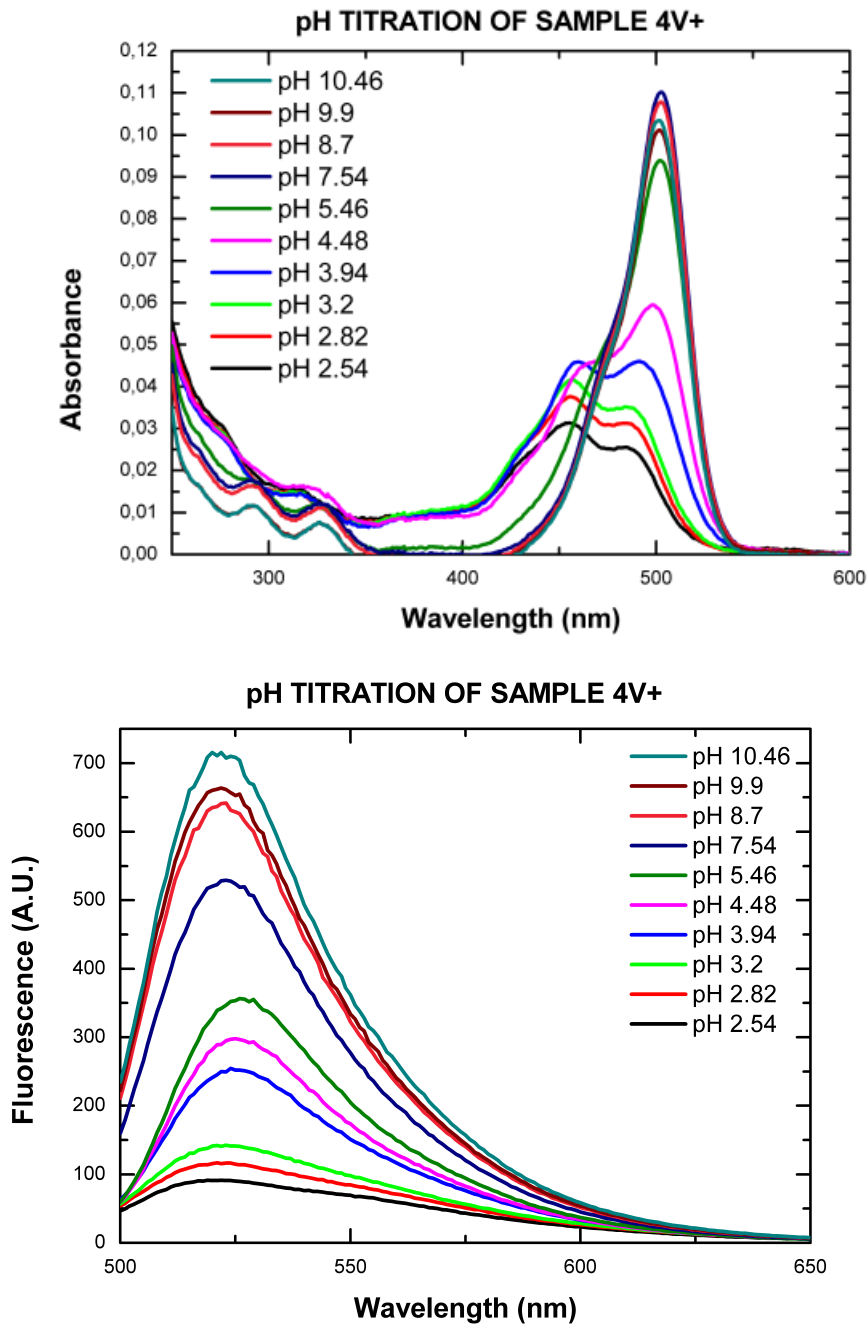


Figure 3.9: pH titration of sample 4V+: absorption and emission spectra are reported in different colors at the indicated pH. The sample concentration in cuvette was about 400nM; the measurements were performed at 25°C, optical path length $l = 1\text{cm}$ and with $\lambda_{exc} = 488\text{nm}$ for the fluorescence experiment.

In order to better appreciate the aforementioned differences, Fig 3.11 reports as an example a comparison between the normalized (values divided by the maximum) fluorescence integrals as a function of pH for NHScarboxyfluorescein-Glycine and sample 1V+: until pH ~ 6 the charged samples show a sigmoidal trend as the one displayed by NHScarboxyfluorescein-Glycine, which is the usual trend found in pH titrations of Fluorescein and derivative dyes; at pH < 5 , differently from NHScarboxyfluorescein-Glycine

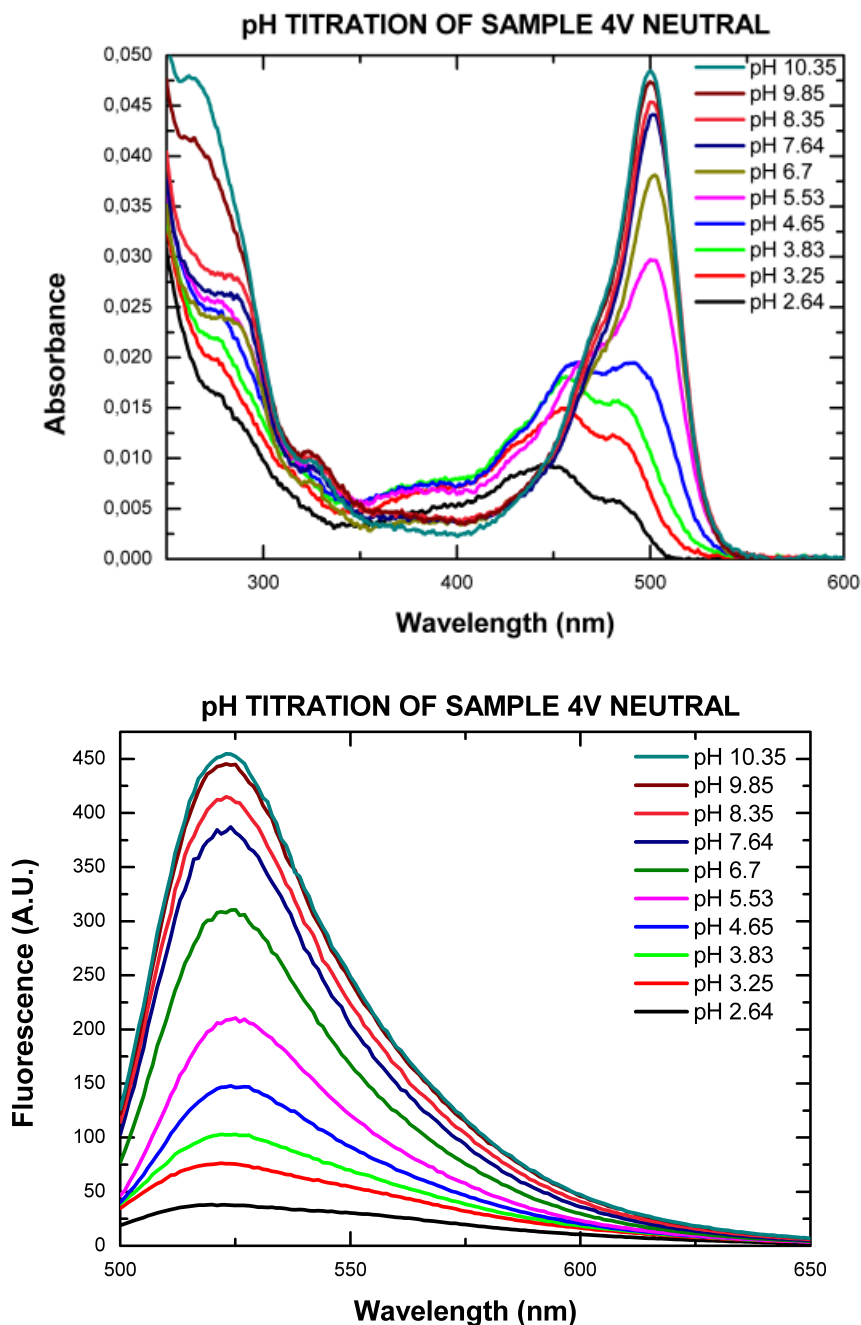


Figure 3.10: pH titration of sample 4Vn: absorption and emission spectra are reported in different colors at the indicated pH. The sample concentration in cuvette was about 130nM; the measurements were performed at 25°C, optical path length $l = 1\text{cm}$ and with $\lambda_{exc} = 488\text{nm}$ for the fluorescence experiment.

titration, the samples emission intensity tends to increase. this can be explained recalling that the G4-PAMAM dendrimer is known to have three protonation levels: at high pH (>9), it is fully deprotonated (uncharged dendrimer), at neutral pH (~ 7) it has all primary (surface) amines protonated, and at low pH (<5) it has all primary and tertiary (internal) amines protonated. Thus, at pH values < 5 , the dendrimer's structure tends to become more open and rigid for the protonation of the tertiary amines; this change in

the conformation of the interior affects also the dendrimer's surface and the eventually linked molecules, allowing for more space between the latter and the charged primary amines of the dendrimer. This causes a relative increase of fluorescence emission, since the interactions between linked fluorophores and dendrimer's surface are reduced, and the dyes recover a behaviour more similar to that of the non-conjugated configuration. The same peculiar behaviour displayed by charged samples is not observed for acetylated samples, which instead show a fluorescence pH titration curve more similar to that of the dye alone, as illustrated in Fig. 3.12; however, the less sharp increase of the fluorescence with pH is still indicative of a more complicated equilibrium between various forms of the dendrimer-dye(s) systems.

In Fig. 3.13 is reported as an example the plot of volume-corrected Absorbance (value

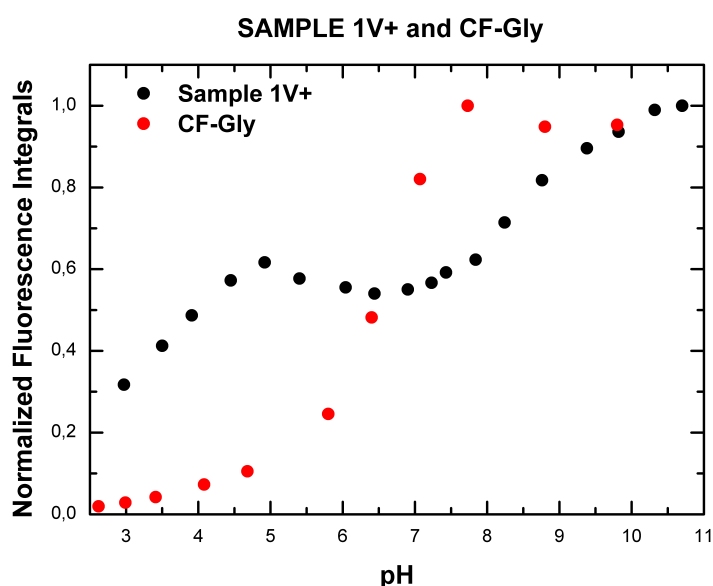


Figure 3.11: Comparison between the normalized fluorescence integrals as a function of pH for NHScarboxyfluorescein-Glycine and sample 1V+.

at $\lambda = 488\text{nm}$) as a function of pH for the sample 1V+: this trend for varying pH was found to be different for the samples and for NHScarboxyfluorescein-Glycine, meaning that the linkage to the dendrimer's surface affects not only the fluorescence emission of bound fluorophores, but also their capability to absorb incident light.

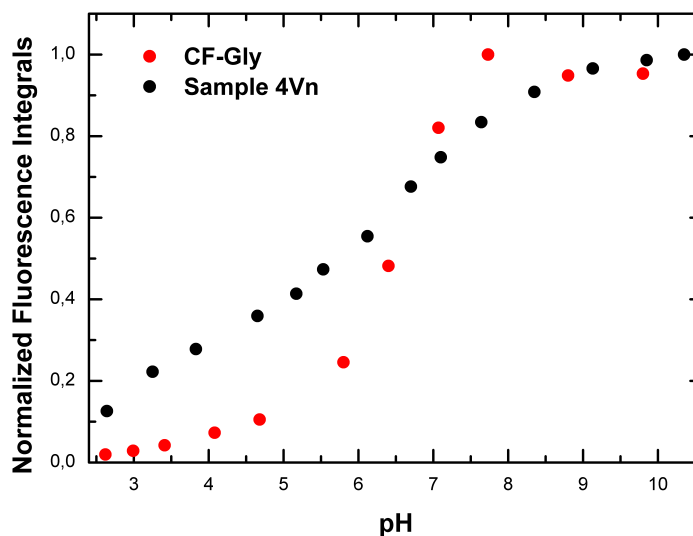


Figure 3.12: Comparison between the normalized fluorescence integrals as a function of pH for NHScarboxyfluorescein-Glycine and sample 10Vn.

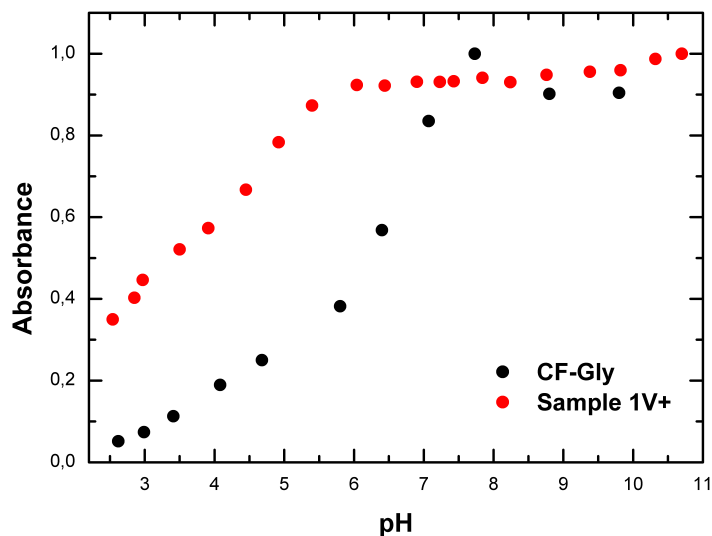


Figure 3.13: Volume-corrected Absorbance at $\lambda = 488\text{nm}$ as a function of pH for the sample 1V+.

3.4.3 Absorption and Emission Peak Wavelength Shift

Comparing the emission and absorption spectra of NHS-carboxyfluorescein and NHScarboxyfluorescein-Glycine with those of the charged and neutral samples, we observed a red-shift of the peak wavelength of the latter with respect to the former two. Table 3.1 below reports the values of absorption and emission peak wavelengths for all the samples considered and for NHS-carboxyfluorescein and NHScarboxyfluorescein-Glycine. While there is no significative difference between those of these last two, we can assert that there is

Sample	Abs Peak λ (nm)	Fluorescence Peak λ (nm)
NHS-CF	495	518
NHS-CFGly	493.5	518
0.1V+	501	524
1V+	502	522
4V+	503	524
10V+	502	522
0.1Vn	503	526
1Vn	500	526
4Vn	503	526
10Vn	501	526

Table 3.1: Values of absorption and emission peak wavelenghts for all the samples considered and for NHS-carboxyfluorescein and NHS-carboxyfluorescein-Glycine: the uncertainties for both columns are considered $\pm 2.5\text{nm}$, that is the half width of the emission slits of the spectrophotometer and of the fluorimeter, according to the parameter set specified in Section 3.3 of this Chapter.

a real shift of about 5 nm between wavelengths of absorption and fluorescence spectra for the samples and that for the dye alone or the dye linked to Glycine (which doesn't alter significantly the photophysics of the fluorophore). This shift is observed both in the charged samples and in the acetylated ones, suggesting that the charge surface should not be addressed as the reason for it. Suspecting a change in the chemical environment polarity as the real cause of this shift, we recorded absorption and emission spectra of NHS-carboxyfluorescein in Dimethylformamide (DMF, molecular formula C_3H_7NO), a polar (hydrophilic) aprotic solvent commonly used in chemical reactions. DMF presents a dielectric constant of 38 and refractive index of 1.43 at 20°C; these values should be compared to those of water, which has dielectric constant of 80 and refractive index of 1.33 at 20°C. Polar aprotic solvents are solvents that present ion dissolving power as protic solvents but lack an acidic hydrogen (H^+). Common characteristics of polar aprotic solvents are no mobile protons and ability to stabilize ions. We performed measurements with the spectrophotometer and the fluorimeter described above, using a solution $2\mu\text{M}$ of NHS-carboxyfluorescein in DMF, for a total of $400\mu\text{l}$ in cuvette. As expected, we found that NHS-carboxyfluorescein absorption and emission were both very low and almost undetectable due to the fact that in DMF the dye loses part of its aromatic conjugation, forming a non-fluorescent species called lactone. We proceeded to subsequent additions of NaOH 0.01M in the cuvette, in particular 1%, 4%, 5%, 10%, 15%, 20% and 50% of the volume ($400\mu\text{l}$), witnessing not only a significant increase in both absorption and fluorescence emission, but also and most importantly, the expected shift towards shorter wavelengths as the amount of NaOH in solution rises. Indeed, the increase in absorption and emission is due to the presence of NaOH as a basis, which favors the deprotonation of the fluorophore's carboxylic group and phenol thus fostering the formation of the dianionic species. Considering that the dielectric properties of DMF are comparable with those of the dendrimer, from these experimental evidences we could confirm our hypoth-

esis that the dendrimer's environment affects the absorption and emission wavelength of the fluorophore, as well as its capability to absorb and emit the incident light.

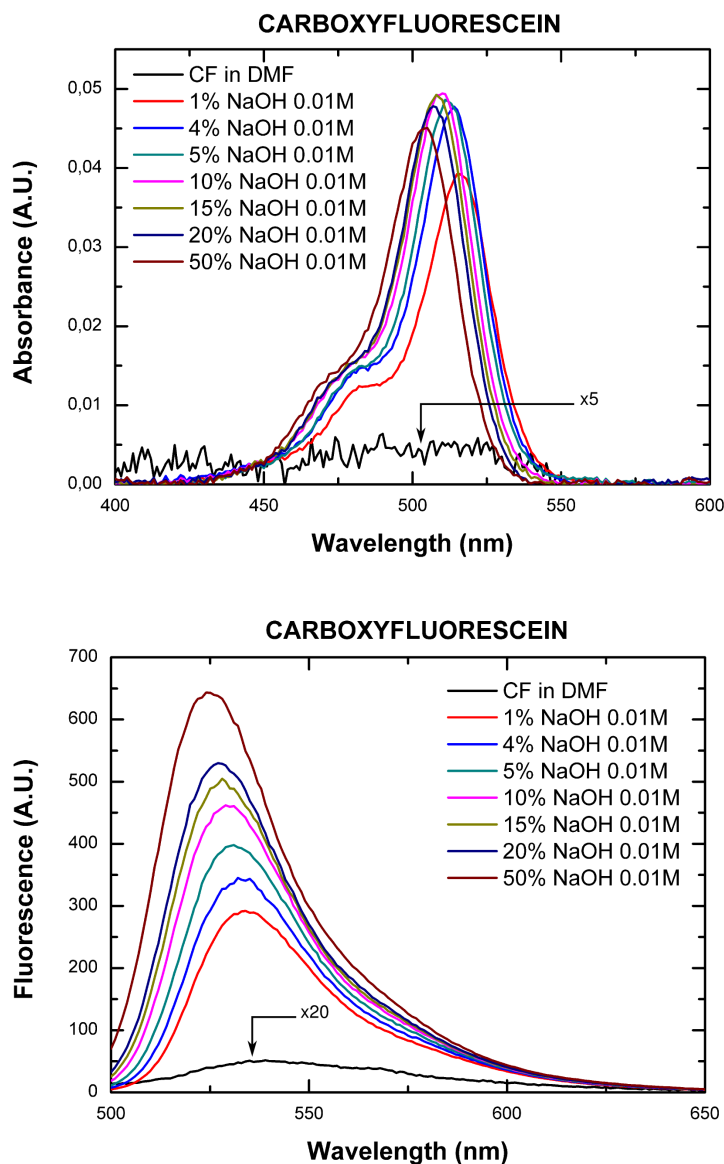


Figure 3.14: Absorption and emission spectra (volume-corrected) for NHScarboxyfluorescein in Dimethylformamide for subsequent additions of NaOH 0.01M in the measurement cuvette: the two plots show the significant rise in both absorption and emission due to increasing pH, and the peak-wavelength shift towards higher energies as the chemical environment in cuvette becomes more polar. The sample concentration in cuvette was about $2\mu\text{M}$; the measurements were performed at 25°C , optical path length $l = 1\text{cm}$ and with $\lambda_{exc} = 488\text{nm}$ for the fluorescence experiment.

3.4.4 Molar Extinction Coefficients

Molar extinction coefficients of the charged samples were experimentally evaluated recording absorption spectra of known concentration solutions in Phosphate Buffer Saline (pH 7.4) and in Carbonate Buffer at pH 9.1 at excitation wavelength 488 nm, according to the **Lambert and Beer Law**:

$$A = \varepsilon lc \quad (3.3)$$

where A is the absorbance recorded, l is the optical path traveled by light through the sample (the lateral dimension of the cuvette, which in our case was 1cm) and c the concentration in cuvette, known a priori. Measurements were all run at 25°C and with the spectrophotometer acquisition parameters specified above. Fig. 3.15 reports the extinction coefficient spectra for all the samples. The values reported in Table 3.2 are those corresponding to light wavelength of 488 nm; ε is expressed in ($\text{l mol}^{-1} \text{cm}^{-1}$).

Sample	$\varepsilon_{488\text{nm},\text{exp}}$ pH 7.4	$\varepsilon_{488\text{nm},\text{th}}$ pH 7.4	$\varepsilon_{488\text{nm},\text{exp}}$ pH 9	$\varepsilon_{488\text{nm},\text{th}}$ pH>9
0.1V+	4300 ± 200	6500	5000 ± 600	7000
1V+	44400 ± 7500	65000	44000 ± 7000	70000
4V+	256000 ± 40000	260000	260000 ± 50000	280000
10V+	510000 ± 170000	650000	409000 ± 130000	700000

Table 3.2: Experimental and theoretical molar extinction coefficients at pH 7.4 and pH 9 for all the charged samples: the errors reported are estimated from measurements carried out on different days.

As we can see by the table, the absolute values of the ε appear a bit lower than the theoretical ones expected considering for the 5(6) Carboxyfluorescein-NHS a molar extinction coefficient of $65000 \text{ l mol}^{-1} \text{cm}^{-1}$ at pH 7.4 (value measured firsthand with the same parameter set as the samples ones) and a molar extinction coefficient of $70000 \text{ l mol}^{-1} \text{cm}^{-1}$ at pH>9 (as found in literature); nevertheless, from Fig. 3.16, we can assert that the values obtained follow a scaling law: in fact, plotting the values obtained for the molar extinction coefficients of the charged samples versus the theoretical number of fluorophores that each is supposed to have and performing a linear fit, we find a slope of about $(52300 \pm 6100) \text{ l mol}^{-1} \text{cm}^{-1}$ for pH 7.4 and a slope of about $(47900 \pm 6100) \text{ l mol}^{-1} \text{cm}^{-1}$ at pH 9, which can be interpreted as an average molar extinction coefficient per NHScarboxyfluorescein molecule for the charged specimens at respective pH. The same scaling trend can be inferred looking at Fig. 3.15: the peaks shown by the samples 0.1V+, 4V+ and 10V+ are, respectively, about 1/10, 4 and 10 times the peak height of 1V+.

For what concerns the ε coefficients of the acetylated samples, the values we found were about ten times lower than expected, mostly because absorbance was dramatically reduced after acetylation, and presented a marked deviation from the trend of the charged samples. We are dubious about this result, since other research works carried out at NEST Laboratory reported that fluorescence emission and molar extinction coefficients

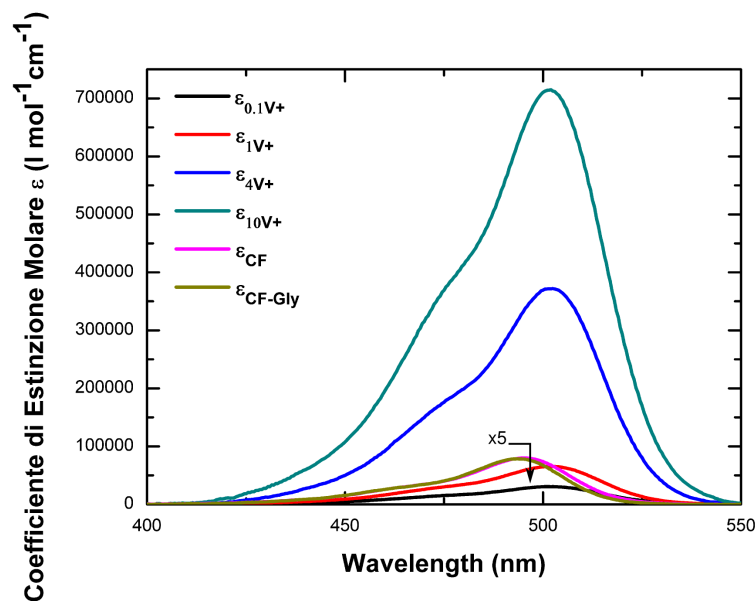


Figure 3.15: Molar extinction coefficients of charged samples 0.1V+, 1V+, 4V+ and 10V+, Carboxyfluorescein-Glycin complex and Carboxyfluorescein-NHS measured in PBS at pH 7.4 as a function of excitation wavelength: the absorbance peak values of the curves for 1V+, Carboxyfluorescein-Glycin and dye alone result similar, according to what was expected.

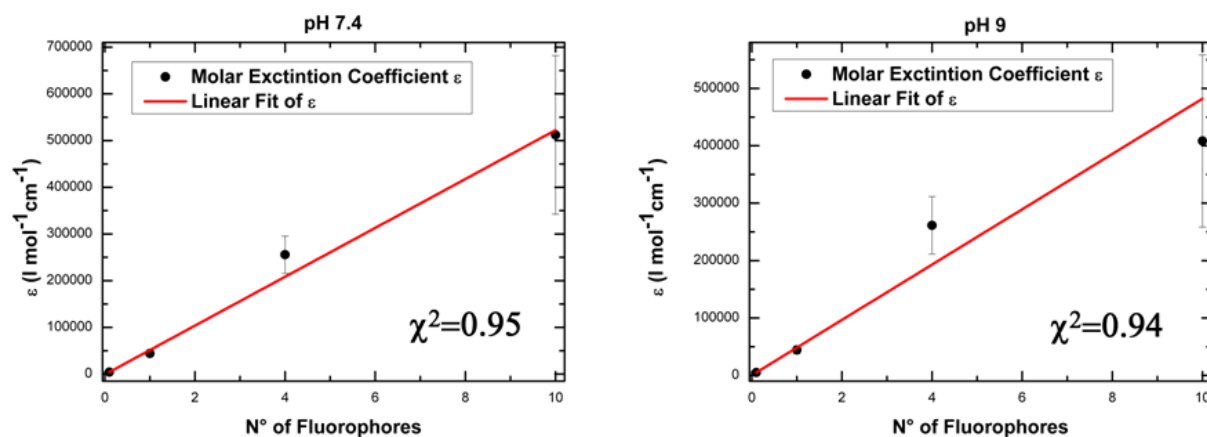


Figure 3.16: Linear fit for the molar extinction coefficients of the charged samples at pH 7.4 and 9 with respective χ^2 values: the slopes of $(52300 \pm 6100) \text{ l mol}^{-1} \text{cm}^{-1}$ at pH 7.4 and of $(47900 \pm 6100) \text{ l mol}^{-1} \text{cm}^{-1}$ at pH 9 may be interpreted as an average molar extinction coefficient per NHS-carboxyfluorescein molecule for the charged specimens at this pH.

of PAMAM dendrimers with linked fluorophores should not vary so much upon acetylation of the dendrimer's surface primary amines. However, we could explain this experimental evidence by considering that, in producing the acetylated samples, a certain amount of material might have been lost due to subsequent dilutions and transfers from a container to another. This made it difficult to be sure about the precise quantity of solid neutral sample obtained, preventing us from calculating the actual concentration of sample in solution and thus affecting the determination of the ϵ values.

3.4.5 Quantum Yields

The fluorescence quantum yields of both charged and neutral samples were determined in Phosphate Buffer Saline at pH 7.4 and in Carbonate Buffer at pH 9 using a solution of Fluorescein in 0.01M NaOH as the standard, according to Eq. 3.4:

$$\phi_F = \phi_{F,ref} \frac{I}{A} \frac{A_{ref}}{I_{ref}} \frac{n^2}{n_{ref}^2} \quad (3.4)$$

with refractive indexes of PBS $-n = 1.35-$ and of water $-n_{ref} = 1.33-$ were assumed to be the same. The values obtained are reported in Table 3.3:

Sample	ϕ_F % pH 7.4	ϕ_F % pH 9.1	Sample	ϕ_F % pH 7.4	ϕ_F % pH 9.1
0.1V+	10 ± 1	13 ± 2	0.1Vn	9 ± 1	12 ± 2
1V+	16 ± 2	19 ± 1	1Vn	12 ± 1	15 ± 2
4V+	12 ± 1	15 ± 1	4Vn	14 ± 4	17 ± 2
10V+	6 ± 0.3	7 ± 0.3	10Vn	6 ± 0.3	8 ± 0.1

Table 3.3: Fluorescence quantum yields of both charged and neutral samples determined in Phosphate Buffer Saline at pH 7.4 and in Carbonate Buffer at pH 9: the errors reported are estimated from measurements carried out on different days.

We can notice that the quantum yield is strongly reduced with respect to the unbound NHScarboxyfluorescein; this could be caused by the fact that the optical properties of a fluorophore could be perturbed by either direct interactions with the dendrimer's end groups, either by weaker interactions, such as with the general local environment or electronic interaction with nearby fluorophores. However, looking at the above table, we note that the samples Quantum Yields do not seem to depend appreciably on the dendrimer's surface charge state (positive or neutral).

3.5 Fluorescence Lifetime Measurements

I employed *Time-correlated single photon counting* (TCSPC), a time-domain method, in order to measure fluorescence decay curves. TCSPC records times at which individual photons are detected by a photomultiplier tube (PMT) or an avalanche photo diode (APD) after a single pulse. The recordings are repeated for many pulses and, after enough recorded events, a histogram of the number of events across all of these recorded time points can be built. This histogram can then be fitted to a decay function (usually a single or multiple exponential decay) from which the lifetime parameters can be extracted.

Fluorescence Lifetimes were evaluated using a Leica TCS SP5 inverted confocal microscope (Leica Microsystems AG, Wetzlar, Germany) coupled to a PicoQuant single-molecule detection module and internal photomultipliers. The excitation source was a 470 nm pulsed laser operated at 40 MHz, with the possibility to attenuate the intensity by 10, 100 or 1000 times. The objective employed was a 20x air-immersion one. The FLIM Wizard available on the software LAS-AF version 2.3.0 was employed to perform the measurements. The emission was detected with a Hamamatsu R955 photomultiplier tube (PMT) which was maintained at 25 °C. A total of 1000 counts were collected at the maximum channel for each pixel. A multiple chambers slide was employed in order to perform all the measurements in the most similar conditions. The concentration of the samples was $\sim 5\mu\text{M}$. For the samples 0.1Vn and 1Vn I did not know the exact concentration, so I tried different dilutions until a proper ($\sim \mu\text{M}$) concentration for FLIM measurement was reached. The fluorescence decay profiles were analyzed either by a tail-fit or by reconvolution of the instrumental response function (IRF) and monoexponential or multiexponential decay of the emission using an iterative nonlinear least-squares curve-fitting method, available in the Symphotime software by Picoquant. I will explain in more detail how the IRF has been estimated in Subsection 3.5.2.

3.5.1 Instrument Calibration

The good functioning of the instrumental setup was tested measuring the fluorescence decay of a standard of Fluorescein, with a well known lifetime of $(4.1\pm0.1)\text{ns}$ in NaOH 0.01M [24]. Fig. 3.17 shows the fluorescence decay curve obtained and tail-fitted with the above mentioned software. As a further check of the reliability of the method, and in order to make comparisons with the samples, I recorded the fluorescence decay at pH 9 of the fluorophore of interest in this work, NHScarboxyfluorescein, and fitted it with a monoexponential, finding a value of $(3.77\pm0.03)\text{ns}$ (see Table 3.5), which is in quite good agreement with the lifetime of 4ns found in literature for the anionic form of Carboxyfluorescein at $\text{ph} > 9$ [25].

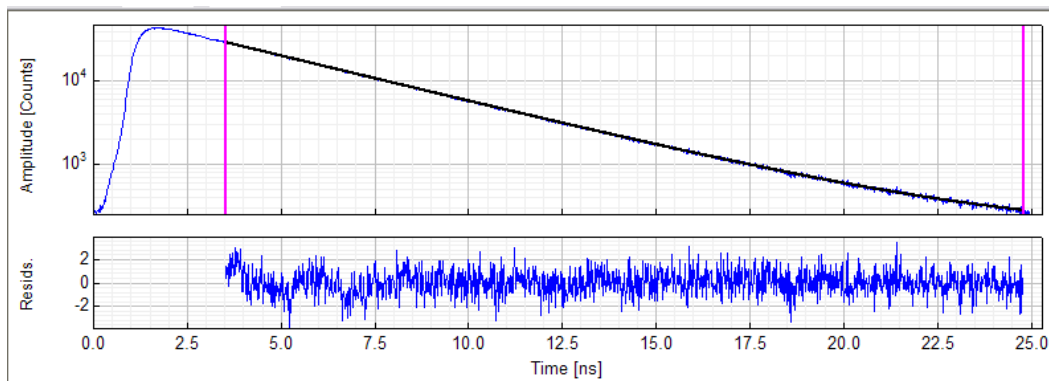


Figure 3.17: Top panel, blue line: TCSPC histogram acquired for the measurement of the fluorescence decay curve of Fluorescein Standard in NaOH 0.01M: the exponential decay fit (black line), performed with the Symphotime software for the time range delimited by the purple lines, yielded a value of (3.95 ± 0.01) ns for the lifetime of Fluorescein, in acceptable agreement with the value found in [24]. Bottom panel: corresponding normalized residues from the fit, with a χ^2 of 1.136.

3.5.2 IRF and Results on NHScarboxyfluorescein

There exist a variety of possible methods to extract the IRF from a measured decay. All of them have characteristic disadvantages, like introducing additional fitting parameters or producing systematic aberrations from the real IRF. Exploiting the fact that NHScarboxyfluorescein has a single-exponential decay, we used the Symphotime software to reconstruct the IRF starting from its decay curve at pH= 9 and used it as IRF for the other samples (see Fig. 3.19). At each pH, fluorescence decay curves were recorded and the values for τ determined averaging the lifetimes from the monoexponential fits performed in two different measurement spots of the same sample and for three slightly different ranges of time for the fit (not including the IRF rise). Then, knowing from Eq. 2.30 that $\tau_R = \tau_F / \phi_F$ and using the values found in literature for the quantum yields of NHScarboxyfluorescein spectroscopically determined at various pH (that were considered similar to those of Fluorescein according to [23]), we could determine $1/\tau_R = k_R \equiv k_{F,CF}$ for NHScarboxyfluorescein at the correspondent pHs by measuring the fluorescence decay time with the FLIM setup. The quantum yield values that I determined for NHScarboxyfluorescein with spectroscopy measurements (and reported in Chapter 4, Fig. 4.2) result in good agreement with the values found in literature. Table 3.4 shows the fluorescence lifetimes τ , the calculated radiative constants $k_{F,CF}$ obtained for NHScarboxyfluorescein and the quantum yield values used to determine the latter, for pH ranging between 4.2 and 8.9. These $k_{F,CF}$ values can be considered "average" radiative rates for the forms of NHScarboxyfluorescein in dynamical equilibrium in the solutions; they will be used in the following to estimate, through the analysis of the decay curves, the quantum yield of the samples.

In Fig. 3.18 is reported the plot of NHScarboxyfluorescein's fluorescence lifetime as a function of pH.

pH	τ (ns)	χ^2	$k_{F,CF}$ (ns ⁻¹)	ϕ_{CF} (%)
4.2	2.61±0.02	1.11	0.096±0.001	25
5.25	2.80±0.03	1.40	0.111±0.001	31
6.1	3.27±0.05	1.61	0.113±0.002	37
7	3.76±0.03	1.15	0.149±0.001	56
7.8	3.80±0.04	1.19	0.195±0.002	74
8.9	3.79±0.03	1.14	0.245±0.002	93

Table 3.4: NHScarboxyfluorescein's fluorescence lifetime τ , radiative rate $k_{F,CF}$ and percentage quantum yield ϕ at respective pH values. The χ^2 value is reported to show the goodness of the fits.

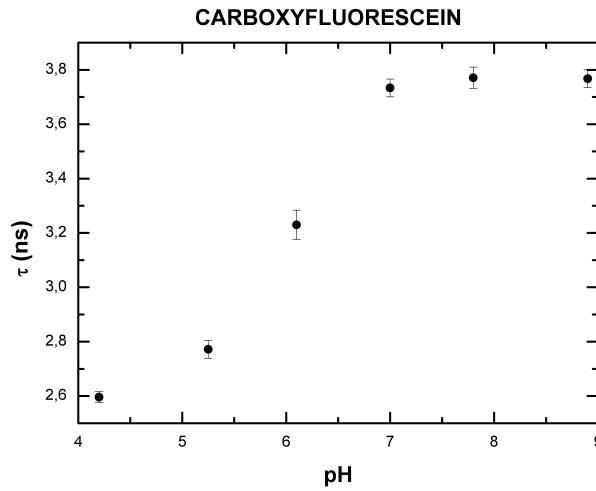


Figure 3.18: pH titration of NHScarboxyfluorescein fluorescence lifetime. The error bars reported are the standard deviations of the lifetimes obtained for two different measurement spots of the same sample and for three slightly different ranges of time for the fit.

3.5.3 Results on the Samples

I am going now to describe the results on the samples. I proceeded to perform three types of measurement on them:

1. I determined the lifetimes of all the charged and the neutral samples at pH 7 by means of a bi-exponential fit of the fluorescence decay curves performed on a range of times not including the Instrument Response Function (tail-fitting);
2. I performed pH lifetime titrations for the samples 4V+ and 4Vn in a range of pHs from 4 to 9; in order to evaluate the quantum yield of the latter ones, we included the IRF in the fits to have exact values for the lifetimes amplitudes (see below for more details): differently from the previous point, we noted that in order to obtain a good fit, a triexponential function was needed, with a third, very short (< 200 ps), lifetime;
3. Following the same procedure adopted in point (2) I estimated the quantum yield

of the sample 1V+ at pH 9 according to Eq. 2.6.4 to compare it with that obtained with spectroscopic methods in Section 3.4.5 of this chapter.

In the following, the results of the three kinds of experiment will be illustrated.

1. At pH 7, the samples, charged or acetylated, display two decay times, one longer similar to that of NHScarboxylfluorescein, and one shorter, not displayed by the dye alone and most presumably attributable to the dendrimer's presence. The values obtained are reported in Table 3.5.

Sample	τ_1 (ns)	τ_2 (ns)	χ^2
0.1V+	3.84±0.01	1.16±0.01	1.14
1V+	3.58±0.01	1.12±0.02	1.14
4V+	3.42±0.01	1.03±0.01	1.20
10V+	3.88±0.01	0.84±0.01	1.08
0.1Vn	3.52±0.01	1.32±0.01	1.12
1Vn	3.52±0.01	1.32±0.01	1.12
4Vn	3.55±0.01	1.30±0.01	1.09
10Vn	3.57±0.01	1.06±0.01	1.12

Table 3.5: Values of the two lifetimes τ_1 and τ_2 found for all the charged and acetylated samples at pH 7, upon performance of a biexponential fit. The errors reported are the standard deviations of the lifetimes obtained for three slightly different fit ranges.

2. To determine the quantum yields of the samples 4V+ and 4Vn at various pH, we used the radiative decay rates $k_{F,CF}$ of NHScarboxylfluorescein as a function of pH derived in Subsection 3.5.2. In the light of what reported in Subsection 2.6.4 of Chapter 2, we could calculate ϕ_F for the samples 4V+ and 4Vn at various pHs knowing a priori only the radiative decay rate of NHScarboxylfluorescein determined as previously mentioned. The fit of the fluorescence decay curves of the samples 4V+ and 4Vn at various pH returned three lifetimes and respective amplitudes (as shown in Fig. 3.20). The third lifetime τ_3 resulted constantly distributed with pH around a value of (230 ± 40) ps for the sample 4V+, and a value of (210 ± 40) ps for the sample 4Vn (see fig. 3.20 for an overview of all the three lifetimes for both samples 4V+ and 4Vn). It is important to stress that the values at pH 7 found with the triexponential fit for τ_1 and τ_2 of the samples 4V+ and 4Vn were in agreement with those returned by the biexponential fit performed in experiment (1), as shown in Table 3.6: this evidence agrees with our hypothesis that in the samples there is a fraction of molecules almost switched off which absorb as the others, but display so many non-radiative decay channels that their fluorescence lifetimes are drastically reduced. This will be discussed in a more global frame in Chapter 4.

The three lifetimes and respective amplitudes were then combined as shown below:

$$\phi_F = k_{F,CF} \frac{A_1\tau_1 + A_2\tau_2 + A_3\tau_3}{A_1 + A_2 + A_3} \quad (3.5)$$

	Sample	τ_1	τ_2
Bi-exp FIT	4V+	3.42 ± 0.01	1.03 ± 0.01
Tri-exp FIT	4V+	3.32 ± 0.14	0.98 ± 0.06
Bi-exp FIT	4Vn	3.55 ± 0.01	1.30 ± 0.01
Tri-exp FIT	4Vn	3.54 ± 0.11	1.16 ± 0.06

Table 3.6: Values at pH 7 found with triexponential and biexponential fit for τ_1 and τ_2 of the samples 4V+ and 4Vn: they result in agreement.

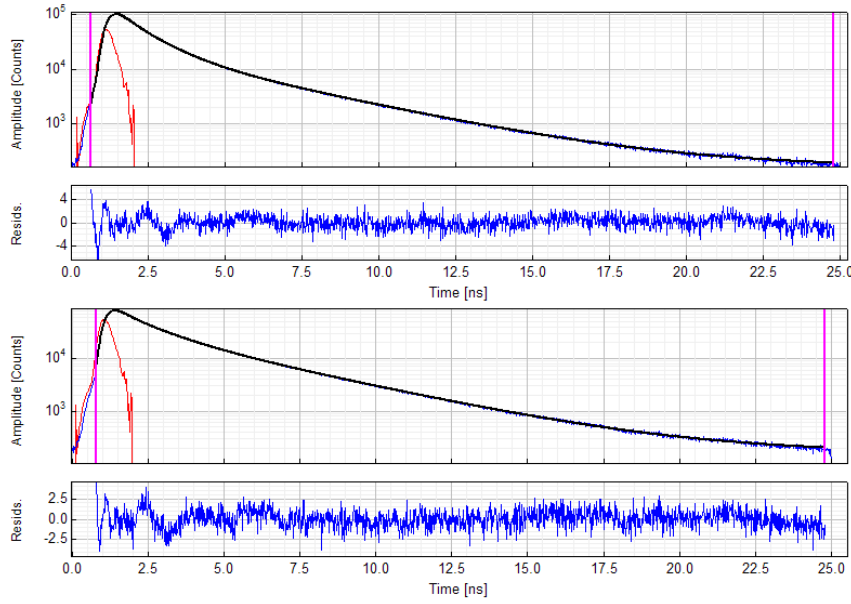


Figure 3.19: Fluorescence decay curve (blue line), triexponential fit (black line) and IRF (red line) for samples 4V+ at pH 9 (top panel) and sample 4Vn at pH 7 (bottom panel). For both samples, fit residues are also reported in the small panels under the respective decay curves.

We applied Eq. 3.5, according to the equation Eq. 2.44, to calculate the ϕ_F for the samples 4V+ and 4Vn, finding the values listed in Table 3.7.

pH	ϕ_F of 4V+	ϕ_F of 4Vn
4.2	15 ± 1	15 ± 5
4.65	12 ± 1	16 ± 1
5.25	13 ± 2	16 ± 5
5.62	12 ± 1	16 ± 1
6.1	10 ± 1	20 ± 1
6.48	9 ± 1	20 ± 1
7	13 ± 3	20 ± 2
7.8	19 ± 1	24 ± 1
8.9	26 ± 1	31 ± 4

Table 3.7: Quantum Yields ϕ_F obtained for the samples 4V+ and 4Vn at various pH by means of fluorescence lifetime measurements. The errors reported are the standard deviations of the Quantum Yields obtained for two different measurement spots of the same sample and for three slightly different ranges of time for the fit.

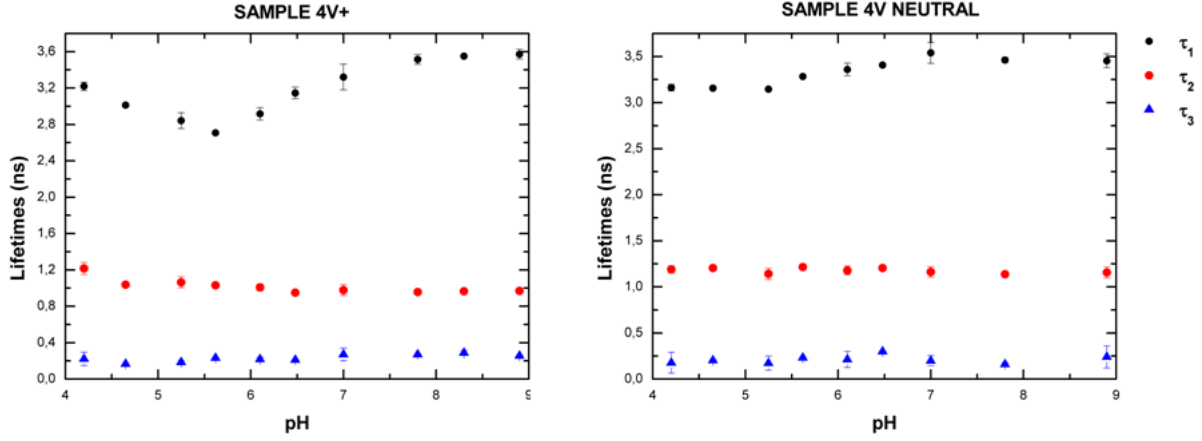


Figure 3.20: Lifetimes τ_1 , τ_2 and τ_3 returned by the triexponential fit of the samples 4V+ (left panel) and 4Vn (right panel) as a function of pH. The error bars reported are the standard deviations of the lifetimes obtained for two different measurement spots of the same sample and for three slightly different ranges of time for the fit. From the two graphics, we see that τ_2 and τ_3 show an almost constant trend for varying pH and that τ_1 , while it does not change excessively, has a trend that reminds the one seen for the fluorescence intensities reported in section 3.4.

Comparing the values of ϕ_F obtained with the spectroscopic methods and reported in Section 3.4.5, on the one hand we observe that they are in good agreement at pH around 7 for both the charged and the acetylated samples: in fact, for the sample 4V+ using the spectroscopy approach we found a $\phi_F = (12 \pm 1)\%$ and with the FLIM technique $\phi_F = (13 \pm 3)\%$, while for the sample 4Vn using the spectroscopy approach we obtained a $\phi_F = (14 \pm 4)\%$ and with the FLIM technique $\phi_F = (20 \pm 2)\%$. On the other hand, the values of ϕ_F found at pH 9 with the FLIM technique are slightly higher than those determined with spectroscopy for both the samples, and mostly for the neutral one: for the sample 4V+ using the spectroscopy approach we found a $\phi_F = (15 \pm 1)\%$ and with the FLIM technique $\phi_F = (26 \pm 1)\%$, while for the sample 4Vn using the spectroscopy approach we find a $\phi_F = (17 \pm 2)\%$ and with the FLIM technique $\phi_F = (31 \pm 4)\%$. Plots of the quantum yields as a function of pH for both methods and a possible explanation for this apparent discrepancy will be reported in Chapter 4.

3. Using the same procedure of point (2), the fluorescence decay curve of the sample 1V+ at pH 9 was recorded and fitted with a triexponential decay function; applying Eq. 3.5, I found for this sample a percentage quantum yield of $(20 \pm 1)\%$ at pH 9, which is in very good agreement with the value found in Section 3.4.5 at the same pH $(19 \pm 1)\%$.

3.6 Single Molecule Detection (SMD)

For this experiment, measurements were performed using a Leica DM6000 setup with module AM TIRF MC, composed of an inverted wide-field microscope (transmission and epifluorescence) equipped with a TIRF module (laser at 405nm, 488nm, 561nm, 635nm), fast excitation and emission filter wheels, motorized and galvanometric stage Super-Z, incubator chamber for temperature and CO₂, EM-CCD camera ImagEM mod. C9100-13 by Hamamatsu Photonics K.K. (Japan). Single-molecule spots and tracks were analyzed by means of the software LAS-AF version 2.3.0 by Leica. To elaborate the data I also used Imaris 7.2.3, a 3D and 4D Real-Time Interactive Data Visualization Software by Bitplane. For all the experiments, a HCX PL APO 100x oil-immersion objective with N.A. 1.47, an emission filter Semrock FF01-525/45, laser wavelength of 488nm, laser intensity 100% and a dichroic with cut at $\lambda = 502\text{nm}$ were employed. The measurements were carried out integrating on the whole CCD (512×512 pixel), using an exposure time of 100ms, gain 1 and EM gain 1000 for the CCD.

3.6.1 Sample Preparation

Samples on which I performed single-molecule experiments were 1V+ and 10V+. Solutions of concentration respectively 10pM and 1pM in dendrimer were prepared by subsequent dilution of an appropriate quote of the samples' stocks in water, for a total of 500 μl . Each of these solutions was put in WillCo dishes (glass-bottom Petri dishes) large 22 mm in diameter. The WillCos were treated as follows before being filled with the solutions: using a diamond tip, I etched a little cross in the center of each dish, which would help me finding the focus when performing the measurements in TIRF mode; then, in order to become as clean as possible, all the WillCos underwent extensive acid-base washes: first, 5' wash with HCl 0.1M, after removing the acid other 5' wash with milli-Q water, after removing the water 5' wash with NaOH 0.1M and lastly, after removing the base, other 5' wash with milli-Q water. At this point, the dishes were carefully dried by means of a nitrogen flow. As already specified in Chapter 2, Section 2.6.6, single-molecule experiments are preferably performed on immobilized molecules; to stick the dendrimer-dye(s) molecules to the WillCo's glass bottom, I exploited a technique in use at NEST Laboratories for bonding microfluidic chips to the bottom of a glass dish, the **Oxygen Plasma** [26]: subjecting the WillCos to an air plasma exposes the OH- of the glass groups SiOH, thus making the dish bottom negatively charged and more hydrophilic (cleaning the dishes as well). By putting the sample solutions containing positively charged dendrimers inside these dishes, we can be sure that most of the molecules have bound to the glass surface and can thus be considered as immobilized. The recipe I followed was developed for the plasma machine available at NEST (Colibri Multipurpose Plasma Machine, Gambetti Kenologia Srl, Milan, Italy) introducing a single gas, oxygen. In this procedure, the WillCo dish is placed in the center of the plasma cleaning chamber and the recipe for "glass cleaning" is run. When completed, air is vented in the chamber and

the door is opened to remove the glass-cleaned dish. The settings for glass-cleaning are: Plasma Exposure Time=120s, Gas Stabilization Time=60s, percentage of oxygen=10%, Power=100W, Base Vacuum=0.25mBar.

The solutions of samples in water prepared as illustrated above were put in the WillCos, and left there for several minutes in order to allow the molecules to bind to the negatively charged glass bottom; then, water was removed by means of a pipette, the dishes were rinsed and Carbonate Buffer at pH 9 was added. This double step (water and then buffer) was needed: in fact, at pH 9 the primary amines of PAMAM dendrimer's surface start deprotonating, thus making more difficult the linking to the negatively charged glass. Therefore, I opted for this solution: let the molecules bind to the glass in water, remove water immediately after that and add Carbonate Buffer at pH 9 in order to perform single-molecule measurements in conditions as good as possible to detect the fluorescence signal. Note that, for each measurement, a corresponding one was performed on a WillCo containing 500 μ l of Carbonate Buffer at pH 9, in order to check that the background signal was negligible with respect to that coming from the single molecules.

I prepared also a solution 0.05pM of NHScarboxyfluorescein in Carbonate Buffer at pH 9, by subsequent dilutions of a stock solution 65mM in Dimethyl Sulfoxide (DMSO). Since NHScarboxyfluorescein does not possess positive charges which could mediate the glass-linking, we covered the WillCo's bottom with a layer of Polylysine (ϵ -poly-L-lysine, EPL), which is a small natural homopolymer of the essential amino acid L-lysine that is produced by bacterial fermentation. As shown in Fig. 3.21, Polylysine presents a positively charged end which allows it to bind to the hydroxyl group of the glass. With this expedient, I managed to link at least part of the NHScarboxyfluorescein molecules to the dish, in order to study the single, immobilized molecules. Experimentally, I put

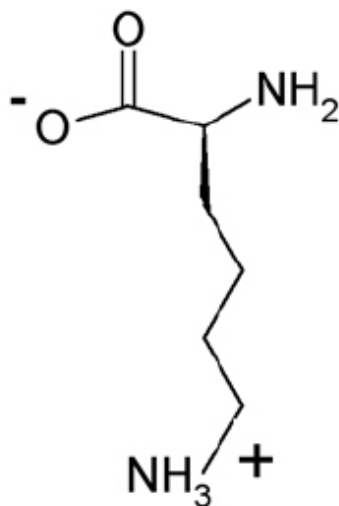


Figure 3.21: Chemical structure of Polylysine.

100 μ l of 0.01% Polylysine solution by Sigma Aldrich in two Willco dishes and let them dry under the laboratory hood. Next, I put in one of them 500 μ l of a solution 0.05pM of NHScarboxyfluorescein in Carbonate Buffer at pH 9, and in the other the same amount of

Buffer alone as a reference. I allowed some time for the NHScarboxyfluorescein molecules to bind to the polylysine and thus to the glass, then I removed the Buffer (together with the molecules that had not bound to polylysine) and replaced it with the same amount of fresh one. Single molecules resulted quite visible with this procedure, and the data obtained were analyzed and processed with the software Imaris as described below.

3.6.2 Data Acquisition and Analysis

The time-stacks of images obtained from TIRF single-molecule measurements for both the samples and the buffers were analyzed by means of the Bitplane's Imaris software, version 7.2.3. This software exploits a macro that selects a certain number of bright spots in the images, according to discrimination parameters that the user can set. The first thing we must take into account is the background, which may be due to various factors, such as for example the CCD offset and the sample autofluorescence. In this experiment, I subtracted the background from my images with the function "thresholding", setting a $4\mu\text{m}$ width for the gaussian filter, an estimated diameter of $0.5\mu\text{m}$ for my molecules; an opportune minimum value of Quality (intensity at the center of the spot) was chosen in order to select the single-molecules spots. Since the molecules visualized were supposed to be immobilized to the glass of the WillCo, in determining the particle trajectories I selected only those that displaced less than $2\mu\text{m}$ from the center of the spot and that lasted more than 0.3s (3 frames, since each is long 100ms). At the end of this procedure, I obtained a number of tracks of about 200 for the sample 1V+ and about 40 for the sample 10V+. For NHScarboxyfluorescein I found a total of about 270 tracks. This discrepancy may be linked to the fact that the sample with 10 fluorophores linked, the 10V+, is likely to have a reduced probability of binding to the glass with respect to the sample 1V+ which has only one site occupied by a dye: 10V+ shows an increased probability that part of the sample which did not adsorb onto the glass was removed together with water during the relative step. It is also noteworthy to stress how the calculation of trajectories for the solutions containing only the Buffer displayed a number of tracks $\ll 10$ for all the samples.

The software was set to return several quantities, such as the mean intensity of the spots during the acquisition time, the maximum and mean intensity and the duration of each track and the respective standard deviations of these quantities, where applicable. All these data were exported to Excel to be further analyzed and processed.

Fig. 3.22 reports the frequency counts histograms of mean intensity $\langle I \rangle$ for all of the three samples examined, built from the mean intensity data returned by Imaris. Our idea was trying to discriminate the populations of dyes with lifetimes τ_1 and τ_2 found in Section 3.5 by means of single-molecule experiments. From Fig. 3.22 it is not possible to distinguish different populations for the samples 1V+ and 10V+ with respect to NHScarboxyfluorescein-Glycine: the three curves are centered about at the same mean intensity, they almost overlay with each other and indeed the samples 1V+ and 10V+ seem to display higher brightness values (see caption of Fig. 3.22). This may be due to the

fact that the single-molecule setup employed has an integration time of \sim ms, which is too long to allow the discrimination of fast, dynamical rearrangements of the dendrimer-dye(s) macromolecules. We suspect that, in this single-molecule experiment, as a consequence of the immobilization of sample molecules (see Subsection 3.6.1), we are observing only one of the various populations present in the samples, and specifically a population of dendrimer-dye(s) macromolecules which has adsorbed to the glass and has blocked in a particularly favorable configuration for the fluorophores to emit. The evidence that the mean intensity histograms result similar for the samples and for NHS-carboxyfluorescein-Glycine indicates that this population is the one with longer lifetime τ_1 .

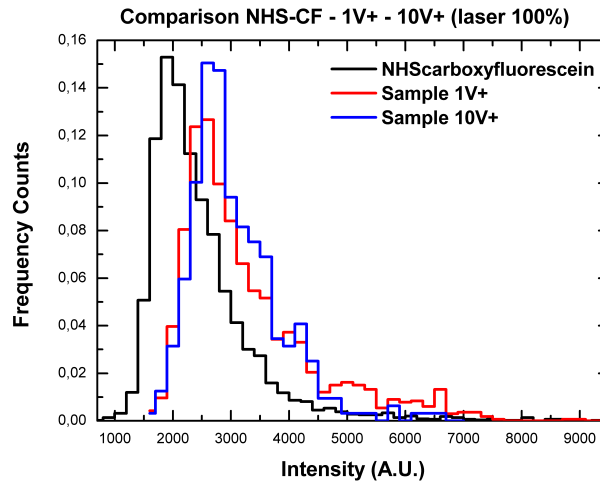


Figure 3.22: Frequency counts histogram of mean intensity recorded for the three samples 1V+, 10V+ and NHS-carboxyfluorescein: the intensity measured by the CCD is proportional to the brightness since we are considering single molecules.

3.6.3 Single-Molecule Statistics

I performed a statistic analysis of the fluorescence intensity traces for both the samples 1V+ and 10V+. The results can be summarized as follows.

- For the sample 1V+, a total of 200 tracks were detected by Imaris; then, I manually selected a number (~ 50) of tracks from the time-stacks of images recorded by LAS-AF software and not corrected for the background. I found that the 70% of these showed the expected trend for a single molecule which switches off after a certain time, that is a single step, as reported in Fig. 3.23 (red and blue lines). The 25% of the tracks were of the kind shown by the black line in Fig. 3.23: in this type of traces, curves started from a fluorescence intensity value lower than in the previous type, meaning that about $1/4$ of the 1V+ molecules are partially switched off since the beginning of the acquisition. The remaining 5% of the tracks displayed an intensity increase limited in time and beginning several frames after acquisition had started: these trends are attributable to blinking molecules, and are shown in Fig. 3.26 (right panel).

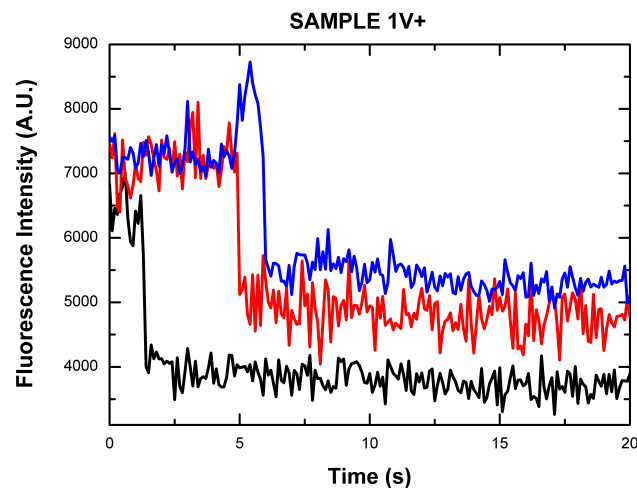


Figure 3.23: Examples of fluorescence intensity traces as a function of acquisition time (s) for sample 1V+: the figure shows single steps, which is what we expected to see for the sample 1V+ which should have an average of one linked fluorophore per dendrimer.

- For the sample 10V+, a total of 40 tracks were detected and analyzed following the same procedure explained in the previous point; the 50% of them showed the behaviour reported in Fig. 3.24, that is similar to a single-step.

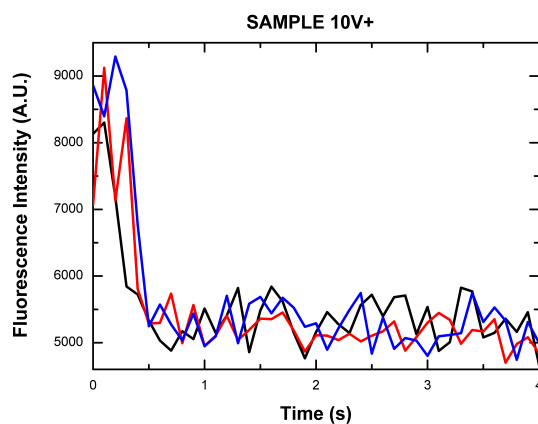


Figure 3.24: Example of fluorescence intensity traces as a function of acquisition time (s) for sample 10V+ showing a single step.

The 30% of the tracks showed a fluctuating behaviour, most probably due to the presence of more than one linked fluorophore, as reported in Fig. 3.25. The remaining 10% of the tracks displayed an intensity increase limited in time and beginning several frames after acquisition had started: these trends are attributable to blinking molecules, and an example is shown in Fig. 3.26 (left panel).

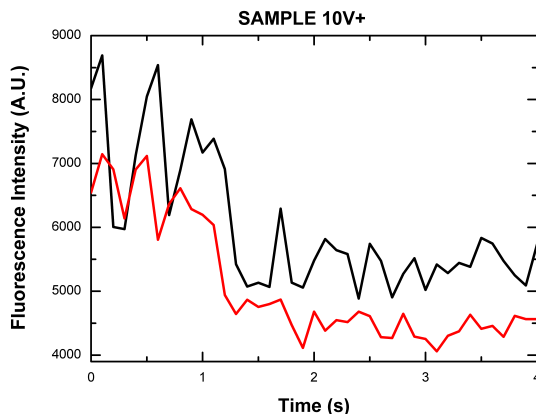


Figure 3.25: Example of fluorescence intensity traces as a function of acquisition time (s) for sample 10V+, showing a strongly fluctuating behaviour.

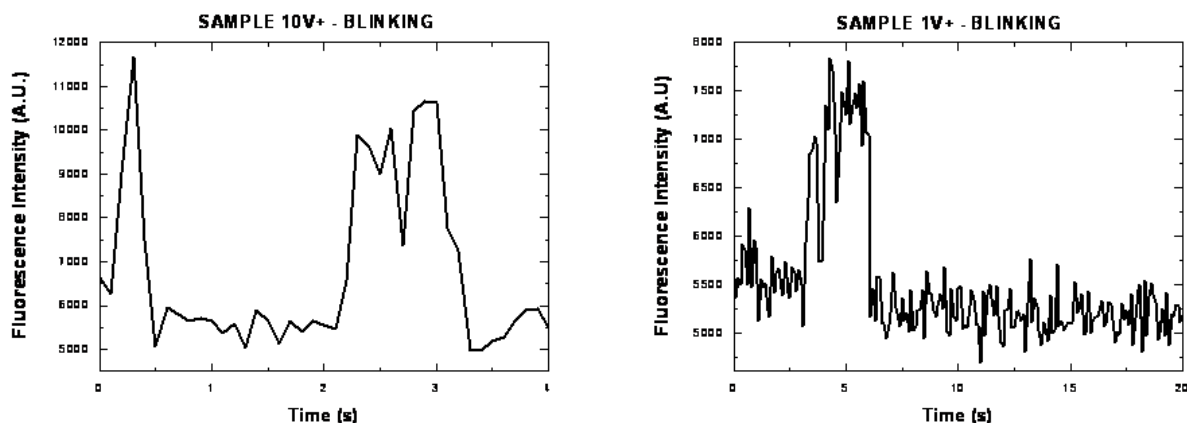


Figure 3.26: Typical *blinking* profiles, a behaviour found in the 10% of the tracks of sample 10V+ (left panel) and in the 5% of tracks for the sample 1V+ (right panel).

3.7 Fluorescence Correlation Spectroscopy (FCS)

Fluorescence Correlation Spectroscopy (FCS) measurements were performed using a Leica TCS SP5 inverted confocal microscope (Leica Microsystems AG, Wetzlar, Germany) coupled to a PicoQuant single-molecule detection module and equipped with two SPAD (single photon avalanche diode) external detectors. Excitation was achieved using a 488 nm Argon laser turned to the 50% of its intensity. Fluorescence emission was collected through a Semrock FF01-550/88 single-band bandpass filter and split with a 50/50 splitter between the two detector channels. This was done in order to avoid the artefact of afterpulsing: in fact, since two detectors produce afterpulses independently from one another, the probability that afterpulsing occurs in two detectors simultaneously is very low. If the same signal is recorded in both channels the cross-correlation contains the same information on dye diffusion and dark states, but not the afterpulsing. For all FCS experiments a 63x 1.2 NA water lens and Immersol ($n = 1.334$ at 23°C) as immersion

fluid for water-immersion objectives were used. The FCS Wizard available on the software LAS-AF and the Symphotime software by Picoquant were employed to perform the measurements and the autocorrelation curves fitting, respectively.

3.7.1 Correction-Ring: adjusting cover glass correction

Spherical aberration is an optical effect that occurs due to the increased refraction of light rays when they strike close to the border of a lens in comparison with those that strike nearer the centre. Each microscope objective is designed to be fully corrected for spherical aberration for a specific cover glass thickness, usually 0.17mm. For our water immersion objective a special correction collar (the *correction ring*) allows correction of spherical aberration for different cover glass thicknesses and different temperatures. This needs to be redone each time the cover glass is changed. Note that additional spherical aberration is introduced when the refractive index of the sample does not match that of the immersion medium. Therefore, a crucial step in FCS is to match refractive indices of immersion medium and sample as well as adjusting the objective to the respective coverslip. In this thesis, we accounted for this by using a 150 μm -slide glass bottom dish with 8 wells. One chamber contained the calibration solution - a solution 5nM of Fluorescein in NaOH 0.01M - and the other chambers contained 200 μl of 1V+, 10V+ and Carboxyfluorescein-Glycine solutions in Carbonate Buffer at pH 9 with concentration 20nM. At the beginning of the experiment, I adjusted the correction ring of the water objective according to manufacturer's instructions as requested in the relative step of the FCS Wizard. During the acquisition, every time I moved on to a different well I checked the correction ring and optimized it if necessary. Once the cover glass was adjusted, I focused about 50 μm above the glass-water interface into the solution. Acquisition duration was set to half an hour for each measurement.

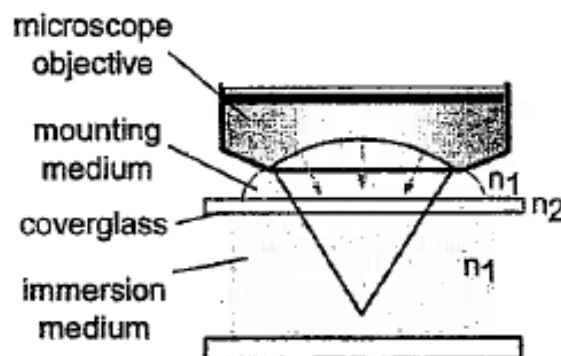


Figure 3.27: Schematic of the propagation of the optical wavefront in a refractive index-matched configuration for a water objective and Immersol mounting medium with a correction collar to compensate for the thickness of the cover glass.

3.7.2 Calibration with Fluorescein Standard

I performed a preliminar FCS measurement on a solution 5nM of Fluorescein in NaOH 0.01M with known diffusion coefficient to determine V_{eff} and the Structure Parameter κ from the autocorrelation curve fit. Then, I applied the values obtained for the reference to the fits I performed on the other samples. In particular, imposing for Fluorescein standard a diffusion coefficient of $(475 \pm 125) \mu m^2/s$, the fit returned $V_{eff} = 0.198$ fl and $\kappa = 5.625$ (Fig. 3.28). A potential problem for calibrating the effective volume could be

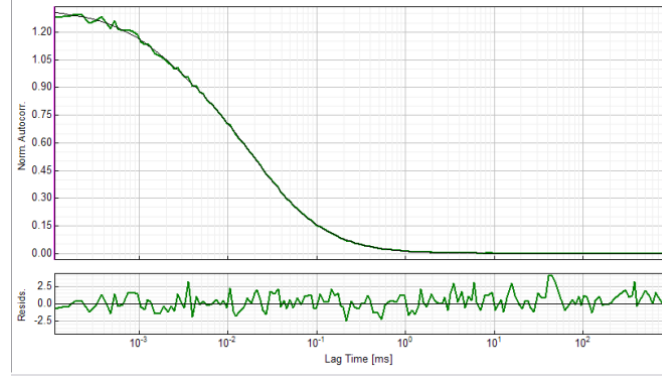


Figure 3.28: Top panel: autocorrelation function $G(\tau)$ (green line) and fit (grey line) performed with the Triplet State Model for Fluorescein standard 5nM in NaOH 0.01M: the $G(0)$ is ~ 1.33 , so the average number of molecules in V_{eff} is 0.75. Bottom panel: fit residues; the χ^2 is 1.66.

optical saturation. Optical saturation means that the total emitted fluorescence does not increase linearly with laser intensity. However, the intensity range in which the molecular fluorescence scales about linearly with excitation intensity is the most useful range for FCS. Indeed, optical saturation in the context of FCS leads to an apparent increase of the detection volume and an underestimation of the diffusion coefficient. To choose an appropriate laser intensity in order to avoid optical saturation, we varied the excitation intensity impinging on the 5nM solution of Fluorescein in NaOH 0.01M and plotted the resulting counts per second (cps) and molecular fluorescence (cpm) as a function of the intensity values in μW . We could adjust the power of the laser using an acusto-optic beam splitter (AOBS); the effects of the percentage setting of the AOBS (Laser Intensity % in the LAS-AF Leica software) on the power of the laser are reported in Fig. 3.29. Since saturation becomes apparent as non-linearity, I decided to employ a 10% laser intensity, which lies in the linear range of the graphic, as shown in Fig. 3.30 and 3.31.

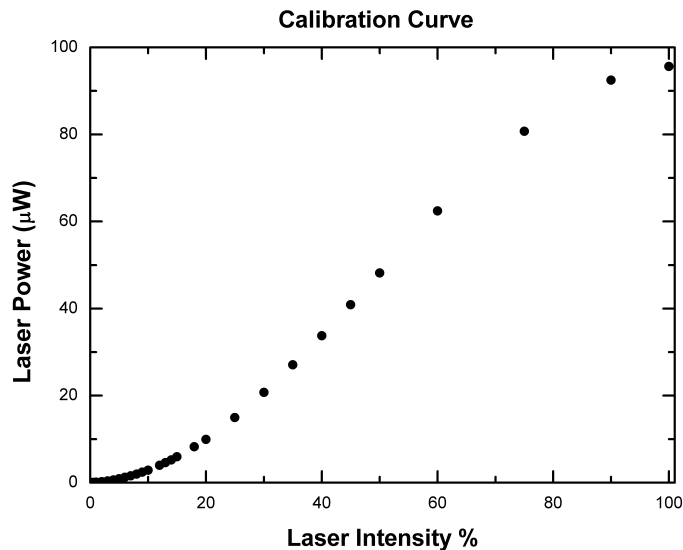


Figure 3.29: Values of laser power (μW) detected by a powermeter immediately after the objective, as a function of the intensity percentage indicated on the LAS-AF Leica software.

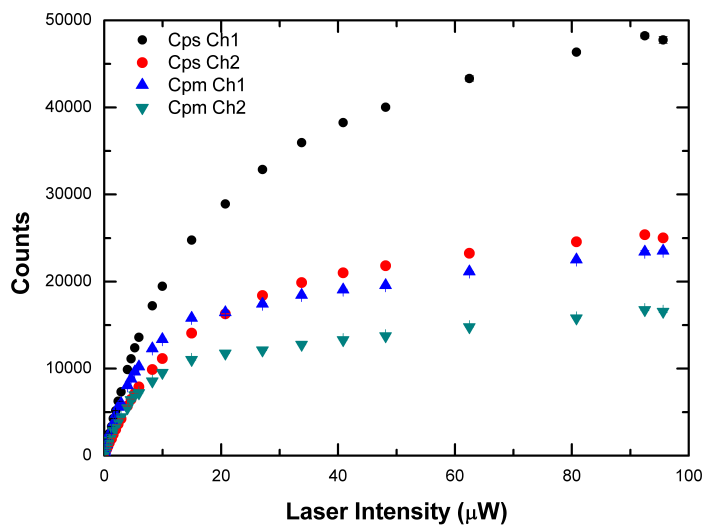


Figure 3.30: Counts recorded per second (cps) and per molecule (cpm) for both detector's channels as a function of the laser intensity (μW) read by the powermeter.

3.7.3 Fit of Autocorrelation Curves

The FCS curves obtained for the solutions 20nM of 1V+, 10V+ and NHScarboxyfluorescein-Glycine were fitted with the Triplet State Model described in Section 3.7, imposing a V_{eff} of 0.198fl and a κ of 5.625, as found for standard Fluorescein. For NHScarboxyfluorescein-Glycine, we obtained a measurement for the diffusion coefficient $D = 365\mu\text{m}^2/\text{s}$, which is in good agreement with the values of D found in literature for Fluorescein and its derivatives, and which we expected to obtain since Glycine is a small molecule if compared to the

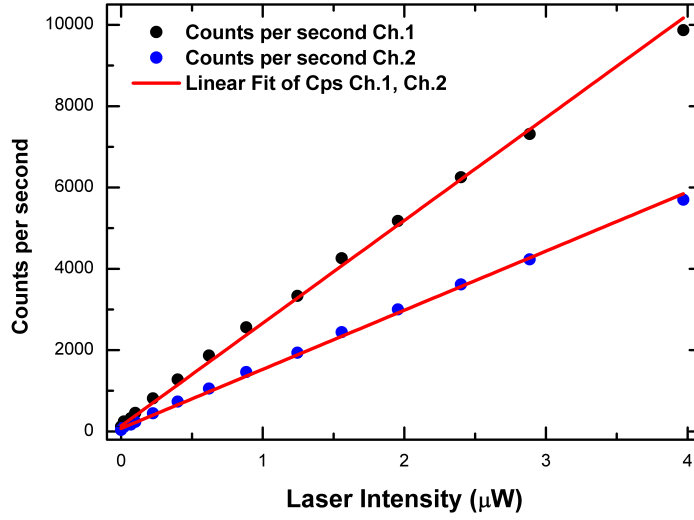


Figure 3.31: Fit of the linear range of counts per second (cps) recorded by both of the detector's channels as a function of the laser intensity (μW) read by the powermeter. The χ^2 is 0.99 for both fits. The percentage laser intensity employed in the FCS experiments of this thesis (10%) lies near the edge of this linear range, since it corresponds to an intensity read by the powermeter of (2.88 ± 0.01) , and is therefore a proper intensity value to use in order to avoid optical saturation.

dye itself, and should therefore decrease only slightly the diffusivity of fluorescein when attached to it. For the samples 1V+ and 10V+ the fit returned values for the average concentration $\langle C \rangle$ quite below the theoretical one (20nM), 2.5nM and 13.1nM, respectively. Because PAMAM dendrimers are positively charged in solution (having primary amines as end groups), significant adsorption of these molecules to the negatively charged silica surface was observed: this should occur through hydrogen bonding of dendrimer terminal amine groups to surface silanol groups and electrostatic interactions between protonated terminal amine groups on the dendrimer and deprotonated silanols on the surface. Clearly, this prevents a fraction of molecules from diffusing, so the real number of molecules in solution free to diffuse in and out of V_{eff} is lower than the expected considering a concentration 20nM. This phenomenon was already observed in [27]: to reduce the adsorption of these probes to silica surfaces, the labeled dendrimers can be reacted with succinic anhydride, converting the primary amine end groups to negatively charged carboxylic acid groups. These carboxylated dendrimers do not detectably adsorb to silica from aqueous solution.

We also tried to determine the diffusion coefficients of 1V+ and 10V+ with the FCS technique, which was not found in previous publications. The values returned by the fit for the diffusion coefficients of the samples 1V+ and 10V+ are too high if compared to those commonly measured for dendrimers with other techniques (i.e. Diffusion NMR): we found $398 \mu\text{m}^2/\text{s}$ for 1V+ and $377 \mu\text{m}^2/\text{s}$ for 10V+ compared with values ranging between $70 \mu\text{m}^2/\text{s}$ (at pH 9, [28]) and $188 \mu\text{m}^2/\text{s}$ (not specified pH, [29]) available in literature.

The possible causes of this discrepancy will be discussed in Chapter 4.

3.7.4 MCS Traces

Multi Channel Scaler curves (MCS, or fluorescence intensity trace, or time trace) are plots of the fluorescence intensity as a function of time; the single photon events are accumulated into bins or “channels” of several ms. In my case, the binning was 1ms. What results is a time trace of the fluorescence intensity from which an histogram of the detected intensity per ms can be obtained. Moreover, these curves allowed me to determine the effective concentrations of the former in the measurement wells. In fact, as discussed in the previous section, part of the sample molecules result adsorbed onto the bottom glass of the slide. Fig. 3.32 reports the MCS trace that I obtained for Fluorescein 5nM employed in the previous section as reference. The Symphotime software returns the minimum and maximum number of photons counted per ms, their average and their standard deviation σ . MCS traces were recorded for the samples 1V+, 10V+

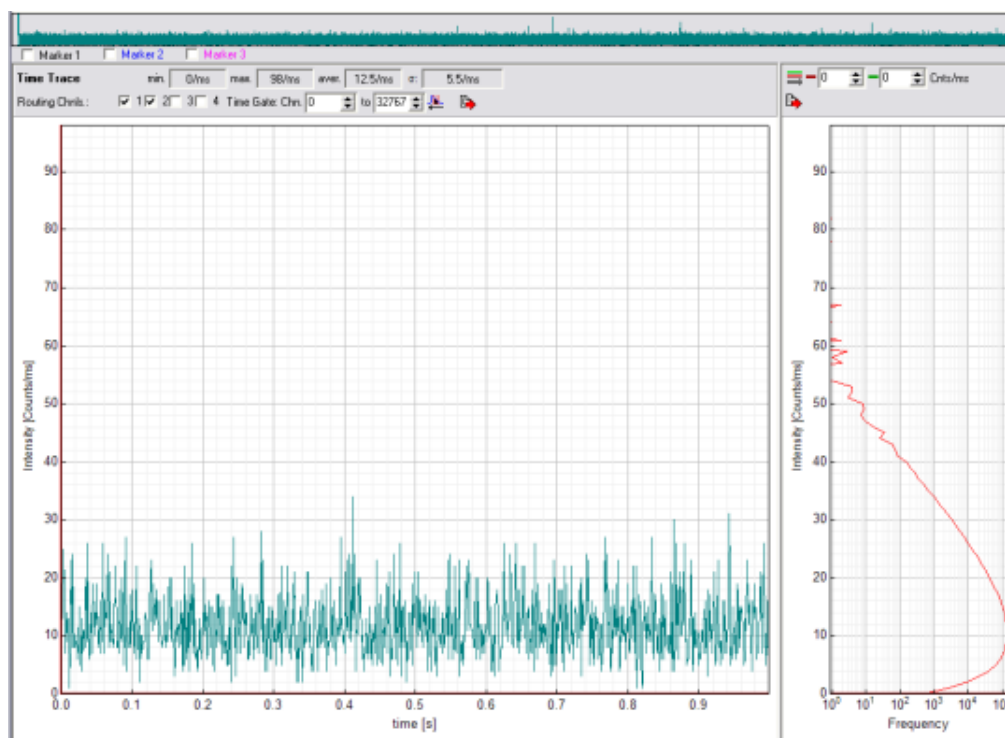


Figure 3.32: Green trace: piece of the MCS trace in the first second of standard Fluorescein 5nM (zoom of the panel above, which is a sketch of the whole trace): the average counts/ms are 12.5, with a standard deviation $\sigma = 5.5$. In the right panel is shown the histogram of the counts intensities as a function of frequency. I will consider again these curves in Chapter 4.

and NHScarboxylfluorescein-Glycine 20nM; I measured FCS and MCS curves also for a solution containing only 200 μ l of Carbonate Buffer at pH 9, obtaining an average number of counts/ms of 0.5 and a σ of 0.8. This will be considered background. The FCS curve for the buffer showed no significant autocorrelation of the fluorescence signal, as expected. The average counts/ms, corrected for the background, and σ are reported in Table 3.8.

Sample	(Aver. Counts/ms) $\pm\sigma$
1V+	2.5 \pm 1.8
10V+	14.7 \pm 5
NHScarboxyfluorescein-Glycine	61.4 \pm 10.9

Table 3.8: Average counts per ms and relative standard deviations for the samples 1V+ 20nM, 10V+ 20nM and NHScarboxyfluorescein-Glycine 20nM, as returned by the Symphotime software employed.

As already mentioned in Section 2.6.5, the ideal number of molecules within the detection volume in a FCS experiment would be 0.3–1.5; the fit of the autocorrelation curves yielded $\langle N \rangle = 0.3$ for the samples 1V+ 20nM, $\langle N \rangle = 1.57$ for 10V+ 20nM and $\langle N \rangle = 6.3$ for NHScarboxyfluorescein-Glycine 20nM. I diluted the last two in order to obtain a number of average counts/ms ~ 3 also for the samples 10V+ and NHScarboxyfluorescein-Glycine. By doing so, I also obtained an average number of molecules in the detection volume $\langle N \rangle \sim 0.3$ for these samples. The amount of dilution was evaluated considering that, for the same sample, the ratio between the counts should be equal to the ratio of concentrations (see Eq. 2.32). Therefore, I derived the dilution factor for the two samples from the ratio of the counts/ms of 10V+ and NHScarboxyfluorescein-Glycine and those of 1V+:

$$\frac{N_{10V+}}{N_{1V+}} = \frac{14.7}{2.5} = 5.88 \quad \frac{N_{CF-Gly}}{N_{1V+}} = \frac{61.4}{2.5} = 24.56 \quad (3.6)$$

I prepared a solution ~ 4 nM for 10V+ and ~ 0.8 nM for NHScarboxyfluorescein-Glycine and performed FCS and MCS measurements on them, obtaining for the latter an average number of counts per ms of 2.5 for the first one and of 2.7 for the second one (values already corrected for the background of 0.5 counts/ms).

Recalling from Eq. 2.31 that the brightness of a species is also equal to the product of its quantum yield and its molar extinction coefficient, we can determine B for the standard Fluorescein knowing its molar extinction coefficient and quantum yield. As already mentioned in previous sections, at pH 12 (NaOH 0.01M) the quantum yield of Fluorescein is 95% and the ε is about 80000 l mol⁻¹ cm⁻¹, which yields $B = 7.6 \times 10^6$ (l mol⁻¹ cm⁻¹ %). Thus, from the counts/ms reported for standard Fluorescein in Table 3.8 and applying Eq. 2.32, we can evaluate the α factor for this sample, obtaining $\alpha = 3.167 \times 10^{-3}$ ms/(counts cm). We are now able to estimate the effective concentration of the samples 1V+, 10V+ and NHScarboxyfluorescein-Glycine in the measurement wells, using the values of ε and ϕ_F at pH 9 reported in Sections 3.4.4 and 3.4.5; Eq. 3.7 reports an example of calculation for NHScarboxyfluorescein-Glycine 20nM:

$$c_{CF-Gly, 20nM} = \frac{counts}{\alpha \times B_{CF-Gly}} = \frac{61.4 \times 3.167 \times 10^{-3}}{70000 \times 90} \simeq 31 \text{ nM} \quad (3.7)$$

Carrying out the same calculation also for the samples 1V+ 20nM, 10V+ 20nM, 10V+ 4nM and CF Gly 0.8nM we obtained concentrations of 12nM, 14nM, 2nM and 1nM, re-

spectively. We can explain why these concentrations result lower than the theoretical ones recalling that part of these molecules are adsorbed to the slide glass.

In order to try to evaluate the equivalent concentration of molecules stuck to the bottom of the slide, we measured the counts/ms for four different concentrations of sample 1V+ (2.5, 10, 25 and 50 nM), plotted them versus concentration and fitted the scatter with a linear function of the type $y = a + bx$. From the values of the intercept and the slope returned by the fit, imposing the number of counts/ms = 0 (hypothesis of saturation of the OH^- sites on the glass bottom), we determined the concentration of the molecules that are stuck to the glass, which resulted of 1.67 nM. The result obtained with this approximative calculation does account in part for the discrepancies observed between nominal and estimated concentration values, but it is not sufficient to explain them entirely, suggesting that more complicate dynamics should be taken into consideration. Therefore, in the following discussions, we will try to adhere mostly to results which did not require a perfect knowledge of the sample concentration in order to be quantitatively interpreted.

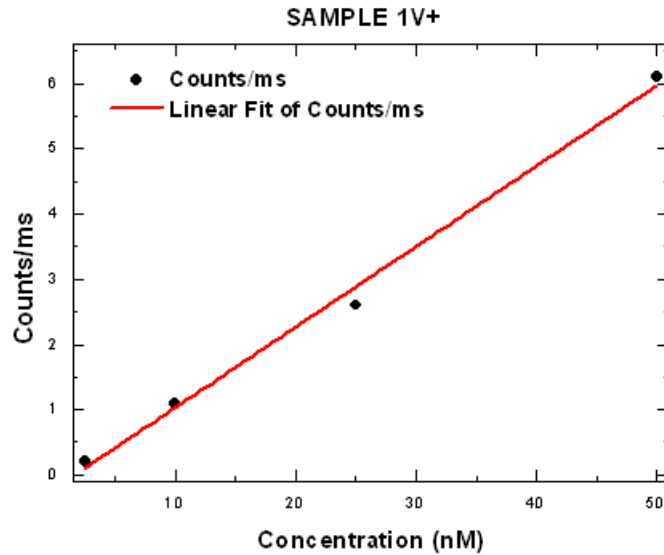


Figure 3.33: Linear fit of photons counted per ms versus concentration for sample 1V+: the fit intercept is (-0.21 ± 0.18) and the slope (0.12 ± 0.01) . The χ^2 is 0.99.

Chapter 4

Impact of PAMAM dendrimers on the photophysics of 5(6)-FAM SE

In this Chapter I will review the experimental results obtained and reported throughout Chapter 3, discuss and analyze them from a global point of view and propose a qualitative interpretation model. From the comparison of the spectral properties of the fluorophore considered in this thesis work, NHScarboxyfluorescein, and the conjugated systems dendrimer-dye(s), we can infer that the linked molecules interact and with some part of the dendrimer, (either end groups, branches or the core), and sometimes also with each other, in ways that may differ in extent and strength from one dye to another; they lead to a change in the photophysical behaviour of the fluorophore which can give information on the structure and dynamics of the dendrimer-dye(s) macromolecules and on their interactions with the local environment.

4.1 Spectral Features

In the light of what illustrated in the previous Chapters, and of the experimental results obtained, we can make three concluding remarks about the impact of PAMAM dendrimers on the spectral properties of NHScarboxyfluorescein:

1. Molar extinction coefficient values of the charged samples followed approximately the scaling trend expected for macromolecules with nominally 0.1, 1, 4 or 10 linked dyes, with an average value per single fluorescein of $(52300 \pm 6100) \text{ l mol}^{-1} \text{ cm}^{-1}$ for pH 7.4 and of about $(47900 \pm 6100) \text{ l mol}^{-1} \text{ cm}^{-1}$ at pH 9. These values are quite close to the extinction coefficient found for NHScarboxyfluorescein-Glycine $65000 \text{ l mol}^{-1} \text{ cm}^{-1}$ at pH 7.4 and $70000 \text{ l mol}^{-1} \text{ cm}^{-1}$ at pH > 9 ; they are a little smaller probably because of the different local environment, which the fluorophore experiences when it is close to the dendrimer surface, with respect to the non-conjugated dye configuration in aqueous solution; indeed, the fluorophore absorption underwent changes also when dissolved in diverse mixtures of NaOH 0.01M and DMF. However, we cannot completely exclude that a small fraction of the fluorophores has been

lost or destroyed during the linking reaction and following purification (causing an average number of attached fluorophore per dendrimer smaller than the nominal one).

2. The quantum yields of both charged and acetylated samples vary substantially, instead, with respect to that of NHScarboxyfluorescein alone, which is about 87% at pH 7.4 and about 90% at $\text{pH} \geq 9$. In fact, it is reduced with respect to the one of the non-conjugated dye for an extent of 80 – 90%. We note that the quantum yield decrease is almost of the same magnitude for the samples 0.1V, 1V and 4V (both charged and neutral), while it results greater for the sample with 10 linked fluorophores, which presents the lowest quantum yield, 6% at pH 7.4 and $\sim 8\%$ at pH 9. The reduction of quantum yield also for 0.1V is not consistent with the hypothesis of self-quenching of the fluorophores linked to the surface (see Chapter 2, Section 2.4.4), which seem to have an impact only as the number of linked fluorophores increases (for 10 fluorophores per dendrimer). It must be caused by direct interactions with the dendrimer, *i.e.* “caging” of the dyes inside some interstice of the dendritic structure. The similar results for charged and “neutral” samples seem to exclude an impact of interaction with the charged amines on the surface of the PAMAM dendrimers.
3. As inferred from the experimental evidences reported in Chapter 3, Section 3.4.3, the linkage to the dendrimer’s surface and the interactions dye-dendrimer affect also the absorption and emission wavelength of NHScarboxyfluorescein, red-shifting both of them of about 5nm. The comparison with the results for free fluorophores dissolved in Dimethylformamide (DMF) links this trend to the different polarity in the local environment for the dyes linked to the dendrimers, since DMF possesses approximately the same solvating properties of the dendrimer.

Thus, according to our experiments, the changes in the spectral properties observed for the dendrimer-dye(s) system with respect to the non-conjugated dye can be related to interactions between linked fluorophores and the dendrimer environment; in order to find a possible explanation for the quantum yield significant decrease, we decided to perform experiments of Fluorescence Lifetime Microscopy on the samples.

4.2 Distribution of Quantum Yields

We chose to carry out this particular type of measurement to investigate if the quantum yield decrease observed with spectroscopic methods was due to the presence in solution of only one population with a single decreased lifetime and therefore quantum yield, by dynamics in the excited states, or rather to the existence of a variety of populations marked by different quantum yields and fluorescence decay rates. In fact, if the probe can exist in multiple conformational states, each of these may display a decay time. The fact that we found a triexponential decay law excludes the first case. Many papers in literature

interpret the multi-exponential decays in terms of conformational distributions [30]. Considering this interpretation, we can describe the three found lifetimes as follows: we found three fluorescence lifetimes for our samples: the one of the same order of magnitude of NHScarboxylfluorescein's (~ 3.5 ns) should represent a population in which the dyes do not significantly interact with the dendrimer environment and thus show unaltered photophysical properties and behaviour; a second lifetime, shorter than the first one (~ 1 ns), indicates the presence of a population of dyes which undergo dynamic quenching with the dendrimer and, possibly, self-quenching (the latter is important particularly in the case of the sample with ten linked fluorophores, which in fact displays a τ_2 lower than the others, for both charged and acetylated samples, according to the presence of a population which undergoes more quenching than the same population type in the other samples); a third, very short, lifetime (< 200 ps) which suggests the existence of a third kind of population, a very quenched one which results almost non-fluorescent. These results suggest the presence of at least three different populations, but there is the possibility that they could be even more, possibly even a distribution of populations.

Our interpretation is supported by the results obtained comparing the plots of the quantum yields as a function of pH determined with spectroscopy and FLIM methods, as described in Chapter 3, Section 3.5. From Fig. 4.1, we can see that the quantum yield's trends for samples 4V+ and 4Vn are similar for the two approaches; the quantum yield's values obtained with the FLIM technique appear slightly lower than those found applying Eq. 3.4: this can be explained by considering that, during data acquisition, some incident light might have reached the detector upon scattering from macromolecular aggregates. This spurious contribute to the collected light might have led us to an overestimation of the amplitude of the population with shortest lifetime, and therefore to an underestimation of the quantum yield, according to Eq. 3.5. This underestimation is more critical for the neutral sample: in fact, due to the reduced charge, electrostatic repulsion is lower for 4Vn than for 4V+, and this favors the formation of aggregates which may scatter the incident light.

Another interesting feature of Fig. 4.1, consists in the different trends for the quantum yields for 4V+ and 4Vn with respect to that of NHScarboxylfluorescein-Glycine (Fig. 4.2): they reflect the trends found for the normalized fluorescence integrals as a function of pH in Section 3.4.2, Fig. 3.11 and 3.12. From the comparison of Fig. 4.1 and Fig. 4.2, we can make some general considerations: the fluorescence intensity of the non-conjugated dye results much more greater for basic pH values (> 7) than that of both charged and acetylated samples, which is consistent with the observed strong decrease of the fluorescence quantum yield of the samples with respect to that of NHScarboxylfluorescein alone; at acidic pHs, as expected for a pH-sensitive dye as NHScarboxylfluorescein, the fluorescence intensity decreases significantly, and therefore the quantum yield too: at $\text{pH} < 5$, we notice that the difference between quantum yield values for NHScarboxylfluorescein and for the samples tends to smooth, and the ϕ reach similar values.

This can be explained by looking at the trend of the ratio of the populations in the

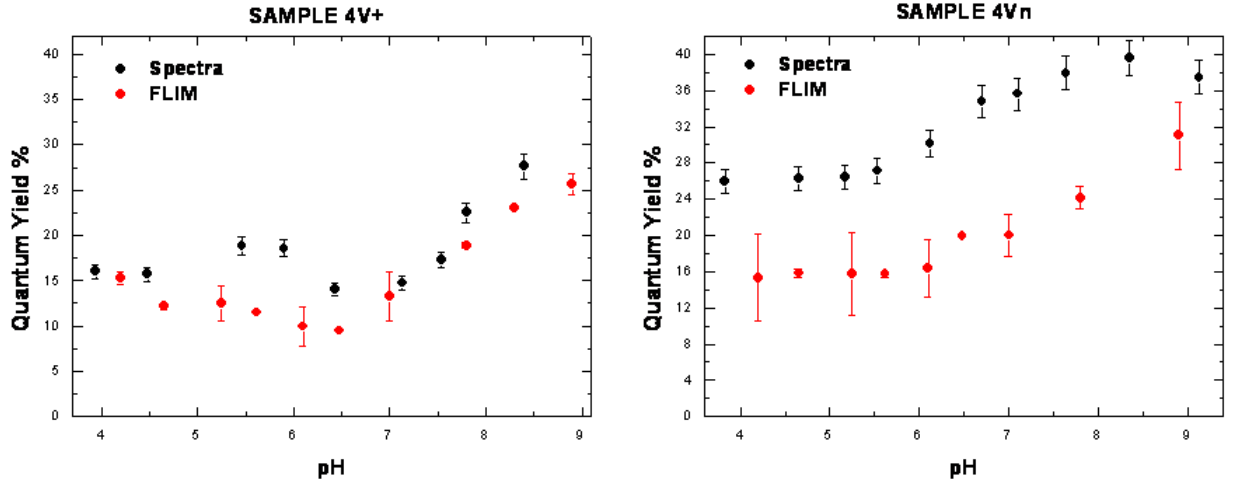


Figure 4.1: Quantum yields of sample 4V+ (left panel) and 4Vn (right panel) for varying pH values obtained by means of spectroscopic (Eq. 3.4, black dots) and fluorescence lifetime (Eq. 3.5, red dots) methods: a comparison. The errors reported derive from the standard deviations of the results obtained in different measurements or with different analysis.

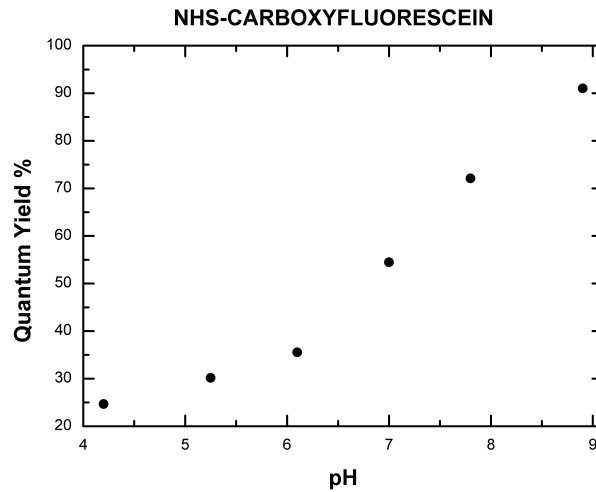


Figure 4.2: NHS-Carboxyfluorescein's fluorescence quantum yield as a function of pH. The error bars are inside the points.

graphics of Fig. 4.3, which report the plots of the normalized amplitudes $\frac{A_i}{\sum_i A_i}$ as a function of pH, for the three lifetimes determined in Chapter 3, Section 3.5: we can see that A_1 , which is proportional to the population with lifetime $\tau_1 \sim 3.5\text{ns}$, increases at $\text{pH} < 5$, which is consistent with a more open and rigid conformation of the dendrimer at that pH, with the internal amines protonated, and reduced interactions with the linked fluorophores. Comparing the top and the intermediate panels of Fig. 4.3, we see that A_2 displays a trend which is specular to that of A_1 : this evidence is easily explainable in the light of our interpretation model, since this is the amplitude of the population with short

lifetime τ_2 , and it is expected to increase as the amplitude A_1 of the population with the longest lifetime decreases. This means that, as the pH becomes more and more basic, the presence of quenched fluorophores increases along with the dendrimer recovering a more flexible and packed conformation. Finally, from the bottom panel of Fig. 4.3 which reports the amplitude A_3 of the population with subnanosecond lifetime τ_3 , we can see that this amplitude remains approximately constant with varying pH, indicating that the sample presents a fraction of molecules which stays in an almost non-fluorescent configuration throughout the whole range of pH.

4.3 Single-Molecule Experiments

We wanted, at this point, to discern if the different lifetimes are given by dynamics in the fluorescein excited state, or if there are indeed subpopulations of fluorophores with different interactions with the dendrimers, and if these population are fixed or change dynamically. In order to do so, we tried to see a distribution (and, possibly, the dynamics) of the molecular brightness with experiments which highlight single molecules properties. Single-Molecule experiments carried out on immobilized molecules with a TIRF microscope did not evidence any different populations (*e.g.* the ones with lifetimes 3.5ns and 1ns) with integrating times of 100ms. Therefore, we decided to employ the Fluorescence Correlation Spectroscopy (FCS) technique, which displays two main advantages with respect to Single-Molecule: it requires molecules in solution, free to diffuse and not immobilized to, and therefore disturbed by, the slide glass, and allows the detection of dynamics with characteristic times of μ s (*e.g.* diffusion). FCS is intrinsically a measurement on single molecules, because only the correlation of fluctuations arising from single molecules remains after averaging. We performed Triplet State Model fits of all the FCS curves obtained, as described in Section 2.6.5 and as reported in Fig. 4.4, 4.5, 4.6, 4.7, 4.8.

In Table 4.1 are reported for clarity the values obtained by the Triplet State Model fit of the FCS curves of all the samples considered. As we can see from Table 4.1, the values

Sample	τ_D (ms)	D ($\mu m^2/s$)	$\langle N \rangle$	$\langle C \rangle_{FCS}$ (nM)	T	τ_T (ms)	Counts/ms $\pm \sigma$	$\langle C \rangle_B$ (nM)
1V+ 20nM	0.022	398	0.3	2.5	0.173	0.0020	2.5 \pm 2.6	12
10V+ 20nM	0.023	377	1.57	13.1	0.158	0.0025	14.7 \pm 5.8	14
CFGly 20nM	0.023	365	6.3	53	0.146	0.0025	61.4 \pm 11.7	31
10V+ 4nM	0.025	343	0.37	3.1	0.187	0.0044	2.5 \pm 2.5	2
CFGly 0.8nM	0.023	378	0.38	3.2	0.149	0.0022	2.7 \pm 2.5	1

Table 4.1: Values for diffusion time, diffusion coefficient, average number of molecules in the detection volume $\langle N \rangle$, average sample concentration $\langle C \rangle_{FCS}$, fraction of molecules in dark state T and typical time of switching to and from this state τ_T , as returned by the fit performed on the experimental data with the Triplet State Model described in Chapter 2, Section 3.7; the last two columns of the table report the average counts/ms for all the samples with respective standard deviation, and average concentration $\langle C \rangle_B$ obtained from Eq. 3.7 in Section 3.7.4. NOTE: the σ for the Counts/ms are those returned by the software for the samples and not corrected for the background's σ .

returned by the Triplet State Model fits for the diffusion coefficients of the samples 1V+ and 10V+ are too high if compared to those commonly measured for dendrimers with other techniques and reported in Subsection 3.7.3; Fig. 4.9 shows a comparison between normalized FCS curves of sample 1V+ 20nM, sample 10V+ 4nM and a theoretical FCS curve for a diffusion coefficient of $70\mu m^2$, as measured for G4 dendrimers in aqueous solution at pH 9 [28]: while the former two almost overlap, the latter curve results right ward shifted with respect to the experimental ones reported, according to what expected

for a macromolecule, such as a dendrimer, displaying a purely diffusive behaviour. In accordance with our interpretation, this discrepancy may be attributed to conformational rearrangements in solution of the dendrimer-dye(s) macromolecules faster than the typical diffusion times, which are of the order of tens of μs . From Fig. 4.10 we can see that also the MCS histograms of the intensities obtained for the samples 1V+ and 10V+ for bins of width 1ms does not permit to distinguish between different populations. Indeed, the two histograms almost overlap: in order to distinguish at least the two populations with longer lifetimes of 3.5ns and 1ns (we did not consider the population with subnanosecond lifetime to be observable) we would expect to see two separate peaks or a broader peak. Instead, we found for the curves of samples 1V+ 20nM and 10V+ 4nM a shape and a width similar to those obtained for NHScarboxyfluorescein-Glycine 0.8 nM: this means that, even if there are different populations, the integrating time of 1ms allow us to see only the effects due to their average, in accordance to the estimated times for structural changes dynamics of the order of μs or tens of μs found in FCS. We also tried to account for the presence of these fast, dynamical changes by fitting the FCS curves of our samples with another model available in the PicoQuant software, the **Conformational Model**, which is described in terms of Eq. 4.3, and consider stochastic dynamical changes between two states with different brightness. The Conformational Model's parameters are the same of the Pure Diffusional Model described in Subsection 2.6.5 plus A_C , β_C and τ_C . A_C is defined as $K(1 - Q)^2/(1 + KQ)^2$ with Q ratio of the quantum yields of the state 1 and of the state 2, and K the equilibrium constant between state 1 and state 2; β_C is the so-called *stretch parameter* ≤ 1 and τ_C (ms) is the relaxation lifetime of the reversible transitions between state 1 and state 2. Fig. 4.11 shows the fit of the FCS curve for the sample 1V+ performed with the three different models: Pure Diffusion, Triplet State and Conformational. In the light of the interpretation frame that we are illustrating, the latter should be the best model to use to perform the fit of the autocorrelation curve of samples 1V+ and 10V+, but unfortunately, the Conformational model available in the software accounts only for two species, while our samples seem to show at least three of them. Nevertheless, the fit performed with this model returned a value for the diffusion coefficients of the samples 1V+ and 10V+ lower than those determined with the Triplet State Model and reported in Table 4.1. In particular, we found a D of $234\mu\text{m}^2/\text{s}$ and of $304\mu\text{m}^2/\text{s}$ for samples 1V+ 20nM and for sample 10V+ 4nM, respectively. Although it is still not the best, this model provides a good step towards optimization of the fitting for the dendrimer-dye(s) FCS curves. We conclude this Chapter with a final consideration on the average concentration values $\langle C \rangle_{FCS}$ and $\langle C \rangle_B$ reported in Table 4.1: the $\langle C \rangle_{FCS}$ values result lower than $\langle C \rangle_B$ values for the samples 1V+ 20nM, 10V+ 20nM and 10V+ 4nM, but particularly we note a significant difference between the ones obtained for the sample 1V+. This evidence can be explained in the light of the interpretation guidelines outlined in this Chapter by saying that FCS measurements performed on this sample could actually detect mainly the most fluorescent, long-lifetime population, which is only a fraction of the entire sample molecules. It is thus clear that

for the sample with only one fluorophore, the probability to detect this free-dye like population is lower than that of the sample with ten linked dyes, and this is the reason of the greater difference found; specifically, for the sample 1V+ 20nM $\langle C \rangle_{FCS}$ was about 1/5 of $\langle C \rangle_B$. This result is in good agreement with what shown in Fig. 4.3, top graphic: in fact, the amplitude A_1 of the longest lifetime is about 1/5 of the overall.

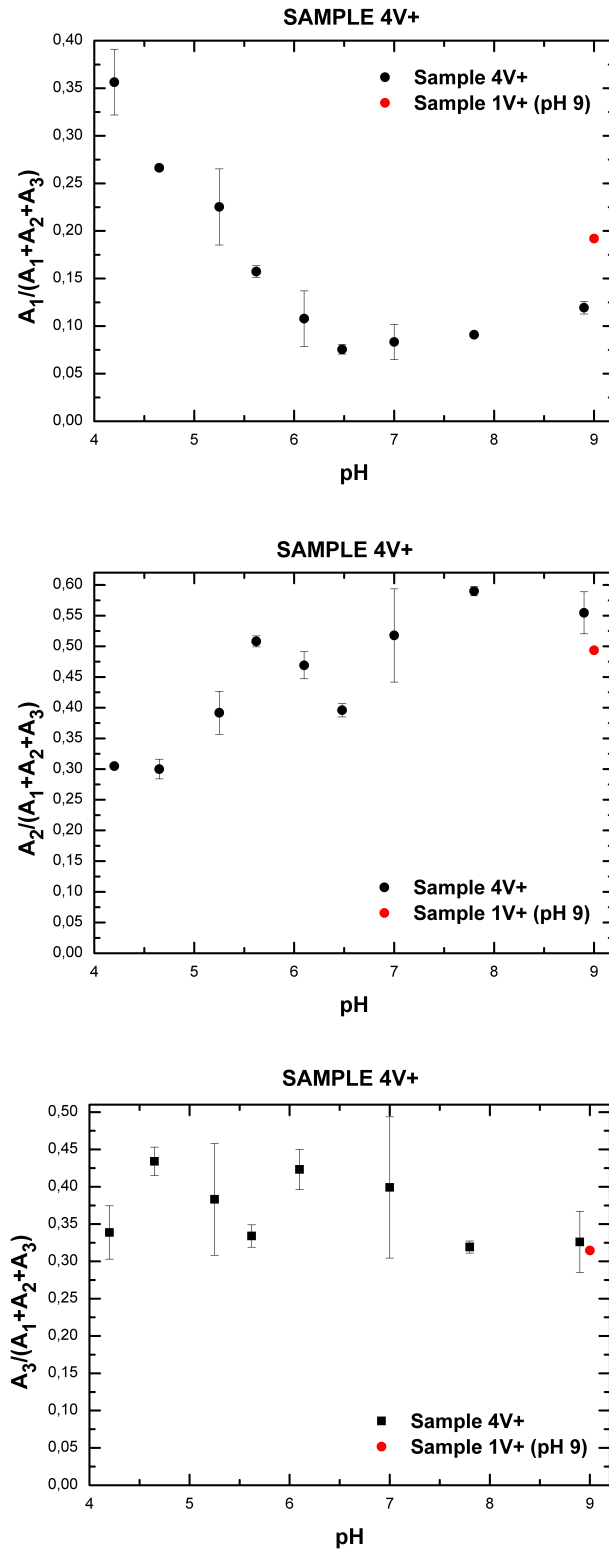


Figure 4.3: Ratio $\frac{A_i}{A_1 + A_2 + A_3}$ as a function of pH for the sample 4V+. The error bars reported derive from the standard deviations of the amplitudes obtained for two different measurement spots of the same sample, and for three slightly different ranges of time for the fit. Red points in the three graphics are the results obtained for the amplitudes at pH 9 for sample 1V+ fitted with a triexponential function.

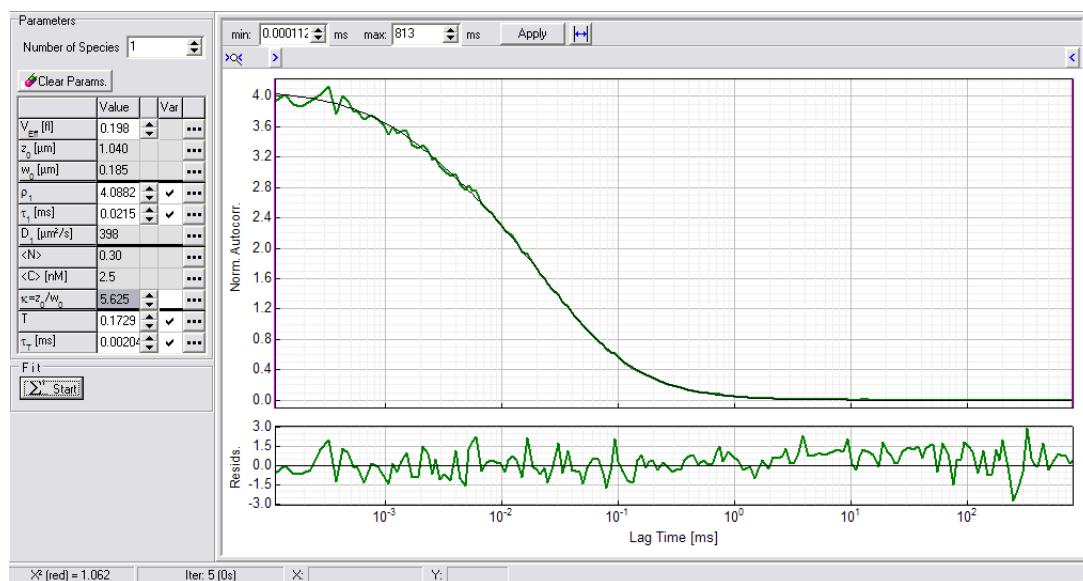


Figure 4.4: Top panel: the green line is the FCS curve of sample 1V+ 20nM, the grey line is the Triplet State Model fit. Left panel: values of fit parameters returned by the software. Bottom panel: respective normalized residues; the χ^2 is 1.062.

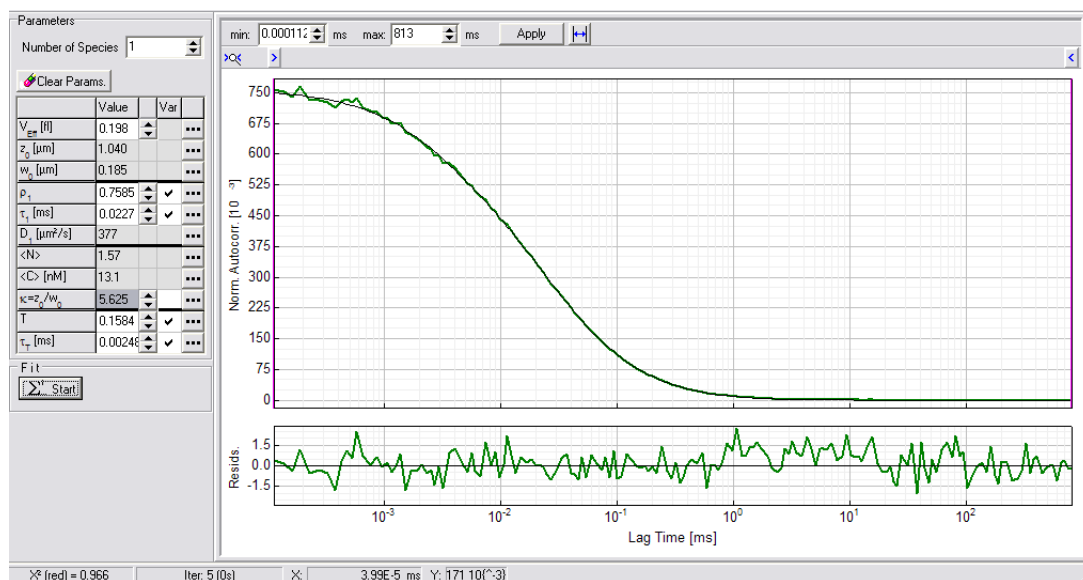


Figure 4.5: Top panel: the green line is the FCS curve of sample 10V+ 20nM, the grey line is the Triplet State Model fit. Left panel: values of fit parameters returned by the software. Bottom panel: respective normalized residues; the χ^2 is 0.966.

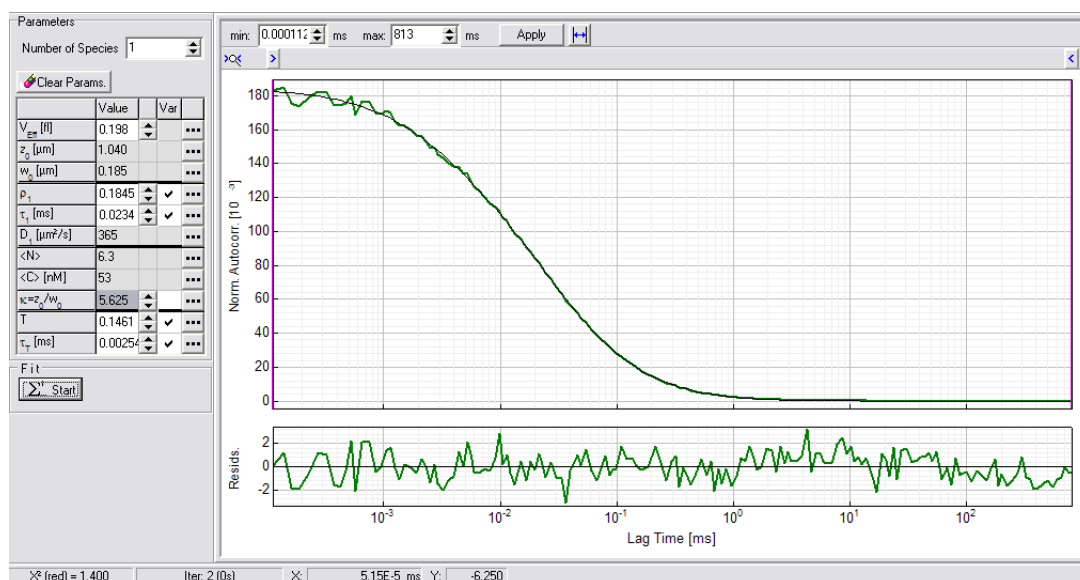


Figure 4.6: Top panel: the green line is the FCS curve of sample NHScarboxyfluorescein-Glycine 20nM, the grey line is the Triplet State Model fit. Left panel: values of fit parameters returned by the software. Bottom panel: respective normalized residues; the χ^2 is 1.4.

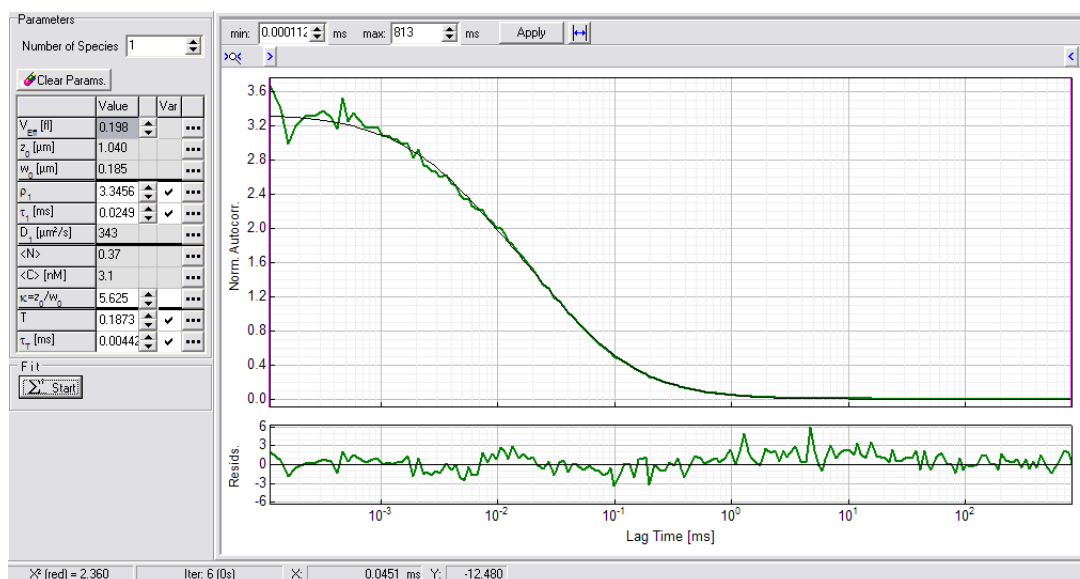


Figure 4.7: Top panel: the green line is the FCS curve of sample 10V+ 4nM, the grey line is the Triplet State Model fit. Left panel: values of fit parameters returned by the software. Bottom panel: respective normalized residues.

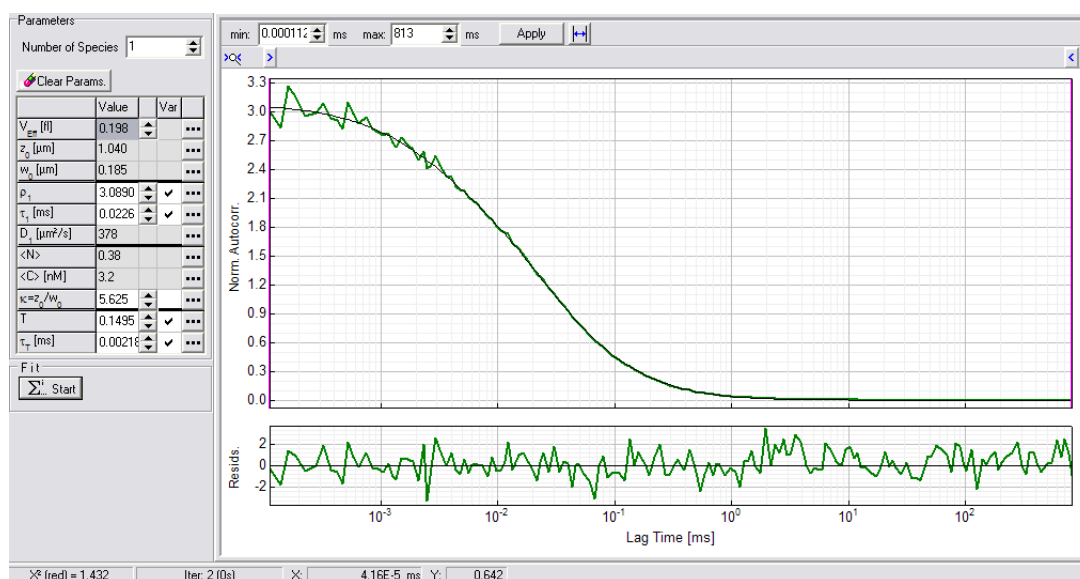


Figure 4.8: Top panel: the green line is the FCS curve of sample NHScarboxyfluorescein-Glycine 0.8nM, the grey line is the Triplet State Model fit. Left panel: values of fit parameters returned by the software. Bottom panel: respective normalized residues; the χ^2 is 1.43.

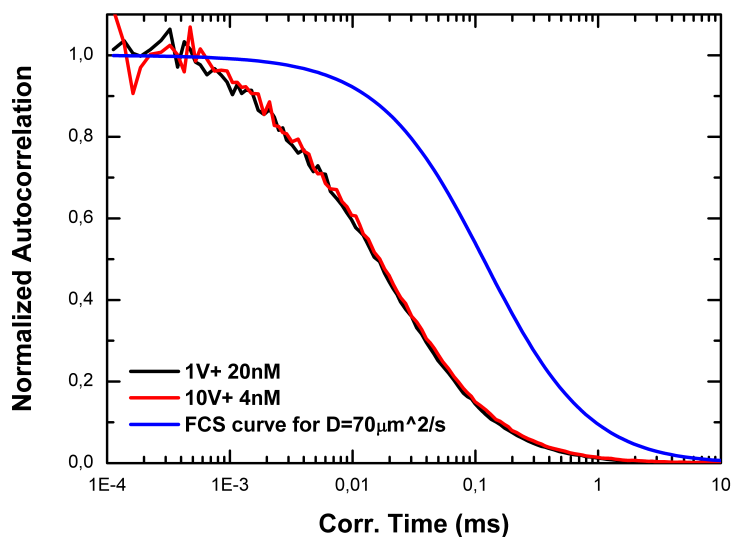


Figure 4.9: Comparison of normalized FCS curves obtained for sample 1V+ 20nM (black curve) and sample 10V+ 4nM (red curve) with a theoretical FCS curve for a diffusion coefficient of $70\mu\text{m}^2$.

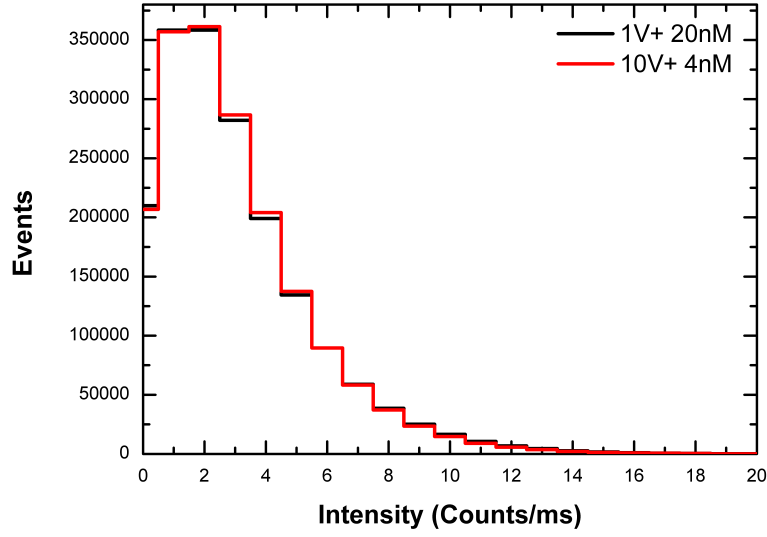


Figure 4.10: Histograms of the intensities (counts/ms) obtained with FCS technique for samples 1V+ 20nM and 10V+ 4nM.

$$G(\tau) = \left[1 + A_C e^{\left(-\frac{\tau}{\tau_c}\right)^{\beta_c}} \right] \frac{1}{\langle N \rangle} \left(1 + \frac{\tau}{\tau_D} \right)^{-1} \left(1 + \frac{\tau}{\tau_D \kappa^2} \right)^{-1/2}$$

$$\kappa = \frac{z_0}{w_0} ; V_{Eff} = \pi^{3/2} w_0^2 z_0^2 ; \langle C \rangle = \frac{\langle N \rangle}{V_{Eff}} ; D = \frac{w_0^2}{4 \tau_D}$$

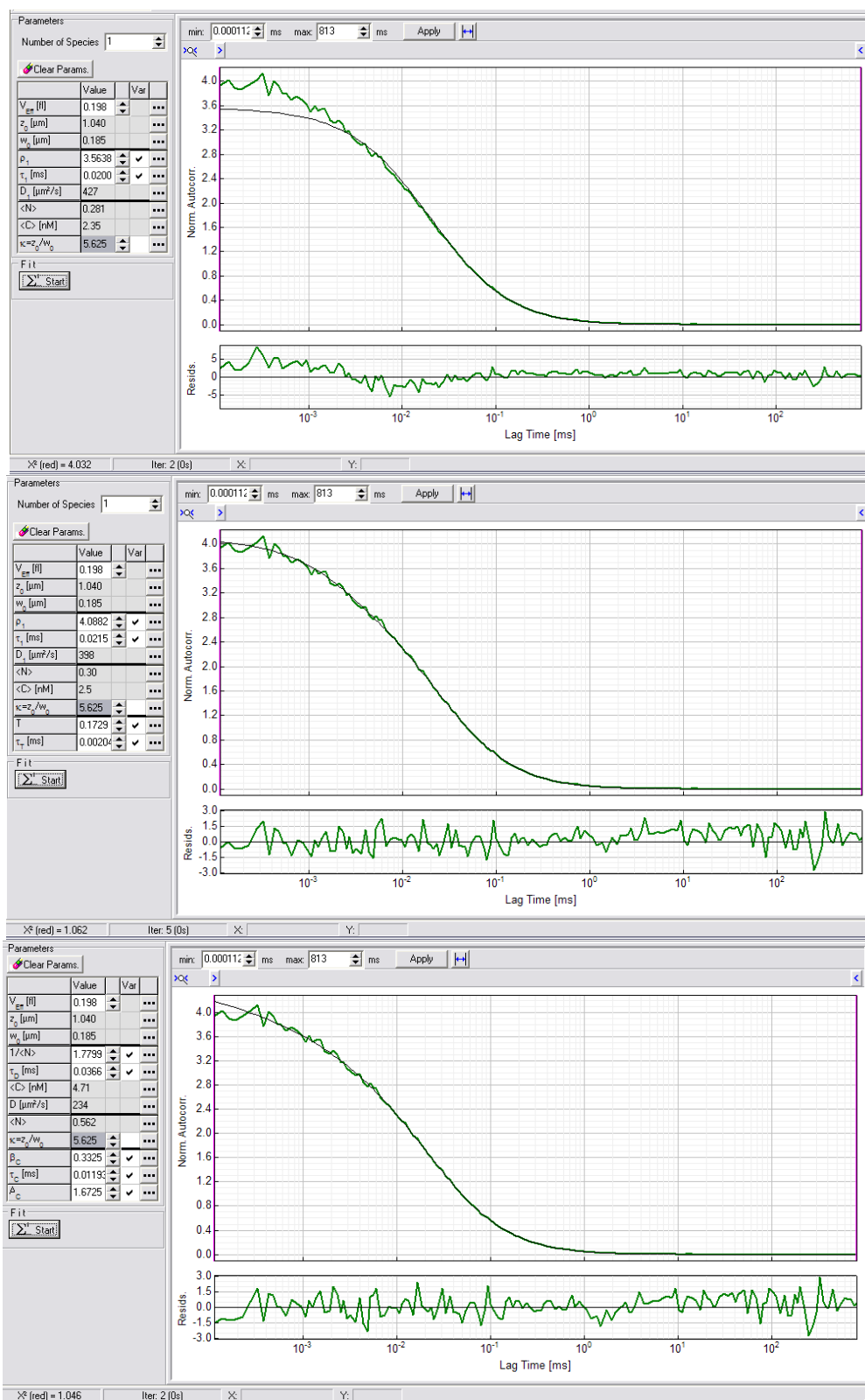


Figure 4.11: Pure Diffusion Model (top panel), Triplet State Model (mid panel) and Conformational Model (bottom panel) fits of autocorrelation curves for sample 1V+. From the comparison of the three panels, we can see that while the Pure Diffusion Model is evidently not suitable to describe the sample's system, both the Triplet State Model and the Conformational Model fit well the curve, with χ^2 of 1.062 and 1.046 respectively.

Conclusions and Perspectives

Dendrimers are perfectly branched monodisperse molecules, with well-defined structure and molecular weight. One of their most noticeable feature is the presence of functionalizable end groups which allow the linking of a variety of moieties to the dendrimer's surface, to serve for many different purposes. In this thesis work, I studied the physical-chemical properties of (PAMAM) dendrimers functionalized with Carboxyfluorescein N-hydroxy succinimide ester and evaluated the effects of the former on the photophysics of the linked fluorophores, with respect to the non-conjugated dye. In order to reach this goal, we investigated our samples by means of spectroscopy and fluorescence microscopy techniques commonly used in Biophysics, such as Fluorescence Lifetime Imaging Microscopy (FLIM), Single Molecule Detection (SMD) and Fluorescence Correlation Spectroscopy (FCS).

The experimental evidences found led us to the following conclusions:

1. The direct linkage to the dendrimer surface affects the optical properties of the dye by a similar extent for charged and "neutral" samples. Absorption and emission spectra at various pH were recorded; differences in the shape and peak wavelength of the spectra with respect to those of the non-conjugated fluorophore were interpreted as caused by interactions between the dye(s) and the dendrimer local environment. In particular, we observed a strong decrease in average quantum yield.
2. The aforementioned properties do not derive from homogeneous changes for all of the fluorescein dyes linked to the dendrimers, but from the presence in solution of many dendrimer-dye(s) populations displaying a distribution of different quantum yields and fluorescence decay rates. One of the results that suggested this conclusion arises from measurements of fluorescence decays by means of a Fluorescence Lifetime Imaging (FLIM) setup. They unveiled that our samples presented (at least) three lifetimes: one similar to that of the non-conjugated dye, one shorter, about one third of the first, and a subnanosecond one most probably belonging to a population of molecules almost non fluorescent.
3. These dendrimer-dye(s) populations displayed a dynamic behaviour, as deduced from single-molecule techniques, which represent the ultimate level of sensitivity. Indeed, single-molecule experiments carried out by means of a Total Internal Reflection (TIRF) setup and using an integration time of 1ms, did not allow us to discriminate between different populations, thus we turned to a technique which can investigate dynamical processes down to the μ s: Fluorescence Correlation Spectroscopy.

From the results obtained in these experiments, we could infer that the populations undergo conformational changes and rearrangements with a faster rate than pure diffusion (which can actually result in an overestimated value for the coefficient diffusion of the sample molecules).

The future perspectives of this work spread in two directions:

- In order to minimize the impact of dendrimers on bound fluorophores, a novel approach to dye-linking is presently being investigated at NEST Laboratories: it involves the production of an improved sample with a spacer inserted between the dendrimer surface and the fluorophore which aims to stabilize its optical properties by reducing the interactions with the dendrimer's environment. As illustrated in Fig. 4.12, the spacer is constituted by poly(ethylene glycol) (PEG) chains, which are covalently bound to the dendrimer's surface (*PEGylation*) and then functionalized with the desired moieties. Furthermore, PEGylated dendrimers have been found

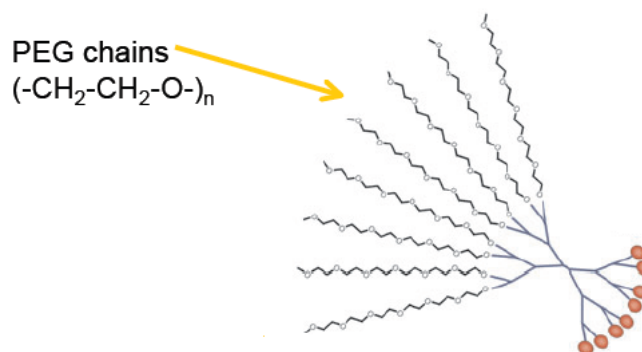


Figure 4.12: Schematical representation of poly(ethylene glycol) (PEG) chains bound to the dendrimer's surface.

to be more biocompatible and less toxic than normal ones when employed for studies *in vivo* [31]. They have also shown increased solubility, a feature that may reveal interesting in order to use PEGylated dendrimers as drug carriers for hydrophobic drugs that may not be in clinical use due to their limited water solubility.

- To better understand the dynamics of the dendrimer-dye(s) system, a future experiment which could be carried out is an FCS measurement using a wider Point Spread Function: this should help to minimize the impact of diffusive dynamics which complicates the interpretation of the autocorrelation curves of the samples. Also, a narrower binning for the Multi Channel Scaler curves might be adopted. Finally, the Triplet State Model used in this thesis work to fit the FCS data could be replaced by a model more suitable than the Conformational described in Subsection 4.3: the ideal fitting model should be able to account for the presence of more than just two species and to monitor and interpret the conformational changes (in times $< \mu\text{s}$) according to a fast and continuous dynamics.

Bibliography

- [1] C.C. Lee , J.A. MacKay, J.M. Frechet, F.C. Szoka *Designing Dendrimers for Biological Applications*. Nat. Biotechnol. **2005**, 23 (12) 1517-26.
- [2] J.M. Oliveira, A.J. Salgado, J.F. Manoa and R.L. Reisa *Dendrimers and Derivatives as a Potential Therapeutic Tool in Regenerative Medicine Strategies - A Review*. Progress in Polymer Science, 35, **2010**, 1163-1194.
- [3] L. Albertazzi, M. Serresi, A. Albanese and F. Beltram *Dendrimer Internalization and Intracellular Trafficking in Living Cells*. Mol. Pharmaceutics, **2010**, 7 (3), pp 680-688.
- [4] A. Saovapackhiran, A. D'Emanuele, D. Attwood and J. Penny *Surface Modification of PAMAM Dendrimers Modulates the Mechanism of Cellular Internalization*. Bioconjugate Chem., **2009**, 20, 693-701.
- [5] J. R. Lakowicz *Principles of Fluorescence Spectroscopy*, Third Edition, Chapters 22, 23, 24. Springer, **2006**.
- [6] J. M. Fréchet, D. A. Tomalia *Dendrimers and Other Dendritic Polymers*. Wiley, **2001**.
- [7] E. Buhleier, W. Wehner and F. Vögtle *Synthesis*. 155, **1978**.
- [8] D. A. Tomalia, J. R. dewald, M. J. Hall et al. *Preprints of the 1st SPSJ International Polymer Conference*. Soc. of Polym. Sci., Japan, Kyoto, p. 65, **1984**.
- [9] G. R. Newkome, Z. Yao, G. R. Baker, V. K. Gupta *Micelles. Part 1. Cascade molecules: a new approach to micelles. A [27]-arborol*. J. Org. Chem. 50: 2003, **1985**.
- [10] P. Antoni, Y. Hed, A. Nordberg, D. Nyström, H. von Holst, A. Hult and M. Malkoch *Bifunctional Dendrimers: From Robust Synthesis and Accelerated One-Pot Postfunctionalization Strategy to Potential Applications*. Angew. Int. Ed., 48 (12), pp 2126-2130, **2009**.
- [11] B. K. Nanjwade et al. *Dendrimers: Emerging Polymers for Drug-Delivery Systems*. European Journal of Pharmaceutical Sciences (Elsevier) 38 (3): 185196, **2009**.
- [12] R. Duncan, L. Izzo *Dendrimer Biocompatibility and Toxicity*. Advanced Drug Delivery Reviews 57 (**2005**) 2215-2237.

- [13] R. K. Tekade, T. Dutta, V. Gajbhiye and N. K. Jain *Exploring dendrimer towards dual drug delivery*. Journal of Microencapsulation 26 (4): 287-296, **2009**.
- [14] M. Liu, K Kono, J. Frechet *Water-soluble Unimolecular Micelles: their Potential as Drug Delivery Agents*. J. Cont. Rel. 65, 121-131, **2000**.
- [15] U. Gupta, H. B. Agashe, A. Asthana, N. K. Jain *Dendrimers: Novel Polymeric Nanoarchitectures for Solubility Enhancement Biomacromolecules*. Synthesis 7: 155-158, **2006**.
- [16] T.P. Thomas, I. J. Majoros, A. Kotlyar et al. *Targeting and Inhibition of Cell Growth by an Engineered Dendritic Nanodevice*. J. Med. Chem. 48: 37293735, **2005**.
- [17] C. Bieniarz *Dendrimers: Applications to Pharmaceutical and Medicinal Chemistry*. Encyclopedia of Pharmaceutical Technology, vol.18, Marcel Dekker Inc., New York, **1999**, pp. 55-89.
- [18] R. Jevprasesphant, J. Penny, R. Jalal, D. Attwood D, N. B. McKeown, A. D'Emanuele *The influence of surface modification on the cytotoxicity of PAMAM dendrimers*. Int J Pharm **2003**; 252:263-6.
- [19] G. Granucci, *Lectures from the Course of Photochemistry*, University of Pisa, **2010**.
- [20] Cantor and Schimmel, *Biophysical Chemistry Part II: Techniques for the study of biological structure and function*. W.H. Freeman and Company, Eleventh printing, 1998.
- [21] *Fluorescence Correlation Spectroscopy: The Femtoliter Test Tube - System Calibration and In Vitro Applications*. Confocal Application Letters, 36, March **2010**.
- [22] Carolyn L. Waite, Sarah M. Sparks, Kathryn E. Uhrich and Charles M. Roth *Acetylation of PAMAM dendrimers for cellular delivery of siRNA*. BMC Biotechnology, **2009**.
- [23] *Molecular Probes Handbook - A Guide to Fluorescent Probes and Labeling Technologies*, 11th Edition. Invitrogen.
- [24] D. Magde, G.E. Rojas, and P. Seybold *Solvent Dependence of the Fluorescence Lifetimes of Xanthene Dyes*. Photochem. Photobiol. 70, 737, **1999**.
- [25] S. Massou, R. Albilot, M. Prats *Carboxyfluorescein Fluorescence Experiments*. Biochemical Education 28, 171-173, **2000**
- [26] J. C. McDonald et al. *Fabrication of Microfluidic Systems in Poly(dimethylsiloxane)*. Electrophoresis, 21, 27-40, **2000**.
- [27] K. S. McCain, P. Schluesche and J. M. Harris *Modifying the Adsorption Behavior of Polyamidoamine Dendrimers at Silica Surfaces Investigated by Total Internal Reflection Fluorescence Correlation Spectroscopy*. Anal. Chem., 76 (4), pp 930-938, **2004**.

- [28] P. K. Maiti, B. Bagchi *Diffusion of Flexible, Charged, Nanoscopic Molecules in Solution: Size and pH Dependence for PAMAM Dendrimer*. The Journal of Chemical Physics 131, 214901, **2009**.
- [29] B. Fritzing, U. Scheler *Scaling Behaviour of PAMAM Dendrimers Determined by Diffusion NMR*. Macromolecular Chemistry and Physics, **2005**.
- [30] C. M. Hutnik, A. G. Szabo *Confirmation that multiexponential fluorescence decay behavior of holoazurin originates from conformational heterogeneity*. Biochemistry, May 2;28(9):3923-34, **1989**.
- [31] J. Lim and E. E. Simanek *Toward the Next-Generation Drug Delivery Vehicle: Synthesis of a Dendrimer with Four Orthogonally Reactive Groups*. Molecular Pharmaceutics, **2005**.

Acknowledgements

Vorrei ringraziare il mio relatore, il Dott. Stefano Luin, per la sua grande disponibilità durante tutte le fasi di realizzazione di questo lavoro, per la sua pazienza nello spiegarmi gli argomenti più ostici e, non da ultimo, per avermi trasmesso in questo anno la sua passione per una materia tanto nuova quanto affascinante come la Biofisica. Grazie per avermi dato fiducia ed avermi sempre incoraggiata a continuare per questa strada che ho scoperto esistere solo due anni fa e che ho deciso di intraprendere per la mia carriera futura.

Desidero inoltre ringraziare tutti i ricercatori e i dottorandi che mi hanno seguita con attenzione e professionalità nel lungo periodo trascorso (al buio o alla luce!) nel Laboratorio NEST, in particolare Lorenzo Albertazzi per le sue esaurienti e dettagliate spiegazioni sul mondo dei dendrimeri, questi sconosciuti, e per avermi seguita passo passo nella parte prettamente chimica del lavoro che ho svolto; a Giovanni Signore per le utilissime chiacchierate e per la pazienza dimostrata quando ho rotto un pHmetro da 200 euro; a tutti coloro cui almeno una volta ho chiesto consigli e chiarimenti sul funzionamento degli strumenti e sul metodo di acquisizione dati, grazie.

Un ringraziamento particolare va alla mia famiglia tutta, in primis ai miei genitori Carla e Antonio, che mi hanno SEMPRE, anche nei momenti più difficili (e non sono stati pochi), sostenuta e spinta ad andare avanti negli studi che ho scelto per passione, senza smettere mai di credere in me e nelle mie capacità. A mio fratello Edoardo, un ragazzo unico nella sua generazione, per le avvincenti discussioni su argomenti di attualità non proprio inerenti alla Fisica, ma egualmente, se non più interessanti, per avermi invitata a seguire una lezione di Diritto Internazionale che mi è piaciuta davvero un sacco e per aver condiviso con me questi due ultimi anni a Pisa: non smettere mai di coltivare le tue passioni, sono sicura che ti porteranno lontano. Inoltre, grazie a mio nonno Antonio per aver continuato ad essere per me un modello di vita anche in questi anni a Pisa, ai miei zii e cugini, in particolare a mia zia Angela, unico altro Fisico della famiglia e pioniera della Fisica delle particelle in un periodo in cui la Scienza era ancora appannaggio degli uomini.

Le preparazioni degli esami, i giorni passati in laboratorio e le mie giornate da universitaria a Pisa non sarebbero state altrettanto fruttuose e divertenti senza tutti i miei amici, fisici e non fisici, belli e brutti, alti e bassi, brilli o sobri ma comunque speciali. Grazie a Silvio, a Leo e a Mariangela per avermi sopportata e sostenuta quando ero nervosa e/o depressa nelle uggiose giornate invernali in laboratorio, nei momenti in cui non credevo di farcela e quando era la quinta volta che ripetevo lo stesso esperimento senza ottenere i

risultati sperati.

Grazie a Pietro, per essermi rimasto vicino ed avermi consigliata ed aiutata anche a distanza, psicologicamente e materialmente; per te ci sarà sempre un posto speciale nel mio cuore e nei miei ricordi.

Infine, rivolgo il mio pensiero a voi, Mary, Alvisè, Piero, Giorgia, Martino e Domenico: tre mesi fa siete entrati nella mia vita come una ventata d'aria fresca e non sapete quanto conoscervi sia stato importante per me. In voi ho trovato un gruppo di amici che non avevo da moltissimo tempo, siete persone davvero uniche, nei vostri pregi e difetti, e non sapete quanto avrei voluto che il futuro ci avesse riservato infiniti altri giorni come quelli passati negli ultimi mesi. Quando, fra quattro o cinque anni, sarò in un qualche appartamento inglese cercando di mettere ordine nella mia vita, mi capiterà fra le mani questa tesi e rileggerò queste parole: so già che l'unica cosa che farò in quel momento sarà sperare che non mi abbiate dimenticata. Vi saluto con le parole di un gruppo le cui note ci hanno spesso accompagnato nelle serate insieme: chissà che" forse, un giorno, potremo incontrarci di nuovo lungo la strada".